The Pennsylvania State University

The Graduate School

College of Engineering

THERMALLY EVAPORATED CONFORMAL THIN FILMS ON NON-TRADITIONAL/NON-PLANAR SUBSTRATES

A Dissertation in

Engineering Science and Mechanics

by

Drew Patrick Pulsifer

Submitted in Partial Fulfillment

of the Requirements

for the Degree of

Doctor of Philosophy

December 2013

The dissertation of Drew Patrick Pulsifer was reviewed and approved* by the following:

Akhlesh Lakhtakia

Charles Godfrey Binder Professor in Engineering Science and Mechanics

Dissertation Advisor and Chair of Committee

Jian Xu

Associate Professor of Engineering Science and Mechanics

Vladimir V. Semak

Associate Professor of Engineering Science and Mechanics and Senior Research Associate

Carlo G. Pantano

Distinguished Professor of Materials Science and Engineering

Director of the Materials Research Institute

Judith A. Todd

Professor of Engineering Science and Mechanics

P. B. Breneman Department Head Chair

*Signatures are on file in the Graduate School.

Abstract

Conformal thin films have a wide variety of uses in the microelectronics, optics, and coatings industries. The ever-increasing capabilities of these conformal thin films have enabled tremendous technological advancement in the last half century. During this period, new thin-film deposition techniques have been developed and refined. While these techniques have remarkable performance for traditional applications which utilize planar substrates such as silicon wafers, they are not suitable for the conformal coating of non-traditional substrates such as biological material.

The process of thermally evaporating a material under vacuum conditions is one of the oldest thin-film deposition techniques which is able to produce functional film morphologies. A drawback of thermally evaporated thin films is that they are not intrinsically conformal. To overcome this, while maintaining the advantages of thermal evaporation, a procedure for varying the substrates orientation with respect to the incident vapor flux during deposition was developed immediately prior to the research undertaken for this doctoral dissertation. This process was shown to greatly improve the conformality of thermally evaporated thin films. This development allows for several applications of thermally evaporated conformal thin films on non-planar/non-traditional substrates.

Three settings in which to evaluate the improved conformal deposition of thermally evaporated thin films were investigated for this dissertation. In these settings the thin-film morphologies are of different types. In the first setting, a bioreplication approach was used to fabricate artificial visual decoys for the invasive species *Agrilus planipennis*, commonly known as the emerald ash borer (EAB). The mating behavior of this species involves an overflying EAB male pouncing on an EAB female at rest on an ash leaflet before copulation. The male spots the female on the leaflet by visually detecting the iridescent green color of the female's elytra. As rearing EAB and then deploying dead females as decoys is both arduous and inconvenient, the development of an artificial decoy would be of great interest to entomologists and foresters. A dead female EAB was used to make a negative die of nickel and a positive die of epoxy. The process of fabricating the paired dies utilized thermally evaporated conformal thin films in several critical steps. In order to conformally coat the EAB with nickel, the substrate stage holding the female EAB was periodically rocked and rotated during the deposition. This process was designed to result in a uniform thin film of $\sim$ 500-nm thickness with dense morphology. The nickel film was then reinforced through an electroforming process and mounted in a fixture which allowed it to be

heated electrically. The corresponding positive die was replicated from the negative die through a series of successive castings. The final EAB positive die was fabricated from a hard epoxy material and attached to a fixture which allowed it to be heated while being pressed into the negative die. Decoys were then made by first depositing a quarter-wave-stack Bragg reflector on a polymer sheet and then stamping it with the pair of matched negative and positive dies to take the shape of the upper surface of an EAB female. As nearly 100 decoys were fabricated from just one EAB female, this bioreplication process is industrially scalable. Preliminary results from field trapping tests are indicative of success.

For the second setting, a method of developing latent fingermarks with thermally evaporated conformal thin films was developed. Fingermarks have long been used to identify the individual who left them behind when he/she touched an object with the friction ridges of his/her hands. In many cases the fingermark which is left behind consists of sebaceous secretions which are not clearly visible under normal conditions. In order to make the fingermarks visible and identifiable, they are traditionally developed by either a physical technique which relies on a material preferentially sticking to sebaceous materials or a chemical technique which relies on a reaction with material within the fingermark. In this application, a columnar thin film (CTF) is deposited conformally over both the fingermark and the underlying substrate. The CTF is produced by the conformal-evaporated-film-by-rotation method, wherein the substrate with the fingermark upon it is held obliquely with respect to a vapor flux in a vacuum chamber. The substrate is then rapidly rotated about its surface normal resulting in a conformal film with columnar morphology. This technique was optimized for several substrates and compared with traditional development techniques. CTF development was found to be superior to traditional techniques in several cases. Use of the CTF was investigated for several types of particularly difficult to develop fingermarks such as those which consist of both bloody and nonbloody areas, and fingermarks on fired cartridge casings. The CTF technique's sensitivity was also compared to that of traditional development techniques. Finally, the CTF technique was compared with another thin film deposition technique called vacuum-metal deposition.

The final setting in which thermally evaporated conformal thin films were evaluated in this dissertation is to enable the experimental observation of the Dyakonov–Tamm wave. The Dyakonov–Tamm wave was predicted to be guided by the interface of two materials, at least one of which is both periodically non-homogeneous in the direction perpendicular to the interface plane and anisotropic. A dense magnesium-fluoride thin film and a zinc-selenide chiral sculptured thin film were selected to provide such an interface. The structural properties of the chiral sculptured thin film were designed to give the zinc-selenide layer, in conjunction with the magnesium-fluoride layer, the optical properties required to support the propagation of a Dyakonov–Tamm wave. The Dyakonov–Tamm wave was first demonstrated in the prism-coupled configuration and then in the grating-coupled configuration. For the case of the grating-coupled configuration, the zinc-selenide-chiral sculptured thin film was deposited on a non-planar substrate consisting of a periodic grating fabricated from magnesium fluoride.

In concert these three applications of thermally evaporated conformal thin films on non-planar/non-traditional substrates demonstrate that the poor intrinsic conformality of thermal evaporation can be overcome. Additionally, the poor intrinsic conformality can be overcome while still maintaining the advantages of being able to deposit an array of materials and produce morphologies which are essential to the function of a device of process. The use of thermal evaporation allows thin films with dense morphology to be deposited in the first setting, vertical columnar morphology in the second setting, and a helical morphology in the third setting.

Table of Contents

List of Figures

List of Tables

Acknowledgments

I would like to express my sincere gratitude to my dissertation advisor, Dr. Akhlesh Lakhtakia, whose guidance was instrumental to the work leading to this dissertation. He routinely went above and beyond what could be expected of an advisor, and always put my best interests as the top priority. He was a great advisor and an even greater mentor.

I am thankful to the members of my dissertation committee, Dr. Vladimir Semak, Dr. Jian Xu, and Dr. Carlo Pantano, for the time and effort they put into evaluating this dissertation. I also thank Dr. Pantano for the use of his laboratory facilities.

I acknowledge my collaborators who contributed to projects described in this dissertation:

(i) Dr. Michael Domingue and Dr. Thomas Baker of the Department of Entomology for their work in evaluating the performance of bioreplicated emerald ash borer decoys;

(ii) Mahesh Narkhede and Dr. Jayant Kumar of the University of Massachusetts Lowell for producing the Bragg reflectors used in the fabrication of emerald ash borer decoys;

(iii) Beverly Post of the Department of Engineering Science and Mechanics for aiding in the preparation of emerald ash borer decoys;

(iv) Sarah Muhlberger, Stephanie Williams, and Dr. Robert Shaler of the Forensic Science Program for their preparation and evaluation of fingermarks developed by the columnar-thin-film fingermark development technique;

(v) Dr. Muhammad Faryad of the Department of Engineering Science and Mechanics for working with me on the theoretical work that preceded the observation of the Dyakonov–Tamm wave, and Anthony Hall of the Department of Chemistry for working with me to produce the dielectric gratings used in portions of my work on Dyakonov–Tamm waves;

(vi) Funding provided through Award No. 2010-DN-BX-K232 from the National Institute of Justice, Office of Justice Programs, U.S. Department of Justice for financial support of my work on the columnar-thin-film fingermark development technique ;

(vii) Funding provided through USDA-APHIS-CPHST cooperative agreement No. 11-8130-0081-CA for financial support of my work on bioreplicated emerald ash borer decoys; and

(viii) Funding provided through the Charles Goodfrey Binder Endowment at Penn State for financial support of my work on Dyakonov–Tamm waves.

Dedication

This dissertation is dedicated to my friends and family for patiently listening to all of my stories about bugs, fingermarks, and surface waves.

Chapter 1

Introduction

Thin films are deposited on a bulk material as small molecular clusters in order to impart some properties that are not easily obtained by the substrate alone. Typically, thin films range in thickness between a fraction of a nanometer and tens of micrometers [1,2]. The intended property that is to be imparted to the substrate depends on the specific application. Thin films find application in many areas. Such applications include: reflective and antireflective coatings, filters, decoration, and waveguides for optical applications [3–5]; insulator, conductor, and semiconductor films for electrical applications [6]; diffusion and corrosion barriers for chemical applications [7]; and hardness, adhesion, and wear-resistance films for mechanical applications [8].

The performance of a thin film is often dependent upon the uniformity of the film in thickness, composition, and morphology [1]. As such, thin films are typically deposited on planar substrates because uniformity is more easily achieved. When a non-planar substrate is utilized, measures have to be taken to ensure that a uniformly thick film is produced. In each of the listed areas in which thin films are widely utilized, non-planar substrates are being increasingly used, as the advantages of more complicated device architectures are identified and the technological barriers of producing them are overcome. In this dissertation, I discuss the deposition of conformal thin films on non-planar/non-traditional substrates by means of thermal evaporation. The advantage

of these thermally evaporated conformal thin films is demonstrated in three settings, all of which utilize non-traditional/non-planar substrates. In each of the three settings, the morphology of the conformal thin film is distinctive.

1.1 Conformal Thin-Film Background

Ideally, a conformal thin film is one which is of uniform thickness, composition, and morphology at all locations when deposited on an undulating or uneven substrate [9]. In practice, few films are perfectly conformal and there is some level of variation in thickness, composition, and/or morphology occurring at the location of physical or chemical changes in the underlying substrate. In practice, these variations often take the form of step edges, trenches, or transitioning substrate materials [10].

Conformal thin films find many applications in modern microelectronics fabrication where step edges, high-aspect-ratio trenches, and complicated overhangs have become common features [10]. As the coming generations of microelectronic devices increasingly will utilize 3-dimensional architectures [11], the demand for and the quality of conformal thin films will undoubtedly increase as well. Along with traditional applications of conformal thin films, new applications will also arise. These could come from the integration of high-tech devices into everyday items [12]. The mobile phone industry may lead in this development as the integration of micro-electro-mechanical-systems increases in prevalence, making our smart phones even smarter [13]. As advances in the understanding of the micro-and-nano scale world arise through fields not normally associated with nanotechnology, thin-film technologies will be adapted and utilized for as yet unseen ways. Nature will provide inspiration for many of these developments [14]. One example of this process is the use of nano-patterned surfaces to reduce reflection which were inspired by the surface of the eyes of a moth [15]. Thin films will undoubtedly play a role in these developments, as they have been a building block of a large portion of nanotechnologies.

Commonly used methods to produce films with good conformality typically exhibit an intrinsic mechanism which causes material to be deposited evenly over the substrate. These mechanisms include surface diffusion [16], operation at near-atmospheric pressures [1, Sec. 6.5.4], and self-limiting chemical reactions [17]. Let me briefly look at several film deposition processes which intrinsically produce conformal thin films due to the combination of the short mean free path of the vapor and high surface diffusion.

1.1.1 Chemical Vapor Deposition

Chemical vapor deposition (CVD) is a deposition process which utilizes volatile vapor-phase precursor chemicals which can be caused to react at the substrate surface in such a way as to result in the desired film material condensing on the substrate [18]. The CVD process is carried out in a reactor which allows for fine control over parameters which govern the deposition process [19]. These parameters often include: pressure, substrate temperature, and gas flow rates.

A common example of this deposition process is the pyrolysis of silane gas [20]. Silane gas is allowed to flow over a substrate which is heated to such a temperature that the silane gas decomposes on contact with the substrate, producing (i) silicon which condenses on the substrate and (ii) gaseous hydrogen which flows out of the reactor [1, Ch. 7].

Several mechanisms lead to the conformality of thin films deposited by CVD. The first is the gas kinetics of operation at relatively high pressures [1, Sec. 6.5.4]. At these pressures, the mean free path of the vapor molecules is so small that it allows for the vapor to approach the substrate from many directions. Additionally, the elevated temperature of the substrates results in a high degree of surface diffusion of the condensed material which leads to a leveling of the film [16]. Finally, the probability of the vapor reacting at the substrate surface during any collision is significantly less than unity [21]. This allows the vapor to penetrate trenches in the substrate because it can go through multiple collisions with the substrate before reacting [1, Sec. 7.3.3].

CVD comes in many flavors [2] with many of the differences being in the method of delivering the vapor or method of providing the necessary energy to produce the desired reaction.

CVD is one of the most widely used techniques to produce conformal thin films. Because it operates in a high-pressure fluid-flow regime, it is able to batch process substrates with no requirement for direct line of sight to all portions of the substrate [10]. Although CVD produces high-quality conformal films, it is not without drawbacks. For the type of work on non-traditional/non-planar substrates utilized in this dissertation, the greatest drawback of CVD is potential damage to sensitive substrates such as those of biological origin. This damage comes from the high temperatures or plasmas present in a CVD reactor [22]. An additional drawback of CVD is that it requires specific high-purity precursor gases, many of which can be dangerous [1, Sec. 7.1.1].

1.1.2 Atomic Layer Deposition

One variation of CVD which is worth discussing in some detail is atomic layer deposition (ALD) [23]. The feature of ALD that makes it stand out from CVD is that the deposition of the film occurs in discrete pulses rather than continuously. This is done by using a pair of complementary chemical precursors which are sequentially and periodically introduced into the reactor. This results in highly conformal films due to the fact that the first precursor will adsorb onto all available sites on the substrate [17, 23]. The excess quantity of the first precursor is then purged from the reactor before introducing the second precursor. As the second precursor comes into contact with the first, both react with each other to precipitate the desired film material. The cycle is repeated until the desired film thickness is achieved [24].

ALD is a very appealing technique with which to deposit conformal thin films. Due to the self-limiting reaction processes, it is possible to exert very fine control over film thickness [17]. For this reason, ALD has become a preferred industrial method for depositing gate-oxide layers in transistors [23]. Some materials can also be deposited at relatively low temperatures, thereby

allowing for the use of non-traditional substrates such as butterfly wings [25].

There are also several drawbacks to ALD. Due to the layer-by-layer growth exhibited by ALD, the deposition rate is slow when compared to other techniques [24]. As with CVD, the precursor chemicals used to deposit some materials can damage chemically sensitive substrates or be otherwise dangerous [23]. Along with chemical damage, biological substrates may also be damaged by the high temperatures needed to deposit certain films. Additionally, only some types of films can be deposited at low cost by ALD [26].

1.1.3 Sputtering

A third film-deposition technique which inherently produces conformality is sputtering. Sputter deposition is a physical process by which high-energy inert atoms, such as argon atoms in a plasma, bombard a target composed of the source material [1, Sec. 9.3.3]. Through a momentum-transfer process [1, Sec. 9.1], the source material is ejected from the target. Depending on the gas pressure in the sputtering chamber, the sputtered target material may undergo several collisions before eventually condensing on the substrate. These multiple collisions are one mechanism that leads to the conformal nature of sputter-deposited films [1, Sec. 8.5.4]. Because of the multiple collisions which occur prior to condensation, the vapor effectively arrives from many directions. The presence of the plasma can also contribute to the conformality of sputter-deposited thin films. Some fractions of the sputtered source material and the plasma itself may arrive at the substrate with such energy that they forward sputter or resputter material already condensed on the substrate. This process leads to some amount of surface diffusion, in turn improving the conformality of the deposited film. Surface diffusion can also be increased through ion bombardment or heating of the substrate [16].

As with the other techniques described, sputtering has both advantages and drawbacks when depositing conformal thin films. The greatest advantage to sputtering is that nearly any material can be deposited [1, Sec. 9.3.3]. By producing a target of the proper composition, films with com-

plicated compositions can be deposited. A drawback of sputtering is that it utilizes a plasma and elevated substrate temperatures that may damage biological substrates. An additional drawback of sputtering is that the gas used in sputtering is often incorporated into the deposited films, resulting in higher contamination when compared to other techniques [27].

1.2 Directional Thin-Film Deposition Techniques

A common drawback among the conformal techniques described in Sec. 1.1 is the high probability for sensitive biological substrates to be damaged during the deposition process. This damage often arises from elevated substrate temperatures, exposure to damaging chemicals, or exposure to a plasma. Because these characteristics are intrinsic to the previously described conformal-thin-film deposition processes, they can not be eliminated. However, there are other deposition techniques that do not require the use of reactive chemicals, elevated substrate temperatures, or a plasma in proximity of the substrate.

The deposition techniques which meet these criteria are thermal evaporation [2], electron-beam evaporation [1, Sec. 8.2], ion-beam sputtering [1, Sec. 8.5.4], and pulsed-laser deposition [28]. Each of these deposition techniques are carried out under high-vacuum conditions and the generated vapor flux is highly directional [1, Sec. 4.6]. The directional nature of the vapor flux results in shadowing while a film is being deposited on a non-planar substrate [29]. Shadowing refers to the fact that portions of the non-planar substrate which do not have a line of sight to the vapor source receive little or no vapor flux, thereby resulting in insubstantial or no film growth in those areas.

If the goal is to produce conformal thin films, at first glance it would appear that the use of any technique which produces a directional vapor flux would be a poor choice. In order to improve the conformality and uniformity of thin films deposited by these techniques, substrates are often placed on heated planetary substrate stages [1, Sec. 4.6]. The idea behind planetary

stages is that by changing the location of the substrate in relation to the source of the vapor flux, the directions from which the vapor flux arrives at the substrate can be enhanced. This reduces the effect of shadowing and improves both conformality and uniformity when batch processing many substrates simultaneously [1, Sec. 4.6]. As with the previously discussed film-deposition techniques, heating the substrate improves uniformity by increasing the surface mobility of the source material arriving on the substrate. When used in combination, planetary substrate stages and substrate heating can greatly improve the conformality of films deposited from a directional vapor source [1, Sec. 4.6].

Thin-film deposition methods which generate directional vapor flux exhibit several advantages over methods described in Secs. 1.1.1–1.1.3. The greatest of these is the ease of implementation. Many low-temperature materials can be evaporated by thermal evaporation, a large number of materials can be deposited by electron-beam evaporation [1, Sec. 8.2], a greater number still by ion-beam sputtering [1, Sec. 8.5], and there are only few materials which can not be deposited by pulsed-laser deposition [30]. This ease of implementation allows for a single deposition tool to be used for a wide array of applications which is particularly useful in a laboratory setting. An additional advantage to these techniques is that the directional vapor flux can be utilized to produce several interesting film morphologies [31].

So far, I have eliminated reactive chemicals and plasma as sources of substrate damage when conformally coating fragile substrates, but even with the alternative techniques described heating of the substrate is still required to produce an acceptable conformal thin film. A method of improving the conformality of thermally evaporated thin films while eliminating the need for substrate heating is discussed in Sec. 1.3.

1.3 Improved Conformal Thin Films by Thermal Evaporation

1.3.1 Thermal Evaporation by Resistive Heating

Let me now narrow my focus to thin films that are deposited by thermal evaporation from a resistively heated source [2, Ch. 2]. In this technique, a source material is placed in a metal receptacle within a vacuum chamber. In this context, a vacuum chamber is one in which the mean free path is of the order of tens of meters [1, Sec. 2.7] whereas the linear dimensions of the chamber are on the order of tens of centimeters. The receptacle is most often made of tungsten, but other refractory metals are used as well [1, Sec. 4.5.1]. The receptacle is heated by passing a high current through it. When the source material is sufficiently heated, it undergoes phase transitions, with many materials first melting and then evaporating, while others sublimate [1, Sec. 4.1]. Once in the gas phase, clusters of atoms (or molecules) ballistically travel from the receptacle to either a portion of the evaporation chamber or the substrate. The distribution of vapor ejected from the source takes the form of $\cos^n \theta$, where θ is the angle as measured from the normal to the receptacle's aperture and n is the order of the distribution [1, Sec. 4.6]. The order of the distribution increases as the flux is more confined to the source normal. In practice, a receptacle in the form of a wire basket produces a $0th$ order ($n \geq 1$) cosine distribution while dimpled receptacles and crucibles produce higher-order cosine distributions.

If the substrate is maintained at near-ambient temperatures, the sticking coefficient of vapor impinging on the substrate is nearly unity and there is very little surface diffusion before the vapor is incorporated into the growing thin film [1, Sec. 5.2]. While this process does not lead to improved conformality, it is a gentle process which does not damage sensitive substrates. Additionally, the ballistic transport from the source receptacle to the substrate can result in shadowing that further reduces the conformality of the deposited thin film [1, Sec. 5.4]. These

challenges to producing conformal thin films by thermal evaporation are addressed in Sec. 1.3.2 and are in fact advantageous in some situations.

Thermal evaporation is an appealing technique with which to deposit conformal thin films on sensitive substrates, because it produces vapor with low-energy clusters (compared to those of ion-beam sputtering or pulsed-laser deposition) and without damage from reactive chemicals. When compared to electron-beam evaporation, resistive heating of the source material results in less waste thermal energy being generated at the substrate. This allows for substrates to be maintained at relatively low temperatures which is essential for depositing conformal thin films on fragile substrates such as fingermarks. A further advantage of thermal evaporation is that a large number of materials can be deposited with no alteration to the apparatus [32]. This is a great advantage in that it allows for a single apparatus to be broadly used. When compared to other thin-film deposition techniques, the apparatus for thermal evaporation is relatively inexpensive and easily maintained. This low cost has led to wide availability of thermal-evaporation systems. In practical terms, this means that thermal-evaporation equipment can be dedicated to depositing thin films on non-traditional substrates which would never be permitted in more expensive or less robust equipment due to concerns about contamination. Finally, thermal evaporation allows for the control over film deposition rates ranging from ~ 0.01 to more than 10 nm s^{-1}.

1.3.2 Conformal-Evaporated-Film-by-Rotation

The method for improving film conformality discussed here should be applicable for any deposition method which utilizes a directional vapor source. In Sec. 1.2 substrate motion and heating to improve the conformality of thin films were discussed. While substrate heating greatly improves conformality, it damages temperature-sensitive substrates. With that in mind, I eliminated substrate heating and was left with substrate motion to improve film conformality. The use of a planetary substrate stage can provide some motion which improves conformality. However, due to limited range of motion provided by the planetary stage, the shape of the vapor plume which

depends on the source used [1, Sec. 4.6], the diversity of substrate geometries, and the convolution of these three factors, the variation in the direction of vapor flux arriving at the substrates surface is restricted and can not be tailored to the specific geometry of a given substrate.

With the aforementioned limitations of planetary substrate stages in mind, I decided to use a substrate stage which utilizes two independently operable and programmable axes of rotation [33]. The conformal-evaporated-film-by-rotation (CEFR) technique was originally developed to fabricated high fidelity replicas of biotemplates such as butterfly wings [34] and fly eyes [35] as well as micro-scale resonators [36]. The CEFR technique produces a conformal thin film that consists of many individual parallel columns. The resulting film is analogous to a child's pin toy in that the individual pins conform to the underlying surface and replicate that surface along the tops of the parallel columns. With the CEFR technique, a substrate is affixed to a substrate stage which is tilted to a fixed angle measured between the plane of the substrate stage and the direction of the incident vapor flux. The substrate stage is then rapidly rotated about its surface normal. The self shadowing of the initial nucleation sites and competitive growth as the nucleation sites develop lead to a columnar morphology in thin films deposited using the CEFR technique. This morphology is more closely investigated when discussing the columnar thin film development of fingermarks in Ch. 3.

For a highly non-planar substrate affixed to a stationary stage, the angle at which a directional vapor flux falls upon the substrate can range from 0 to 90 deg [33]. The angle at which the vapor flux arrives at a substrate can greatly affect the deposition rate and film morphology [31]. As such, one would expect poor conformality and uniformity over a non-planar substrate when using a film deposition method such as thermal evaporation.

In order to compensate for this variation, the motion of the substrate can be tailored to produce a more conformal and uniform film [33]. This is done by periodically and rapidly changing the direction from which the incident vapor flux is locally impinging on the substrate. This is achieved by rapidly rotating the substrate stage about its surface normal while also periodically

rocking the stage about an axis lying wholly in the the plane of the stage and perpendicular to the direction of the vapor flux. This process had originally been developed to improve the conformality of thin films deposited on the compound eye of a blowfly [33]. This method of depositing conformal thin films was dubbed the modified-CEFR technique and its use for the fabrication of artificial beetle decoys is examined in Ch. 2.

By introducing tailored motion of the substrate stage, it is also possible to endow the conformal thin film with a morphology that improves its performance or gives the film some new functionality [31]. This type of tailored film morphology is implemented to enable the observation of a new type of surface wave, as described in Chaps. 6 and 7. The deposition of improved conformal thin films by thermal evaporation, and an ability to produce films with specific morphology allow for several novel applications of thermally evaporated conformal thin films.

1.4 Settings to Evaluate the Efficacy of Thermally Evaporated Conformal Thin Films on Non-Traditional /Non-Planar Substrates

Three settings which demonstrate the efficacy of thermally evaporated conformal thin films are presented in this dissertation. In each setting, the distinctive morphology of the film allows for a specific application.

1.4.1 Artificial Beetle Decoys

Artificial visual decoys for the invasive species commonly known as the emerald ash borer (EAB) [37,38] were fabricated through a bioreplication process which makes use of thermally evaporated conformal thin films, electroforming, and several casting steps to produce a pair of dies that can be used to pattern a polymer sheet upon which a Bragg reflector was deposited [39] to provide

iridescent color which matches the targeted species. The decoys for the EAB exploit the mating behavior of this species, wherein an overflying male EAB will first visually spot a female at rest in the ash canopy, and then execute a pouncing maneuver where the male lands directly upon the female [40, 41]. By cuing this behavior with an artificial decoy which can be mass produced, the possibility arises for a more effective trap to monitor and control the spread of this destructive invasive species. Through preliminary studies it was found that (i) both the overall shape and fine surface features must be present to attract male EAB, and (ii) decoys with color produced by paint will attract male EAB as well as decoys using a Bragg reflector for coloration.

1.4.2 Columnar-Thin-Film Development of Fingermarks

Fingermarks have long been used to identify the individual who left them behind when he/she touched an object with the friction ridges of his/her hands [42]. In many cases, the fingermark which is left behind consists of sebaceous secretions which are not visible under normal conditions [43]. In order to make the fingermarks visible and identifiable, they are traditionally developed by either a physical technique which relies on a material preferentially sticking to sebaceous materials or a chemical technique which relies on a reaction with material within the fingermark [44, 45]. I have optimized a new technique which relies on the topology of the fingermark to make it more easily visible. This technique utilizes a columnar thin film (CTF) deposited over both the fingermark and underlying substrate [46]. The CTF is produced by the conformal-evaporated-film-by-rotation method, wherein the substrate with the fingermark upon it is held obliquely with respect to a vapor flux in a vacuum chamber. The substrate is then rapidly rotated about a central normal axis passing through it, thereby resulting in a conformal film with columnar morphology. This technique was optimized for several forensically relevant substrates and compared with traditional development techniques. CTF development was found to be superior to traditional techniques in several cases. Use of the CTF technique was investigated for several types of particularly difficult to develop fingermarks such as those which consist

of both bloody and non-bloody areas, and fingermarks on fired cartridge casings. Additional experiments were conducted to compare the sensitivity of conventional techniques with the CTF technique. Finally, the CTF technique was compared to another thin-film fingermark development technique called vacuum-metal deposition. The resulting thin-film morphologies of each technique and efficacy at developing fingermarks on several forensically relevant substrates were compared.

1.4.3 Experimental Observation of the Dyakonov–Tamm Wave

The Dyakonov–Tamm wave is an electromagnetic surface wave that was predicted to exist at the interface of two dielectric materials at least one of which is periodically nonhomogeneous and anisotropic [47]. In order to make the first experimental observation of the Dyakonov–Tamm wave, the prism-coupled configuration was utilized to excite a Dyakonov–Tamm wave guided by the interface between a dense (and isotropic) magnesium-fluoride thin film and a zinc-selenide chiral sculptured thin film. In this configuration, the excitation of a Dyakonov–Tamm wave is indicated by a reflection dip that occurs at the same angle of incidence independent of the thickness of each partnering material, beyond some threshold, as well as the polarization state of the incident light.

This observation was then repeated in the grating-coupled configuration. The same partnering materials were used with the exception that the planar magnesium-fluoride layer was replaced with a periodically corrugated magnesium-fluoride layer. This required the deposition of the zinc-selenide chiral sculptured thin film on a non-planar substrate while maintaining the proper structure to allow for the propagation of the Dyakonov–Tamm wave.

1.4.4 Differences Between the Selected Settings

Each setting demonstrates a morphology produced to allow for a specific application. A dense conformal thin film is deposited on a highly non-planar biological substrate such as a beetle to

enable a method of mass producing replicas of the biotemplate. A conformal thin film with columnar morphology is deposited on a planar substrate with undulating features composed of a radically different material (i.e., a fingermark) than the substrate to reproduce the topology of the substrate with high fidelity. A film with a well engineered helical morphology is deposited on a periodically decorated substrate to enable the launch of a electromagnetic surface wave that had not been previously observed experimentally.

These settings also highlight the use of thermally evaporated conformal thin films to coat features of varying length scales. In conformally coating a beetle for bioreplication, the ability to capture the overall macroscopic shape of the beetle on the centimeter scale as well as reproducing the micrometer-scale surface features that pattern the entire beetle was necessary. While not necessary in this setting, the modified-CEFR technique adopted had previously been demonstrated as capable of capturing features which were $\sim$ 200-nm in diameter [48]. In developing fingermarks with CTFs, the ability to conformally coat micro-scale features which are found over substrates that are several centimeters in size was necessary. The observation of the Dyakonov–Tamm waves required the coating of periodic features which are $\sim$ 100-nm in size.

The three settings are vastly different in the materials utilized both as substrates and thin films. In the first setting, a metal was deposited upon a relatively hard substrate of biological origin. In the second setting, several metals, semiconductors, insulators, and organic materials were deposited upon both solid substrates of various materials and the oily emulsions of which sebaceous fingermarks are composed. In the third setting, more traditional substrates and evaporants were utilized.

The final way in which the settings differed was in the critical features of the thin films produced. In the first setting, it was critical that the overall shape and micro-scale structure of the beetle be closely reproduced. In the second setting, the thin film was required to produce a visual contrast between the substrate and the fingermark. In the third setting, the nanoscale morphologies of the thin films had to be precisely maintained to produce the desired optical

properties.

1.5 Objectives of Dissertation

The objectives of the research conducted for this dissertation were to:

(a) demonstrate that some of the limitations of thermal evaporation for depositing conformal thin films on non-planar substrates can be overcome;

(b) demonstrate that conformal thin films can be deposited on non-planar/non-traditional substrates without damaging the substrates; and

(c) evaluate the adequacy and the efficacy of conformal thin films of diverse morphologies in three distinct settings.

1.6 Organization of Dissertation

In Ch. 2 a process for fabricating artificial decoys for an invasive species known as the emerald ash borer is presented. Several steps in this process rely on the deposition of a dense conformal thin film directly onto the surface of a specimen of the emerald ash borer. Because of the sensitivity of such a substrate to heat and chemicals, a thermally evaporated conformal thin film presents a suitable thin-film-deposition technique.

Chapter 3 describes the development, refinement, and evaluation of a new method for developing fingermarks for forensic identification. In this setting, the advantage of developing fingermarks with thin films having vertical-columnar morphology is shown by comparing fingermarks developed with (i) dense-thin-film morphology, (ii) slanted-columnar thin-film morphology, and (iii) vertical-columnar thin-film morphology.

Before taking on the task of experimentally observing a new class of surface electromagnetic waves known as Dyakonov–Tamm waves, it was necessary to familiarize myself with the mod-

eling of electromagnetic surface waves. This task was initiated by modeling a simpler surface wave known as a Tamm wave. In Ch. 4 the excitation of Tamm waves in the grating-coupled configuration is theoretically investigated as a warm-up problem before beginning work on the Dyakonov–Tamm wave.

After gaining experience in modeling electromagnetic surface waves, I set out to model the excitation of a Dyakonov–Tamm wave in the prism-coupled configuration. This work is presented in Ch. 5. Various parameters of the pairing of materials that constitute the interface along which the Dyakonov–Tamm wave can propagate were varied in order to determine their effects on the excitation of the Dyakonov–Tamm wave. By establishing trends and acceptable ranges for each parameter, a more detailed picture of what would be the constitutive and morphological requirements of the partnering materials that would support the propagation of the Dyakonov–Tamm wave was brought into focus.

Having a solid theoretical model from which to design the interface which would support the propagation of the Dyakonov–Tamm wave, potential partnering materials were selected and efforts to make an experimental observation of the Dyakonov–Tamm wave initiated. In Ch. 6 the process for fabricating an interface which will support the Dyakonov–Tamm wave is described along with the experiment and corresponding results which represent the first experimental observation of the Dyakonov–Tamm wave.

The interface which was found to support the propagation of the Dyakonov–Tamm wave in Ch. 6 was subsequently modified to allow for the Dyakonov–Tamm wave to be excited in a grating-coupled configuration. In Ch. 7 the process for fabricating the interface which allows for the grating-coupled excitation of the Dyakonov–Tamm wave is given along with the experiment to observe the wave in this configuration.

Finally, Ch. 8 concludes this dissertation and presents potential future work. If the reader is only interested in portions of this dissertation, Chapters 2 and 3 can be read on an individual basis, while Chapters 5, 6, and 7 would be best read in sequence together.

1.7 List of Papers Published, Under Review, or in Preparation for this Dissertation

(i) Pulsifer, D. P., Lakhtakia A., Narkhede, M. S., Domingue, M. J., Post, B. G., Kumar, J., Martín-Palma, R. J., and Baker, T. C., "Fabrication of polymeric visual decoys for the male emerald ash borer (*Agrilus planipennis*)," *Journal of Bionic Engineering* **10**, 129–138 (2013).

(ii) Muhlberger, S. A., Pulsifer, D. P., Lakhtakia, A., Martín-Palma, R. J., and Shaler, R. C., "Optimized development of fingermarks on non-porous forensically relevant substrates with conformal thin films," *Journal of Forensic Science*, doi: 10.1111/1556-4029.12307.

(iii) Williams, S. F., Pulsifer, D. P., Lakhtakia, A., and Shaler, R. C., "Columnar-thin-film-assisted visualization of depleted sebaceous fingermarks on nonporous metals and hard plastics," *Journal of Forensic Sciences*, under review.

(iv) Williams, S. F., Pulsifer, D. P., Lakhtakia, A., and Shaler, R. C., "Visualization of partial bloody fingermarks on nonporous substrates using columnar thin films," *Forensic Science International*, under review.

(v) Williams, S. F., Pulsifer, D. P., Shaler, R. C., Ramotowski, R., Brazelle, S., and Lakhtakia, A., "Comparison of the columnar-thin-film and vacuum metal deposition techniques to develop sebaceous fingermarks on nonporous substrates," *Journal of Forensic Sciences*, submitted.

(vi) Pulsifer, D. P., Muhlberger, S. A., Williams, S. F., Shaler, R. C., and Lakhtakia, A., "An objective fingerprint quality-grading system," *Forensic Science International* **231**, 204–207 (2013).

(vii) Pulsifer, D. P., Faryad, M., and Lakhtakia, A., "Grating-coupled excitation of Tamm waves," *Journal of the Optical Society of America B* **29**, 2260–2269 (2012).

(viii) Pulsifer, D. P., Faryad, M., and Lakhtakia, A., "Parametric investigation of prism-coupled excitation of Dyakonov–Tamm waves," *Journal of the Optical Society of America B* **30**, 2081–2089 (2013).

(ix) Pulsifer, D. P., Faryad, M., and Lakhtakia, A., "Observation of the Dyakonov–Tamm wave," *Physical Review Letters*, accepted for publication.

(x) Pulsifer, D. P., Faryad, M., and Lakhtakia, A., "Grating coupled excitation of the Dyakonov–Tamm wave," *Electronic Letters*, in preparation.

Chapter 2

Fabrication of Artificial Beetle Decoys[‡]

In order to test the efficacy of the modified-CEFR process described in Sec. 1.3.2, the setting of fabricating a beetle decoy through a bioreplication process was developed. In this setting, a dense conformal thin film of nickel was used as the working surface of a negative die which was used to impart the surface features found on the elytra of the beetle to a colored polymer sheet. Through the modified-CEFR process, the fine features found on the beetle along with its centimeter-scale shape were captured in the negative die. This die was used to fabricate nearly 100 artificial decoys of the selected beetle. Thereby, it was demonstrated that a dense and robust conformal thin film can be deposited on a non-traditional/non-planar substrate to produce useful devices.

2.1 Chapter Summary

Artificial visual decoys for the invasive species commonly known as the emerald ash borer (EAB) were fabricated through a bioreplication process which makes use of thermally evaporated conformal thin films, electroforming, and repeated castings to produce a pair of dies that can be used to pattern a polymer sheet upon which a Bragg reflector was deposited to provide iridescent

[‡]This chapter is partially based on: Pulsifer, D. P., Lakhtakia A., Narkhede, M. S., Domingue, M. J., Post, B. G., Kumar, J., Martín-Palma, R. J., and Baker, T. C., "Fabrication of polymeric visual decoys for the male emerald ash borer (*Agrilus planipennis*)," *Journal of Bionic Engineering* **10**, 129–138 (2013).

color which matches the targeted species. The decoys for the EAB exploit the mating behavior of this species, wherein an overflying male EAB will first visually spot a female at rest in the ash canopy, and then execute a pouncing maneuver to land directly upon the female. By cuing this behavior with an artificial decoy which can be mass produced, the possibility arises for a more effective trap to monitor and control the spread of this destructive invasive species.

2.2 Introduction

The invasive species, *Agrilus planipennis* is an iridescent wood-boring beetle native to Asia. In North America this pest species is commonly known as the emerald ash borer (EAB). The EAB was accidentally introduced to Michigan in the late 1990s [37, 38] and has since spread through many forests with ash trees in both the United States and Canada. The developmental stages of the EAB take place in ash trees during which time they bore along the nutrient transporting layers of the host trunk [38]. Within three years of the initial infestation, this disruption of nutrient flow results in the death of the infected tree [37, 38].

Entomologists found that the male EAB locates a potential mate visually while flying over the ash canopy. Once a female is spotted, the male executes a pouncing maneuver whereby he rapidly descends on to the female at rest of an ash leaf. [40, 41]. It is thought that the male recognizes the iridescent green coloration [49] of its potential mate's hard wing coverings, known as elytra, as they contrast with ash-leaf background. This behavior has been cued by entomologists using dead EAB pinned to ash leaves to lure the males. The dead EAB were first washed to remove any semiochemicals to ensure that the behavior was being cued visually. When the decoy was coated with a spray-on adhesive, the pouncing male could be effectively trapped [41].

In order to exploit this behavior to lure and trap EAB males on a larger scale, I developed a process by which the upper surface of the EAB could be bioreplicated [14]. The aim of this bioreplication process was to produce decoys *en masse* which could be used in place of dead EAB specimen [50]. This process utilizes a positive die and a negative die which are directly replicated from a specific EAB to form a polymer sheet into the same shape, and with the same surface features as the EAB. When a quarter-wave-stack Bragg reflector is present on the polymer sheet, the iridescent coloration of the original EAB can also be reproduced.

For the fabrication of a negative die, a thermally evaporated nickel film was conformally

deposited on to the elytra of a dead EAB female. The nickel thin film was then reinforced through electroforming. This process was selected as it can closely reproduce the non-planar surface of the beetle without causing undesirable damage. Indeed, it had been established during the replication of blowfly corneas [48] that a lateral resolution of about 200 nm is achievable. The complementary positive die was fabricated through successive castings of the negative die to ensure a close match between the positive and negative dies. As the EAB male's pouncing behavior is suspected to be initiated largely by the iridescent green color of the elytra, collaborators provided me with a quarter-wave-stack Bragg reflector [51] produced by spin coating [52, 53] alternating layers of poly(vinyl cinnamate) (PVCN) and poly(acrylic acid) (PAA) on a poly(ethylene terephthalate) (PET) sheet. The Bragg reflector was designed to produce peak reflectance at 550-nm wavelength with a relatively narrow bandwidth, in order to mimic the coloration of the EAB.

Here I present the entire process to produce multiple decoys from a single EAB female as well as results from a preliminary field test which demonstrate the effectiveness of the fabricated decoys. Section 2.3 is focused on the fabrication of the negative die, Sec. 2.4 contains a description of the procedure to fabricate the complementary positive die, and Sec. 2.5 deals with the production of the quarter-wave-stack Bragg reflector. The scalable production of visual decoys is discussed in Sec. 2.6, and the results from a preliminary field test are presented in Sec. 2.7. Additionally, a biomimetic decoy fabricated through an additive manufacturing is discussed in Sec. 2.8.

2.3 Fabrication of Nickel Negative Die

2.3.1 Substrate Preparation

A biotemplate—a dead EAB female—was mounted in polydimethylsiloxane (PDMS) on a glass slide which had a layer of kapton tape to serve later as a delamination layer. The mounting was done by placing the biotemplate on the slide and then pouring PDMS over it. Accordingly, a smooth transition was produced between the biotemplate and the slide, which is desirable (i) to eliminate areas that would be shadowed during the deposition of nickel vapor on the biotemplate (Sec. 2.3.2) and (ii) to reduce overhangs when the resulting conformal coating of nickel would be reinforced by electroforming (Sec. 2.3.3). After the PDMS was cured, it was peeled away from the upper surface of the biotemplate's elytra and head to expose the surface of interest. Finally,

the slide-mounted EAB specimen was sonicated in ethanol to remove any residue.

Figure 2.1(a) shows a dead EAB female mounted on a glass slide with PDMS. Both elytra and the head are exposed and will serve together with the PDMS mounting as a non-planar substrate for the deposition of a conformal coating of nickel.

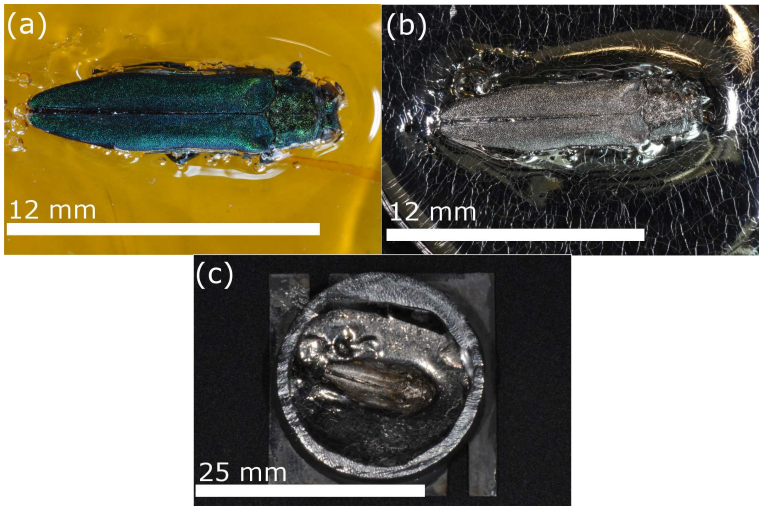

Figure 2.1: Production of a negative nickel die. (a) Photograph of a non-planar substrate comprising a dead EAB female mounted on a glass slide with PDMS. The PDMS mounting allows for a smooth transition between the biotemplate and the glass slide. (b) Photograph of the slide-mounted EAB female from (a) after being coated with ∼500 nm of nickel in two successive CEFR runs. (c) Photograph of the electroformed negative die soldered into a steel ring and mounted to a stainless steel plate.

2.3.2 Conformal Coating of Nickel

In order to conformally coat the non-planar substrate, the modified-CEFR method was adopted [33]. The CEFR method had originally been developed to produce conformal coatings on non-planar substrates such as butterfly wings [34] and fingermarks [54], and was modified for highly lenticular substrates such as the eyes of insects [33]. The modified-CEFR method is implemented in a vacuum chamber containing both the substrate to be coated and a receptacle containing the material to be evaporated towards that substrate. A vapor flux generated from the material is obliquely directed towards the substrate. Two programmable stepper motors allow a stage holding the substrate to be manipulated in order to produce a uniform coating.

For coating the EAB specimen, nickel was evaporated from a long and narrow receptacle made of tungsten. During deposition, the pressure in the vacuum chamber was maintained at

$\sim 10^{-5}$ Torr and a current of $\sim$ 90 A was passed through the boat to maintain a deposition rate of 1 nm s^{-1}. The substrate-holding stage was periodically rocked about a fixed axis in the stage plane through incident vapor flux angles χ_v (See Fig. 2.2) between 10 and 90 deg. Simultaneously, the stage was rotated about a central normal axis at 120 rpm. A ∼500-nm-thick film was deposited in two successive CEFR runs, each run depositing ∼250 nm of nickel. The use of two runs instead of just one run arose from the limited capacity of the tungsten boat. Any oxidation occurring on the nickel surface between the two runs did not have a deleterious effect on the second run.

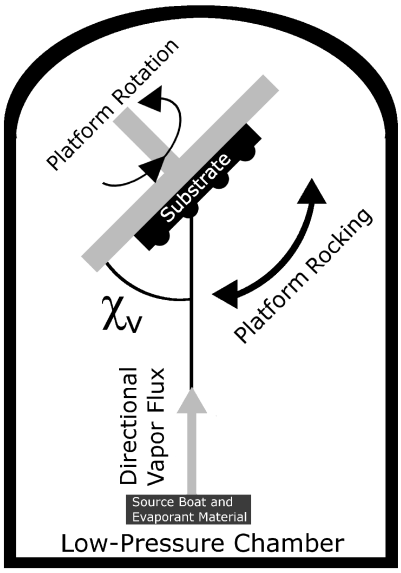

Figure 2.2: Schematic of the CEFR method. In a vacuum chamber, a collimated vapor flux is directed towards a substrate mounted on a stage that rotates rapidly about a central normal axis. The stage may also be made to rock slowly about an axis lying wholly in the stage plane so that the angle χ_v between the average direction of the vapor flux and the stage plane varies periodically, provided the exposed surface of the substrate is significantly lenticular.

Figure 2.1(b) shows the slide-mounted biotemplate after being conformally coated with nickel. The upper surface of the nickel coating is meant to serve as a seed for the electroforming step, and the lower surface of the coating is supposed to later function as the active surface for stamping with the negative nickel die. Based on similar coatings on the eyes of insects [48], the fidelity of bioreplication should be very good at the ∼200-nm length scale, as the nickel coating should have grains not exceeding ∼20 nm in maximum cross-sectional diameter. However, nanoscale

fidelity is not needed, as the scanning electron microscope (SEM) image in Fig. 2.3(a) shows that the elytron has small-scale features at ∼10-μm length scale. The the SEM image in Fig. 2.3(b) confirms that the negatives of these features are reproduced in the nickel coating,

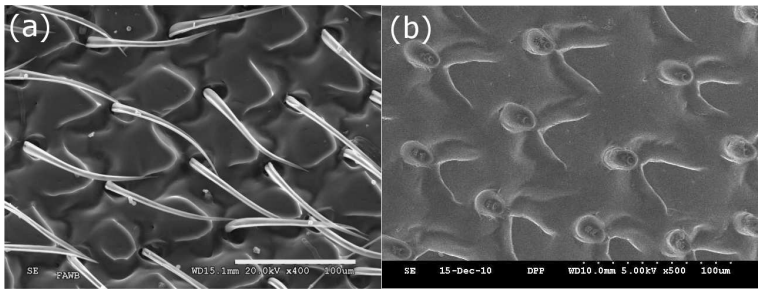

Figure 2.3: SEM images of (a) the elytron of an EAB at 400× magnification, and (b) the functional surface of the ∼500-nm-thick nickel coating at 500× magnification. As the surface of the coating is the negative of the elytron surface, the roots of the cilia on the elytron in (a) appear as elliptical depressions in (b).

2.3.3 Electroforming

Electroforming is necessary to build up the nickel coating on the biotemplate in order to produce a negative die able to withstand the forces exerted when a polymer sheet is to be stamped [55].

Electroforming of the nickel-coated biotemplate was carried out in three stages of successively increasing electric current. Three different electroforming stages were implemented to minimize grain size at the working surface of the die while also allowing acceptable growth rates. During all three stages, the electroforming bath was maintained at ∼ 50 °C for 2 days. The current was set at 20 mA for the first stage, 40 mA for the second, and 60 mA for the last stage. The electroformed layer produced was ∼100 μm in thickness. After the electroforming step, the biotemplate was removed to leave behind a negative die of nickel.

2.3.4 Mounting of Negative Die

Although ∼100-μm thick, the electroformed nickel die has an irregular shape with the negative of the biotemplate protruding out of the plane of the majority of the die area. To facilitate the application of pressure that would be required to stamp polymer sheets, the negative nickel die was soldered into a steel ring. In this way, the irregular shape of the nickel die was recessed into a solid fixture. The ring-mounted die was then attached to a stainless-steel sheet with an

electrically insulating epoxy. The stainless-steel sheet serves later as a heating element for the negative die when the decoys are stamped (Sec. 2.6). Figure 2.1(c) shows the electroformed negative die soldered into a steel ring and attached to a stainless-steel sheet.

2.4 Fabrication of Epoxy Positive Die

To produce the epoxy positive die, the nickel negative die was first filled with PDMS. After it cured, the PDMS positive casting was removed from the nickel negative die, mounted to a glass slide with kapton tape, and then conformally coated with chalcogenide glass of nominal composition $Ge_{28}Sb_{12}Se_{60}$ using the CEFR method. The resulting structure is presented in Fig. 2.4(a).

The ∼1000-nm-thick coating of chalcogenide glass served simply as a diffusion barrier for the next step, wherein the structure shown in Fig. 2.4(a) was submerged in PDMS. After curing, the PDMS negative casting was pulled away from the PDMS positive. This PDMS negative, shown in Fig. 2.4(b), is a close match of the nickel negative die.

The negative casting made of PDMS was then filled with an epoxy. Once the epoxy was cured, the PDMS negative casting was peeled away to leave behind a positive epoxy die of the biotemplate. This strategy was implemented to allow for the closest match possible between the positive and negative dies. The positive epoxy die was attached to a stainless-steel sheet for easy handling as well as heating during the stamping process (Sec. 2.6). Figure 2.4(c) shows the epoxy positive die after removal from the PDMS negative. The epoxy in the positive die thus fabricated was trimmed to remove excess material and allow clearance for a poly(ethylene terephthalate) (PET) sheet to be stamped. Figure 2.4(d) shows the positive epoxy die which can be mated with the negative nickel die of Fig. 2.1(c).

2.5 Fabrication of Quarter-Wave-Stack Bragg Reflector

It had been ascertained earlier [50] that a PET replica can be produced by melting a PET sheet in a heated negative die and then pressing the positive die into the molten PET by hand. This process did not produce a satisfactory replica, because it resulted in the destruction of the Bragg reflector placed on the PET sheet to provide the desired coloration. Equally significantly,

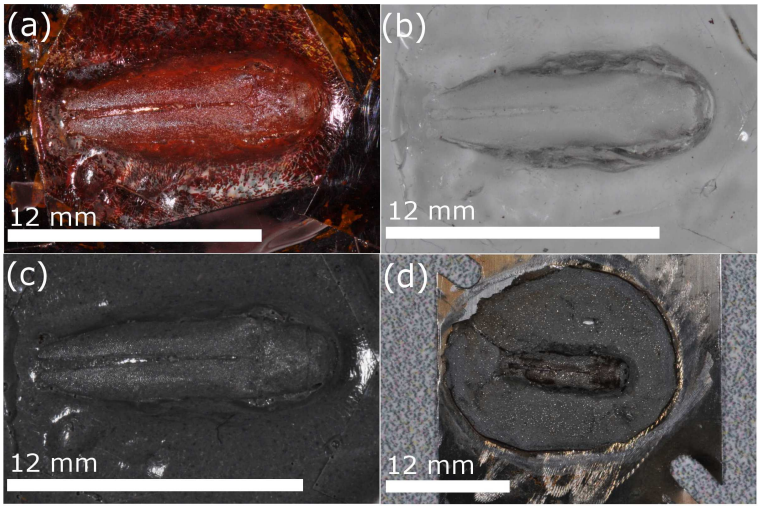

Figure 2.4: Production of a positive epoxy die. (a) Photograph of the PDMS positive cast from the negative nickel die. The PDMS positive is coated with a 1000-nm-thick coating of chalcogenide glass of nominal composition $Ge_{28}Sb_{12}Se_{60}$. (b) Photograph of the PDMS negative produced from the PDMS positive shown in (a). (c) Photograph of the positive epoxy die cast from the PDMS negative shown in (b). (d) Photograph of the positive epoxy die after mounting to a stainless-steel sheet and trimming to allow clearance for a PET sheet to be stamped.

the replica had a translucent white appearance, which would not lure any EAB male. This is because EAB elytra have an iridescent green coloration produced by quarter-wave stacking of sub-cuticular layers, which is known from many beetle species to produce strong structural colors without the use of pigments [51, 56]

As is evident in the SEM image shown in Fig. 2.5(a), the outer region of the EAB elytron contains four ∼135-nm-thick layers of alternating refractive indexes. Thus the iridescent green coloration is produced by a quarter-wave stack Bragg reflector that develops during the pupal stage, and this coloration is not significantly disturbed by the presence of cilium-supporting ∼70-μm dimples that can be seen in Fig. 2.3(a). Reflectance spectrophotometer measurements show peak reflectance from EAB elytra to be close to 540-nm wavelength, quite similar to both ash leaflets and oak leaves and also similar to the elytra of *A. biguttatus*, an aggressive European oak-feeding species (Fig. 2.5(b)).

Whether the EAB males are lured simply by the iridescent green coloration of the EAB females or also by the small-scale structures is an open question that I had also hoped to answer at the beginning of this project.

To mimic the natural Bragg reflector found in the EAB elytra, alternating layers of PVCN

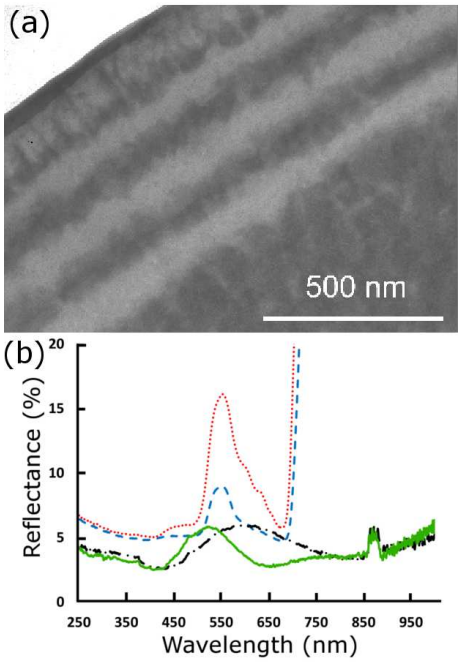

Figure 2.5: (a) Transmission electron micrograph of a cross-section of a female EAB elytron, showing four alternating layers of differing refractive indexes $\sim$ 135-nm thickness. (b) Reflectance spectrophotometer measurements of the elytra of a female EAB, *A. planipennis* (solid green line), and an aggressive European oak-feeding species in the same genus, *A. biguttatus* (dotted-and-dashed black line), compared to the reflectance profiles of an ash leaflet (dotted red line) and an oak leaf (dashed blue line). [Courtesy of Dr. Thomas Baker and Dr. Michael Domingue]

and PAA were spin-coated on one side of a 3×3 cm^2 PET sheet. These polymers were chosen as their refractive indexes differ by 0.19, which is quite large. Furthermore, the solubilities of both polymers in orthogonal solvents are very different. PVCN (0.9 wt %) and PAA (1.2 wt %) solutions in chloroform and methanol, respectively, were used for spin coating. Bragg stacks were fabricated by consecutively coating 15 bilayers of PAA and PVCN at 1500 rpm. Since PAA and PVCN are insoluble in chloroform and methanol, respectively, the addition of a new layer via spin coating did not damage prior layers. The transmission spectrum of the resulting PET sheet with a quarter-wave-stack Bragg reflector is shown in Fig. 2.6(a). These measurements were performed using a Perkin–Elmer Lambda-9 spectrophotometer, with an uncoated PET sheet as a reference.

Thereafter, the other side of the PET sheet was coated with black ink as an absorber layer in order to enhance the spectrally selective reflection. The resulting PET sheet with a quarter-

wave-stack Bragg reflector on one side and black absorber layer on the other side is shown in Fig. 2.6(b). The reflectance of the doubly coated PET sheet as a function of wavelength is shown in Fig. 2.6(c). These figures confirm the desired green coloration.

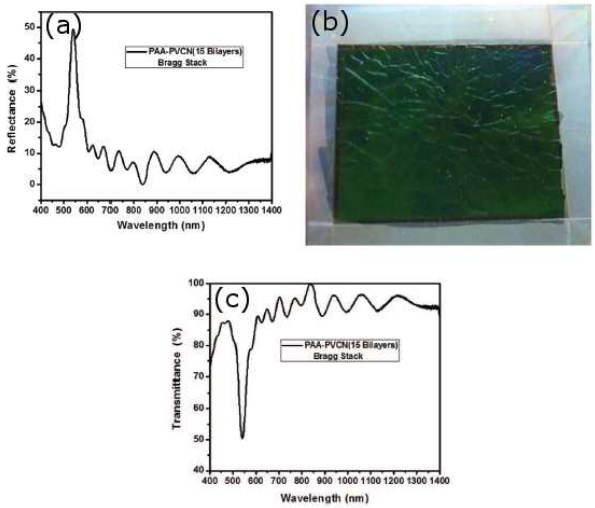

Figure 2.6: (a) Measured transmittance spectrum of an unstamped PET sheet with a quarter-wave-stack Bragg reflector on one side and without a black absorber. (b) Photograph of an unstamped PET sheet with a quarter-wave-stack Bragg reflector on one side and a black absorber layer on the other. (c) Measured reflectance spectrum of an unstamped PET sheet with a quarter-wave-stack Bragg reflector on one side and a black absorber on the other side. [Courtesy of Dr. Jayant Kumar and Mahesh Narkhede]

2.6 Fabrication of Visual Decoys

Four decoy types were fabricated to be tested against dead EAB females. An EAB female is shown in Fig. 2.7(a). The first type was simply the quarter-wave-stack Bragg reflector trimmed to resemble the silhouette of an EAB as shown in Fig. 2.7(b). The remaining three decoy types were fabricated by hot stamping PET sheets, each coated with a quarter-wave-stack Bragg reflector on the upper side and a black absorber layer on the lower side, as described in Sec. 2.5. The PET sheet was pressed between the electrically heated positive and negative dies and allowed to cool under pressure. Once cooled, the now patterned sheet was removed from the dies and the excess material trimmed away.

Figures 2.7(c-e) show decoys prepared in this way with some variation. The decoy shown in

Fig. 2.7(c) was stamped with enough force to leave the general shape of the beetle and some surface details but do minimal damage to the quarter-wave-stack Bragg reflector. The decoy shown in Fig. 2.7(d) was stamped more heavily in order to impart the decoy with the surface features of the EAB at the sacrifice of a portion of the Bragg reflector. Finally, the decoy shown in Fig. 2.7(e) was stamped heavily from a PET sheet which had a quarter-wave-stack Bragg reflector on its upper side prior to stamping, but without a black absorber layer on its lower side. Following the heavy stamping, decoys of this type had their lower sides painted first with a commercially available metallic emerald green paint and then a black absorber layer.

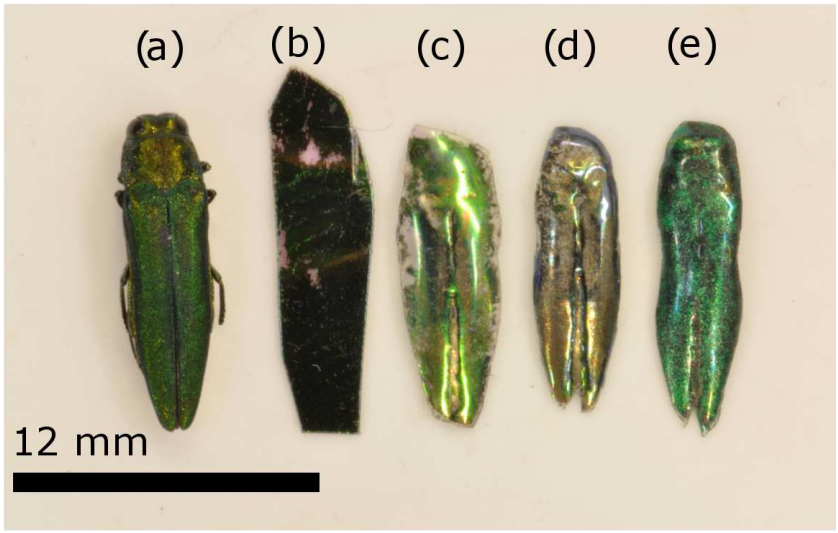

Figure 2.7: (a) A dead EAB female is shown for reference. (b) A quarter-wave-stack Bragg reflector cut into a rough silhouette of an EAB. (c) A visual decoy produced by lightly stamping a PET sheet coated with a quarter-wave-stack Bragg reflector on the upper side and a black absorber layer on the lower side. Note that the quarter-wave-stack Bragg reflector is intact over much of the decoy. (d) A visual decoy produced similarly to the one shown in (c) but it was stamped more heavily. This yielded more fine features at the expense of area where the quarter-wave-stack Bragg reflector survived. (e) A visual decoy produced by heavily stamping a PET sheet, then painting the lower side first with emerald metallic paint and then a black absorber layer.

2.7 Field Tests

Visual decoys of five types—(a) dead EAB females, (b) unstamped Bragg reflectors trimmed to have a silhouette similar to an EAB, (c) lightly stamped Bragg reflectors, (d) heavily stamped Bragg reflectors, and (e) heavily stamped and painted metalic emerald on the backside—were

Table 2.1: Result of an experiment designed to compare the effectiveness of decoys of type (c–e) against control decoys of type (a–b). This experiment was carried out with decoys pinned to sticky traps which were checked each day for captured EAB. [Courtesy of Dr. Thomas Baker and Dr. Michael Domingue]

Decoy Type	Number of Traps Deployed	Number of Target Beetles Captured
(a) Dead EAB	6	4
(b) Unstamped Bragg	6	1
(c) Lightly Stamped Bragg	6	6
(d) Heavily Stamped Bragg	6	5
(e) Heavily Stamped and Painted	6	11

mounted on green plastic surfaces and sprayed with an adhesive. In this manner, several test traps of types (c–e) were made, all originating from the same dead EAB female. Control traps were made using decoys of types (a–b).

All of these traps were deployed in a preliminary field test conducted in June and July 2012. As the emergence of adult EAB in North America was premature in 2012 and because dead EAB females have been shown to work just as reliably in attracting a potentially destructive oak-feeding invasive pest species, *A. bigutattus*, as they do against EAB themselves [57], *A. biguttatus* field trapping tests of the visual decoys were conducted in Hungary. The results showed that traps of types (c–e) performed as well or better than the dead EAB female control decoy at attracting *A. biguttatus*. That the stamped visual decoys of all three types were much more successful in luring overflying *Agrilus* males than unstamped Bragg reflector traps provides evidence that not only should a decoy have the same silhouette, size, and color as an EAB female, but must also have the 3-dimensional shape and small-scale surface texture found on the elytra. Table 2.1 presents the result of one in a series of experiments designed to compare the effectiveness of decoys of types (c–e) against the control decoys of types (a–b), and Fig. 2.8 shows a photograph of an adhesive trap which had captured a male *A. biguttatus*.

A second experiment was conducted at a nearby site. In this experiment only decoys of types (a) and (c) were compared. The results of this experiment are summarized in Table 2.2.

Table 2.2: Result of an experiment designed to compare the effectiveness of decoys of type (c) against control decoys of type (a). This experiment was conducted in a location near the site of the results reported in Table 2.1. This experiment was carried out with decoys pinned to sticky traps which were checked each day for captured EAB. [Courtesy of Dr. Thomas Baker and Dr. Michael Domingue]

Decoy Type	Number of Traps Deployed	Number of Target Beetles Captured
(a) Dead EAB	6	17
(c) Lightly Stamped Bragg	6	19

Figure 2.8: Photograph of a test trap with an *Agrilus* male stuck to a visual decoy, thereby demonstrating that the visual decoys produced by us can initiate pouncing behavior. Field tests were conducted in Hungary. [Courtesy of Dr. Thomas Baker and Dr. Michael Domingue]

2.8 Fabrication of Emerald Ash Borer Decoys by Additive Manufacturing

The preliminary testing of bioreplicated decoys left open a question as to the need for an exact replica. It was found that the use of a metallic-emerald paint rather than a Bragg reflector could be used to attract EAB. One major issue left unresolved was if green coloration and overall shape were sufficient, or if fine-scale features on the elytra surface require reproduction for success. In order to resolve this issue, I fabricated a simplified biomimetic, not bioreplicated, EAB decoy through an additive manufacturing process. If successful decoys fabricated through additive

manufacturing would be attractive as they could be produced at a lower cost than bioreplicated decoys.

2.8.1 3D model of EAB

The production of a biomimetic EAB decoy began with a 3D rendering of the decoy. Figure 2.9 shows a profile drawing that was produced to roughly match that of the EAB. Features that were captured in the profile were the overall length, shape of the elytral region, and a slight dip between the beetle's head and the elytral region. The 2D profile was then rotated through 180 deg to produce a 3D model which roughly matched the shape and size of the original EAB. Figure 2.10 shows this 3D model which was produced using Solidworks® drafting software.

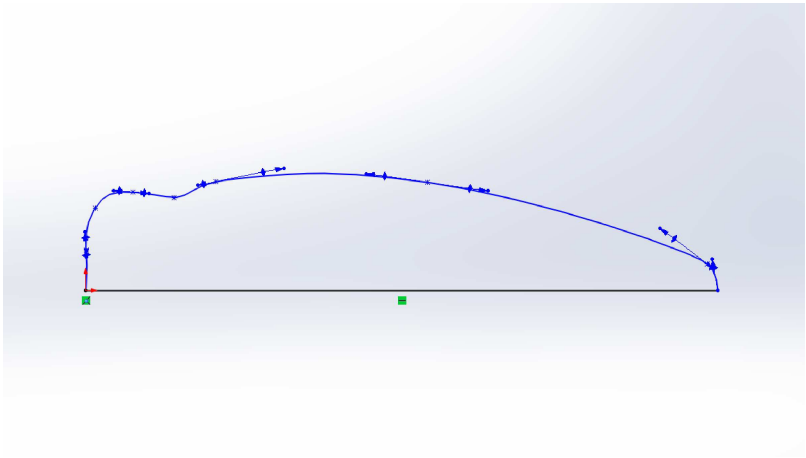

Figure 2.9: Profile of EAB.

2.8.2 3D Printing of Decoys

The 3D EAB model was then uploaded into the control software for a Dimension 1200es-SST (Stratasys, Edina, MN) 3D printer for additive manufacturing. In this process, the model was arrayed to allow the printing of 300 decoys. Each decoy was printed as 11 discrete layers, each $\sim$ 0.254 mm in thickness. Figure 2.11 shows a photograph of the decoy as it was produced by the additive manufacturing process.

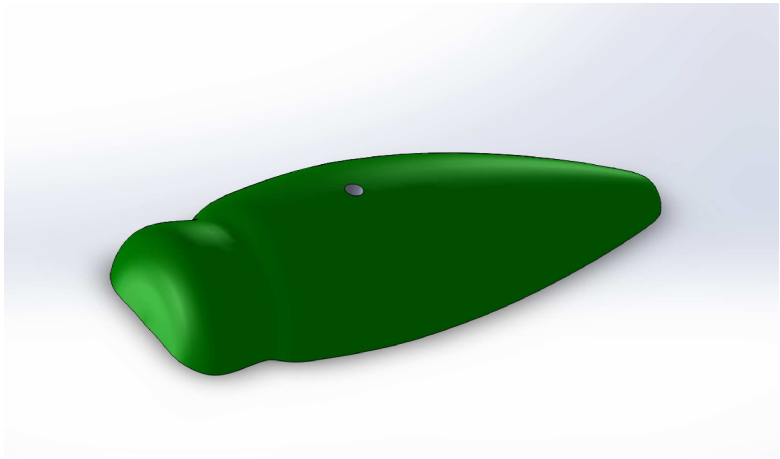

Figure 2.10: 180 deg solid rotation of the profile in Fig. 2.9 about its longitudinal axis

Figure 2.11: Unpainted decoy as it comes from the additive manufacturing equipment.

2.8.3 Painting of Decoys

One half of the decoys produced by the additive manufacturing equipment had their step structure smoothened prior to being painted. This was done by hand-rubbing each decoy with acetone. The acetone partially dissolved the ABS, which when combined with the rubbing, smoothed the step structure. All decoys were then painted with Testor's® Mystic Emerald spray paint. In

Fig. 2.12 a painted decoy with the stepped structure is shown, and in Fig. 2.13 a painted decoy with the smoothed structure is shown. Figure 2.14 shows a photograph of the 300 biomimetic decoys produced by additive manufacturing after they had been painted

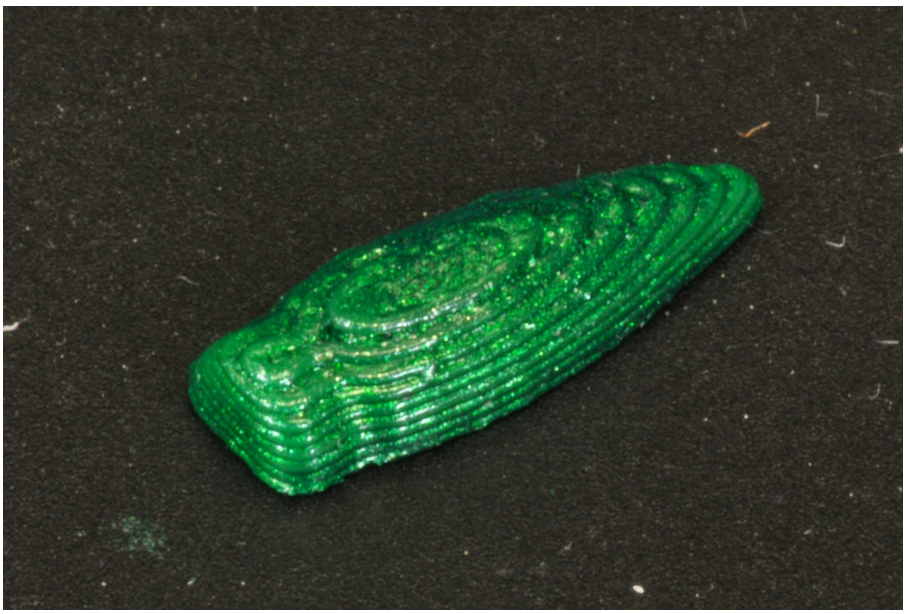

Figure 2.12: The unpainted decoy after being painted with a metallic emerald paint.

2.8.4 Field Testing of Additively Manufactured Decoys

In the summer of 2013 the additive manufactured biomimetic decoys underwent field testing on the Penn State campus to be compared with earlier bioreplicated and natural decoys. In this study, the decoys were pinned to ash leaves and video filmed. The video filming allowed for the observation of the pouncing behavior of the EAB. Once the pouncing behavior was initiated, one of four events would take place: (i) the beetle would divert without landing on either the decoy or the leaf, (ii) the beetle would divert from landing on the decoy and land somewhere nearby, (iii) the beetle would land directly on the decoy then leave, or (iv) the beetle would land on the decoy then attempt to copulate. Events of types (i) and (ii) were considered as failures while events of types (iii) and (iv) were considered as successes.

Table 2.3 summarizes the results of this experiment for decoys consisting of: dead EAB (a), dead European oak beetles, lightly stamped Bragg reflector decoys (c), heavily stamped and

Figure 2.13: The unpainted decoy after being smoothed with acetone and then painted with metallic emerald paint.

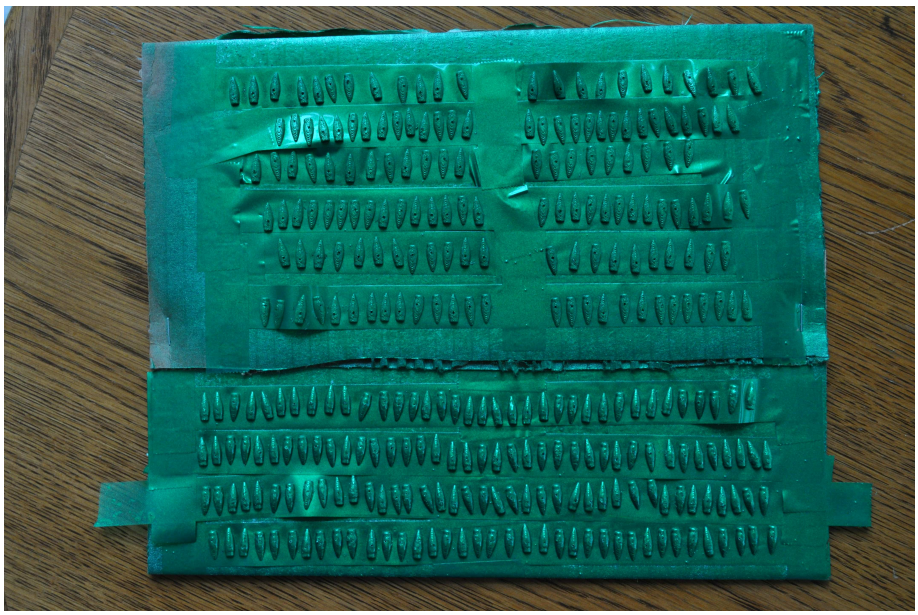

Figure 2.14: Photograph of 300 decoys produced by additive manufacturing after being painted.

painted decoys (e), and the additively manufactured decoys. Note that the decoys of types (c) and (e) were reused from previous years and may have undergone some degree of degradation.

Table 2.3: Result of an experiment designed to compare the effectiveness of dead EAB, dead European oak beetles, lightly stamped decoys with Bragg reflector, heavily stamped and painted decoys, and additive manufactured decoys. In this experiment the decoys were pinned directly to an ash leaf and filmed to observe the approach of an EAB. [Courtesy of Dr. Thomas Baker and Dr. Michael Domingue]

Decoy Type	Number of Approaches Observed	Number of Approaches Resulting in Direct Contact with Decoy	Ratio
Dead EAB (a)	32	31	0.97
Dead Oak Beetle	24	22	0.92
Lightly Stamped Bragg (c)	21	15	0.71
Heavily Stamped and Painted (e)	18	14	0.78
Additive Manufactured	15	1	0.07

In this experiment, the bioreplicated decoys performed much more closely to the dead beetle decoys than did the additively manufactured biomimetic decoys. This suggests that maintaining fine-scale elytral features is essential to a successful decoy for the EAB.

2.9 Concluding Remarks

Here I have presented a bioreplication procedure to make visual decoys to lure male emerald ash borers and other invasive pest species in genus *Agrilus*. This procedure involves the stamping of a polymer sheet with two dies directly replicated from a dead EAB female. The procedure is industrially scalable as nearly 100 decoys were produced from a single biotemplate.

Field testing of the visual decoys was carried out and preliminary results show them to be effective at cuing the aerial pouncing behavior from overflying males. The ineffectiveness of unstamped Bragg reflector control traps demonstrated that the visual decoys must have not only the iridescent green coloration but also the structure of the EAB elytra. The ineffectiveness of the additive manufactured decoys demonstrates that some quantity of the fine-surface features found on the EAB must also be maintained.

In this setting the efficacy of the modified-CEFR process described in Sec. 1.3.2 was demonstrated through the successful replication of the fine-scale surface features found on the elytra of the EAB while simultaneously capturing the overall shape of the EAB. This demonstrates that thermal evaporation can produce accurate and robust conformal thin films with dense morphology on non-traditional/non-planar substrates without damage. The die which integrated this conformal thin film was used to produce nearly 100 artificial decoys to lure the EAB.

Chapter 3

Columnar-Thin-Film Development of Fingermarks as Forensic Evidence[‡]

In the second setting for testing the efficacy of thermally evaporated conformal thin films on non-traditional/non-planar substrates, the development of sebaceous fingermarks placed forensically relevant substrates was selected. This setting demonstrates three key features of thermal evaporations: (i) compatibility with very temperature-sensitive substrates, (ii) capability of simultaneously coating substrates of vastly different chemical and physical properties, and (iii) an ability to conformally deposit films with a specific morphology which improves functionality.

3.1 Chapter Summary

Fingermarks have long been used to identify the individual who left them behind when they touched an object with the friction ridges of their hands. In many cases the fingermark which is left behind consists of sebaceous secretions which are not visible under normal conditions. In order to make the fingermarks visible and identifiable, they are traditionally developed by either a physical technique which relies on a material preferentially sticking to sebaceous materials or a chemical technique which relies on a reaction with material within the fingermark. I have optimized a new technique [46] which relies on the topology of the fingermark to make it more easily

[‡]This chapter is partially based on: Muhlberger, S. A., Pulsifer, D. P., Lakhtakia, A., Martín-Palma, R. J., and Shaler, R. C., "Optimized development of fingermarks on non-porous forensically relevant substrates with conformal thin films," *Journal of Forensic Sciences*, doi: 10.1111/1556-4029.12307.

visible. This technique utilizes a columnar thin film (CTF) deposited over both the fingermark and underlying substrate. The CTF is produced by the conformal-evaporated-film-by-rotation method, wherein the substrate with the fingermark upon it is held obliquely with respect to a vapor flux in a vacuum chamber. The substrate is then rapidly rotated about its surface normal resulting in a conformal film with columnar morphology. This technique was optimized for sebaceous fingermarks on several forensically relevant substrates and compared with traditional development techniques. CTF development was found to be superior to traditional techniques in several cases. Use of the CTF technique was investigated for several types of particularly difficult to develop fingermarks such as those which consist of both bloody and non-bloody areas, and fingermarks on fired cartridge casings. Additional experiments were conducted to compare the sensitivity of conventional techniques with the CTF technique. Finally, The CTF technique was compared to another technique which utilizes thin films called vacuum-metal deposition (VMD).

This chapter demonstrates the use of a thermally evaporated film to produce a conformal thin film with a specific morphology on a non-planar/non-traditional substrate. As fingermarks are fragile, the use of thermal evaporation allows them to be coated without damaging either the substrate or the fingermark. It is also demonstrated that vertical columnar morphology results in improved development when compared to either a dense film or a film comprising slanted columns.

3.2 Introduction

Fingermarks are the invisible impressions of the friction ridge patterns found on the hands that are left behind when an individual touches a surface. On contact with a surface, any material found on the friction ridges can be transfered to the substrate. Fingermarks are often a combination of secretions from sebaceous and eccrine glands found in human skin [43]. The eccrine secretion is 99% water which either evaporates or is absorbed in the sebaceous sectretion within a few hours. Fingermarks are of interest to forensic scientists and criminalists because they can be used to identify the perpetrator of a crime. The identification of an individual by their fingermarks is possible due to the fact that the pattern of the friction ridges is unique to each individual and does not change over an individual's lifetime [42].

Because they are not visible, fingermarks require some type of development process to be car-

ried out to enable visualization. Development techniques often rely on some type of physical or chemical reaction to make the fingermark visible. The most well known development technique relies on a powder adhering to the oily residue in the fingermark preferentially over the substrate [44]. Chemical techniques rely on a reaction between specific chemicals in the fingermark and the development agent [45]. If substrates can be returned to a laboratory for development, advanced techniques can be utilized. Such techniques include: chemical imaging [58,59], vacuum metal deposition (VMD) [60], vacuum cyanoacrylate fuming [61], and corrosion analysis [62,63]. A problem that forensic scientists often face is that multiple development techniques are needed to visualize a specific fingermark. Furthermore, traditional techniques are sometimes not ideal and may even be inapplicable. This is particularly true for fingermarks on common but difficult substrates such as adhesive tapes, woods, and plastics; partial bloody fingermarks, and discharged cartrige casings.

A new type of fingermark development technique which relies on the topology of the fingermark to produce contrast with the substrate was recently developed [46, 54]. This technique deposits a columnar thin film (CTF) conformally over both the fingermark and the underlying substrate. The CTF is produced using the conformal-evaporated-film-by-rotation (CEFR) method, which was originally developed to replicate the surface features of biological templates such as butterfly wings and fly eyes [34,35]. CEFR is a variation on thermal evaporation.

As in thermal evaporation, an electric current is passed through a metal receptacle which contains a source material. The receptacle is heated by passing a large current through it until the source material begins to transition to the vapor phase. Both the source and the substrate are contained within a vacuum chamber which allows the generated vapor flux to ballistically travel from the source to the substrate. This line-of-sight path of the vapor flux can lead to shadowed regions of the substrate receiving very little or no incident vapor and demonstrating no film growth as a result. The CEFR method is shown schematically in Fig. 2.2. This shadowing can be utilized to produce a CTF. When the angle χ_v between impinging vapor flux and substrate's surface is sufficiently small the initial nucleation sights will shadow each other. This self-shadowing leads to competitive growth amongst the nucleation sights wherein the tallest sights receive the greatest amount of vapor and grow faster as a result. Because each site receives vapor flux on their upper surfaces, a columnar morphology results, where each column is tilted approximately toward the vapor source [31]. If the substrate is rapidly rotated about its surface normal during this process

the columns will grow normal to the substrate surface as can be seen in Fig. 3.1 [34–36].

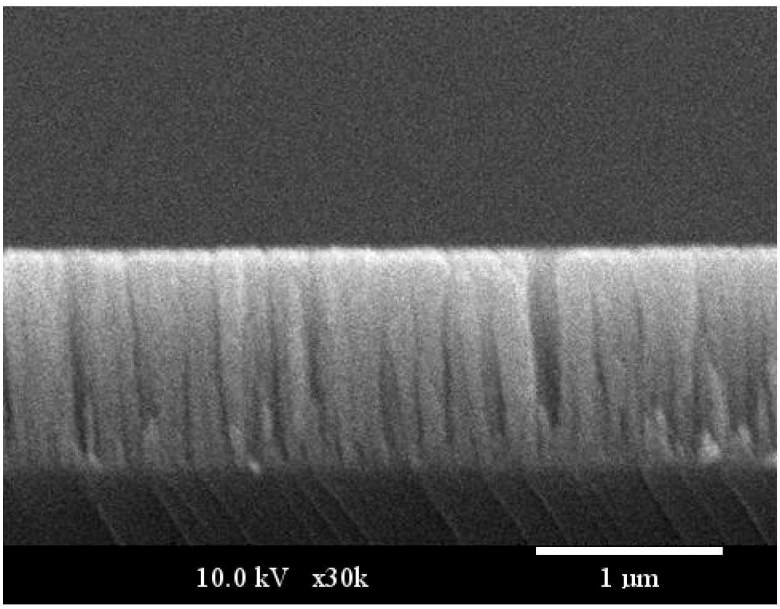

Figure 3.1: Cross-sectional SEM image of a CTF of chalcogenide glass grown on a planar glass substrate using the CEFR method with constant rotation at 120 rpm while $\chi_v = 10°$. The columns of the CTF grew upright.

The rapid rotation of the substrate leads to the resulting CTF conformally coating both the substrate and the fingermark. The topology of the fingermark is reproduced by a mechanism similar to a child's pinpoint impression toy [46]. When the toy is placed on an undulating surface, the surface is reproduced at the surface consisting of the heads of the parallel pins. As the diameter of the pins is decreased the fidelity of the replication is increased. As the column diameter of a CTF can be 30-to-100-nm, the topology of a fingermark can be reproduced at the nanoscale.

Here I present in detail a systematic study carried out in order to optimize the deposition parameters affecting the CTF development of fingermarks. Once optimal values of deposition parameters had been determined to develop fingermarks with the highest quality, clarity, and contrast, several forensically relevant non-porous substrates upon which fingermarks are commonly found at a crime scene were developed with various evaporant materials. Fingermarks found on non-porous substrates upon which fingermarks are commonly found at a crime scene were developed with various evaporant materials. Fingermarks found on non-porous substrates

are typically very fragile as they do no adsorb onto the substrate but merely lie atop the substrate [31]. Fingermarks on these types of substrates are normally developed using cyanoacrylate fuming, powders, dyes, and VMD, and are also candidates for CTF development. Optimal combinations of forensically relevant substrates and evaporant materials were found, along with the identification of those substrates for which CTF development was found to be superior to the results from traditional development techniques. A hybrid technique comprising two steps — conventional fuming in a cyanoacrylate chamber followed by the deposition of a CTF— also emerged as a successful technique in some instances.

The plan for this chapter is as follows: In Secs. 3.3 and 3.4, the process and results of the optimization of the CTF technique are described. The investigation of the development of partial bloody fingermarks is covered in Sec. 3.5. A comparison of the sensitivity of the CTF technique and traditional fingermark development techniques is made in Sec. 3.6. In Sec. 3.7 the CTF and vacuum-metal deposition are compared. Finally, concluding remarks are made in Sec. 3.8.

3.3 Materials and Methods

3.3.1 Fingermark Collection

All fingermarks were collected using a specific grooming procedure to ensure as much consistency as possible — first, throughout the optimization of the deposition parameters for CTF development, and then during comparative studies against traditional development techniques. The grooming procedure used the same finger of the same person at all times to limit variability. The finger was first cleansed with ethanol and allowed to dry. The fingertip was then swiped across the forehead, nose, and chin of the donor 20 times. Two fingermarks were laid down on a glass slide to remove excess sebaceous secretions, and then two fingermarks were laid down on the substrate of interest for processing. This procedure was then repeated until the desired number of samples was reached. In this study, the services of one fingermark donor, unless otherwise noted, were utilized to minimize variability and maximize consistency between experiments. For each experiment, four duplicate fingermarks were collected. Fingermarks were allowed to age 24 hrs prior to development.

3.3.2 Grading System

All fingermarks were graded based on visual observation and comparison. Clarity, contrast, and visualization of observable detail of level one/two/three were all considered as developed fingermarks were compared side by side [64–69].

3.3.3 Optimization of CTF Developemt

Prior to comparing the CTF development technique to the traditional development techniques, a systematic series of experiments was carried out in order to determine the optimal CTF-deposition conditions necessary to achieve the highest quality of fingermark development. The following parameters were varied within the limitations of a custom-made CEFR apparatus [46, 54] in order to find their optimal values: (i) base pressure in the vacuum chamber prior to deposition, (ii) angle χ_v of the collimated vapor flux relative to the stage plane, (iii) stage rotation rate, (iv) deposition rate of the CTF, and (v) thickness (as measured by a quartz crystal monitor within the vacuum chamber) of the CTF. The base pressure was controlled using a turbo pump, the stage rotation rate by the rotation motor, the deposition rate of the CTF through the electric current passed through a tungsten boat holding the evaporant material, and the CTF thickness by a quartz crystal monitor (QCM) located close to the substrate inside the vacuum chamber. The QCM also provides feedback for deposition control. The rocking motor was not used and the angle χ_v was held fixed during deposition. The evaporant material used for the optimization study was chalcogenide glass of nominal composition $Ge_{28}Sb_{12}Se_{60}$ and the underlying substrates were standard glass microscope slides.

3.3.4 Forensically Relevant Substrates

The chosen substrates included: (i) brass (Alloy 260), (ii) stainless steel (Grade 420), (iii) the sticky and smooth sides of various adhesive tapes (Scotch Duct®, Gloss Finish Scotch Multitask®, Scotch Masking®, and Gorilla®), (iv) hard plastics (black and white nylon, black and white acrylonitrile butadiene styrene (ABS)),(v) soft plastics (clear sandwich bags, white grocery bags, black garbage bags), (vi) woods (stained, and stained and sealed with polyurethane), (vii) anodized aluminum (Alloy 5005), and (viii) discharged cartridge casing (9 mm Luger). All substrates–except discharged cartridge casings–were cut into 25 mm $\times$ 25 mm squares for

deposition of a fingermark per square.

3.3.5 Evaporant Materials

The evaporant materials utilized were selected because of their compatibility with thermal evaporation [70]. Easily evaporated materials are desirable because they allow for high deposition rates to be achieved without producing unnecessary heat that could damage both the substrate under investigation and the fingermark thereon. The evaporant materials chosen were: (i) chalcogenide glass of nominal composition $Ge_{28}Sb_{12}Se_{60}$, (ii) gold, (iii) nickel, (iv) magnesium fluoride, (v) germanium oxide, and (vi) Tris(8-hydroxyquinolinato) aluminum, more commonly known as Alq_3.

Alq_3 is an organometallic chelate that is typically used in organic light-emitting diodes, where variations of the quinoline structure can affect its luminescent properties [71]. Deposition of Alq_3 produces a developed fingermark that is visible when exposed to short-wave ultraviolet radiation. Germanium oxide is a high-refractive-index material often used to make wide-angle lenses, magnesium fluoride is a low-refractive index material often used for anti-reflective coatings, gold and nickel are commonly used metals, and chalcogenide glass is an infrared transparent material often used for infrared applications. This diversity of materials was chosen in order to best optimize deposition parameters on various substrates for the best contrast possible.

3.3.6 Selected Traditional Development Techniques

The CTF development technique was compared to traditional development techniques by following a split-fingermark protocol. A fingermark was deposited onto two 25 mm×12.5 mm pieces of the selected substrate that were laid side by side, so that half of each fingermark was placed on each piece. Each half was subsequently developed with either the CTF development technique or a traditional technique relevant to the specific substrate. Traditional development techniques utilized included: (i) dusting with regular black powder, regular white powder, magnetic black powder, magnetic white powder, or a fluorescent powder (red, green, yellow, orange, gold) and (ii) cyanoacrylate fuming (with cyanoblue dye when applicable) in a commercial chamber (Arrowhead Forensics, Lenexa, KS). The third traditional technique involved the use of either a pre-mixed liquid sold as Wetwop®, sticky-side powder (SSP), a small-particle reagent (SPR), leucocrystal

violet (LCV), or a protein dye called amido black, as appropriate for the substrate of interest. Following separate development of both halves of each fingermark, the two halves were reconnected and photographed for grading using the aforementioned grading scheme. Table 3.1 shows all forensically relevant substrates investigated along with all traditional development techniques employed for each chosen substrate.

The performance of the CTF development technique is compared with that of VMD [60] in Sec. 3.7. Both techniques are similar in that they are based on evaporating a material in a vacuum chamber. In the usual implementation of VMD, first gold is evaporated to form a thin layer that penetrates the fingermark residue, and then a second layer of zinc or cadmium is similarly deposited. However as the second layer does not penetrate the fingermark residue but lies atop the gold layer wherever it can, the fingermark ridges appear transparent on a dark zinc/cadmium background [72]. In contrast, the CTF is a conformal coating on the fingermark ridges (see Fig. 3.2e).

3.3.7 Imaging of Fingermarks

Both undeveloped and developed fingermarks were photographed with a Nikon D3000 10.2 megapixel camera with a Nikon 60 mm macro lens capable of 1:1 reproduction. The camera was attached to a custom stand that allowed photographs to be take from the same viewing angle and under the same lighting conditions. High-magnification ($10\times$ to $40\times$) optical images of the fingermarks were acquired on a National stereo microscope partnered with a Moticam 1000 1.3 megapixel microscope camera.

A Hitachi S-3500N backscattered scanning electron microscope (SEM), capable of resolving 4 nm at 25 kV and with magnification ranging from $15\times$ to $100K\times$, was used to make images on which the columnar morphology of CTFs deposited on fingermarks could be resolved.

3.4 Results and Discussion

In a comprehensive study for the optimization of CTF development with chalcogenide glass as the evaporant material and a glass slide as the substrate, the following five parameters were varied: base pressure, the fixed vapor flux angle χ_v, CTF deposition rate, stage rotation rate, and CTF thickness. The values of these parameters specifically used for optimization are presented in

Table 3.1: Combinations of forensically relevant substrates and traditional development techniques (excluding VMD) investigated

Forensically Relevant Substrate	Specifically	Traditional Development Techniques
Brass[1]	Alloy 260	Regular powder, Magnetic powder, Fluorescent powders, Cyanoacrylate fuming
Stainless Steel[1]	420 Grade	Regular powder, Magnetic powder, Fluorescent powders, Cyanoacrylate fuming
Anodized Aluminum[1]	Alloy 5005	Regular powder, Magnetic powder, Fluorescent powders, Cyanoacrylate fuming
Adhesive Tapes (sticky and smooth sides)[2]	Scotch Duct®, Gloss Finish Scotch Multitask®, Masking, Gorilla®	Wetwop®, SSP, SPR, Cyanoacrylate fuming, Cyanoblue, Powders
Hard Plastics[1]	Nylon, ABS	Regular powder, Magnetic powder, Fluorescent powder,s Cyanoacrylate fuming
Soft Plastics[3]	Black garbage bag, White grocery bag, Clear Sandwich bag	Regular powder, Magnetic powder, Fluorescent powders, Cyanoacrylate fuming
Stained and Sealed Woods[4]	Pine, Walnut	Regular powder, Magnetic powder, Fluorescent powders, Cyanoacrylate fuming
Discharged Cartridge Casings[5]	9 mm Luger	NA

[1] Purchased from McMaster–Carr Supply Co., Inc.
[2] Purchased from Staples, Inc.
[3] Purchased from Weis Markets, Inc.
[4] Wood donated by Spectra Wood, Inc. and stains/seals purchased from Lowe's Companies, Inc.
[5] Purchased from Walmart, Inc. and discharged at the Pennsylvania Game Commission's Scotia range.

Table 3.2: Deposition parameters influencing CTF development and their optimal values, the evaporant material being chalcogenide glass and the substrates being microscope glass slides. Note that the rocking motor was not used so that the direction of the vapor flux was held fixed during every deposition.

Parameter	Values Investigated for Optimization	Optimal Value
Base Pressure ($\times 10^{-4}$ Torr)	0.028, 0.13, 1.0, 400	1
Average Vapor Flux Angle χ_v (deg)	5, 10, 15, 20, 30, 60, 90	20
CTF Deposition Rate (nm s^{-1})	0.5, 1.0, 2.0, 5.0	1
Stage Rotation Rate (rpm)	4.5, 15, 60, 180	180
CTF Thickness (nm)	200, 500, 800, 1000, 1500, 2000	1000

Table 3.2, along with the optimal value of each parameter determined by visual observation of clarity, contrast, and level one/two/three detail of the developed fingermarks.

The optimal values of four of the five parameters turned out to be quite similar to those used in the initial proof-of-principle experiments [46, 54], the sole exception being the base pressure prior to the beginning of the CTF deposition. Whereas the base pressure was 4.0×10^{-6} Torr or lower in the predecessor studies [46, 54], it was determined that just 1.0×10^{-4} Torr would suffice for fingermark development. The adequate base pressure thus determined is moderately low, which greatly reduces the requirements on CEFR apparatus for fingermark development. This finding also allows for increased fieldability of the CTF development technique for on-scene development of fingermarks, because the vacuum pump needed is going to be much smaller and less expensive than originally thought. Furthermore, the time needed to pump down to the base pressure is reduced. The smaller size and lower price would allow for crime laboratories of even small or medium size to budget for and operate the CEFR apparatus comfortably.

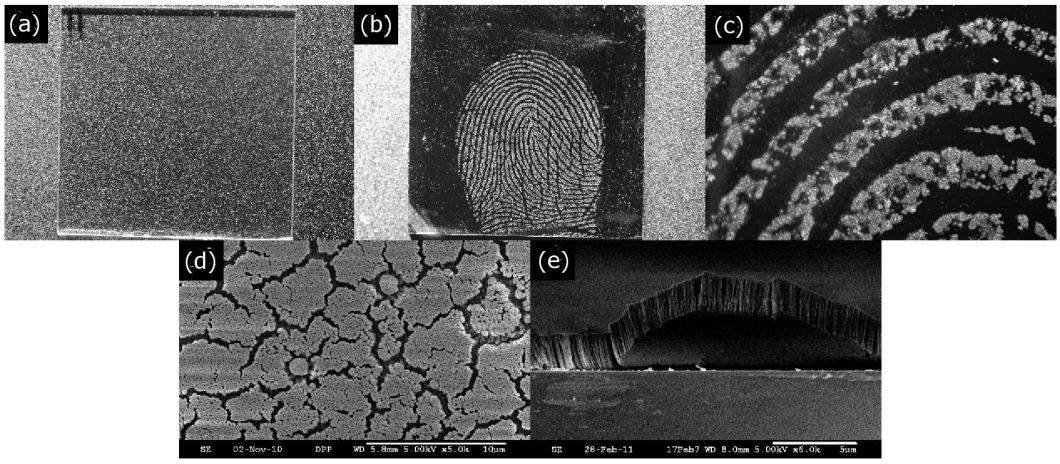

Figure 3.2: (a) Photograph of a fingermark on a glass slide before CTF development; (b) photograph of the developed fingermark after a 1000-nm-thick CTF of chalcogenide glass had been deposited thereon under the optimal conditions identified in Table 3.2; (c) a 30× magnified image on an optical microscope of the developed fingermark, showing level-three pore detail very clearly; (d) top-view SEM image of the developed fingermark at 5000× magnification; and (e) cross-sectional SEM image of a ridge in the developed fingermark at 6000× magnification.

The efficacy of the CTF development technique is brought out by the five images presented in Fig. 3.2. Photographs of a fingermark on a glass slide are shown in Figs. 3.2(a) and 3.2(b), respectively, before and after development using the optimal conditions identified in Table 3.2. The fingermark is invisible (Fig. 3.2(a)) but the optimal deposition of a chalcogenide-glass CTF on it makes it clearly visible (Fig. 3.2(b)). The 30× magnified image in Fig. 3.2(c), obtained on an optical microscope that should be easily affordable to a crime laboratory, shows level-three pore detail. The top-view SEM image at 5000× magnification in Fig. 3.1(e) shows not only a generally upward columnar morphology but also the conformal shape of the deposited CTF.

The optimal deposition parameters presented in Table 3.2 were obtained for just one combination of the evaporant material (chalcogenide glass) and the substrate (glass slide). Except for the CTF thickness, all other optimal parameters in Table 3.2 were found to also deliver the best fingermark development for all other combinations of the evaporant material and substrate. However, the optimal CTF thickness did depend on the evaporant material. For instance, 50-nm-thick CTFs of gold provided optimal contrast, whereas the optimal thickness of a CTF of chalcogenide glass turned out to be 20 times higher. For all other combinations of the evaproant material and substrate tested, the optimal CTF thickness was fount to lie between 50 and 1000

nm, both inclusive.

Meta-analysis of the data collected resulted in the identification of the best evaporant material for the CTF development technique as well as the best traditional development technique for a wide range of non-porous substrates upon which fingermarks are commonly found at crime scenes [73]. The best evaporant material and the optimal CTF thickness–along with the best traditional technique for all substrates investigated are available in Table 3.3.

For several of the substrates investigated, the CTF development technique provided results superior to those of all traditional development techniques investigated. For some others, the CTF-developed fingermark and the best traditionally developed fingermarks were of the same quality. Both groups of substrates are listed in Table 3.4, as are the substrates for which the best traditional development technique outperformed the CTF development technique.

Table 3.3: The best evaporant material for the CTF development technique, the optimal CTF thickness, and the best traditional technique (excluding VMD) for all substrates investigated. The asterisk indicates that the substrate was subjected to cyanoacrylate fuming before being subjected to the CEFR method, in order to obtain the best CTF development.

Substrate	Best Evaporant Material	CTF Thickness (nm)	Best Traditional Development Technique
Brass	Chalcogenide Glass	1000	Black powder or cyanoacrylate
Stainless Steel	Chalcogenide Glass	1000	Cyanoacrylate and cyanoblue
Stainless Steel	Nickel	100	Cyanoacrylate and cyanoblue
Anodized Aluminum	Alq_3	100	Black magnetic powder
Stained and sealed walnut	Alq_3	100	White magnetic powder
Stained and Sealed Cherry	Alq_3	100	Black magnetic powder
ABS-black	Alq_3	100	Red fluorescent powder

Continued on next page

Table 3.3 – continued from previous page

Substrate	Best Evaporant Material	CTF Thickness (nm)	Best Traditional Development Technique
ABS-white	Alq_3	100	Black magnetic powder
Nylon-black	Alq_3	100	Red fluorescent powder
Nylon-white	Alq_3	100	Black magnetic powder
Soft Plastic-black (Garbage bag)	Nickel	100	White magnetic powder
Soft Plastic-white (Grocery bag)	Nickel	100	Black magnetic powder
Soft Plastic-clear (Sandwich bag)	Gold	50	Cyanoacrylate
Scotch Duct® Tape-sticky side	Nickel	100	Wetwop®
Scotch Duct® Tape-sticky side	Gold	50	Wetwop®
Scotch Duct® Tape-smooth side∗	Gold	50	Cyanoacrylate and cyanoblue
Masking Tape-sticky side	Nickel	100	Cyanoacrylate and cyanoblue
Masking Tape-sticky side	Gold	50	Cyanoacrylate and cyanoblue
Masking Tape-smooth side	N/A	N/A	N/A
Gorilla® Tape-sticky side∗	Gold	50	Wetwop®
Gorilla® Tape-smooth side	Gold	50	Cyanoacrylate
Scotch Tape-sticky side	Gold	50	Wetwop®
Scotch Tape-smooth side	Gold	50	Cyanoacrylate

Continued on next page

Table 3.3 – continued from previous page

Substrate	Best Evaporant Material	CTF Thickness (nm)	Best Traditional Development Technique
Discharged Cartridge Casings∗	Alq_3	100	N/A

Thus, the CTF development technique is not universally applicable, as can be expected from any technique to develop fingermarks. Development by the deposition of a CTF is suitable typically only for non-porous substrates, and the fragility of some substrates poses development difficulties. Fingermarks on some of the substrates investigated were difficult to develop as the temperature within the vacuum chamber can sometimes reach 40 $°C$. Some substrates–such as soft black plastic sheets (black garbage bags)–curled up upon development. In the case of Scotch Duct® tape, the cords within the adhesive started pulling out of the surface of the tape. The deformation of some substrates (such as soft plastics and adhesive tapes) inside the vacuum chamber limited the types of evaporant materials that could be used for the CTF development of fingermarks. In many cases, however, this deformation could be minimized by carefully shuttering the source of the thermal energy and minimizing the time that the substrate was unnecessarily exposed.

Some substrates in Table 3.3 are marked with an asterisk. Whereas the CTF development technique did not produce satisfactory results with these substrates, pretreating the fingermark on these substrates with cyanoacrylate fuming followed by the application of the CTF development technique produced the best outcomes. Thus, fingermarks on the smooth sides of Scotch Duct® tape (Fig. 3.3) and Gorilla® tape (Fig. 3.4) developed very well on cyanoacrylate fuming followed by the deposition of a 50-nm-thick CTF of gold. Quite possibly, successful development was facilitated by the layer of cyanoacrylate providing better definition to the fingermark topology, which was then revealed by the CTF deposited on top of the enhanced topology. The hybrid cyanoacrylate-CTF technique appears promising and requires further research.

All adhesive tapes were able to withstand the higher than room temperature in the vacuum chamber very well. CTF development with gold as the evaporant material worked very well–and better than any traditional development–with fingermarks laid on the smooth sides of three of

Table 3.4: Comparison of the performance of the CTF development technique and the best traditional development technique (excluding VMD). The asterisk indicates that the substrate was subjected to cyanoacrylate fuming before being subjected to the CEFR method, in order to obtain the best CTF development.

Substrate	CTF Development is Superior	Best Traditional Development is Superior	Equal Quality
Brass	–	–	Yes
Stainless Steel	–	Yes	–
Anodized Aluminum	Yes	–	–
Stained and sealed walnut	Yes	–	–
Stained and Sealed Cherry	Yes	–	–
ABS-black	–	–	Yes
ABS-white	–	Yes	–
Nylon-black	–	Yes	–
Nylon-white	–	–	Yes
Soft Plastic-black (Garbage bag)	Yes	–	–
Soft Plastic-white (Grocery bag)	–	–	Yes
Soft Plastic-clear (Sandwich bag)	Yes	–	–
Scotch Duct® Tape-sticky side	–	–	Yes
Scotch Duct® Tape-smooth side∗	Yes∗	–	–
Masking Tape-sticky side	–	Yes	–
Masking Tape-smooth side	N/A	N/A	N/A
Gorilla® Tape-sticky side	–	–	Yes
Gorilla® Tape-smooth side∗	Yes∗	–	–
Scotch Tape-sticky side	–	–	Yes
Scotch Tape-smooth side	Yes	–	–
Discharged Cartridge Casings∗	Yes	N/A	–

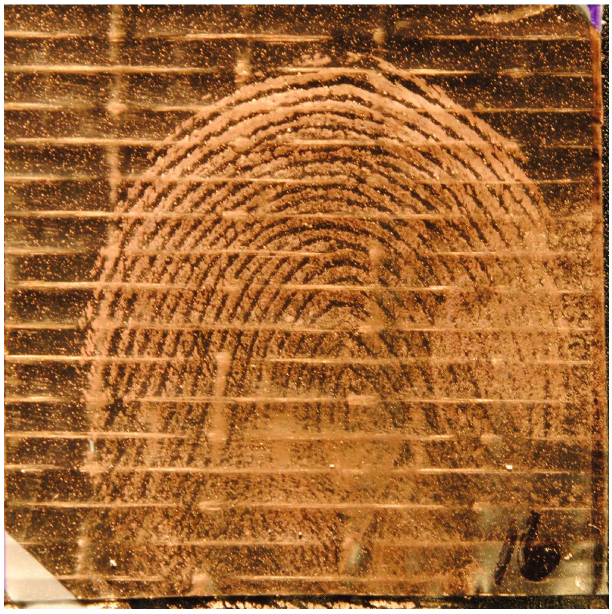

Figure 3.3: Fingermark on the smooth side of Scotch Duct® tape developed by a hybrid technique involving pretreatment of the fingermark by cyanoacrylate fuming followed by the deposition of a 50-nm-thick CTF of gold. [Courtesy of Sarah Muhlberger]

Figure 3.4: Same as Fig. 3.3, but for the smooth side of Gorilla® tape. [Courtesy of Sarah Muhlberger]

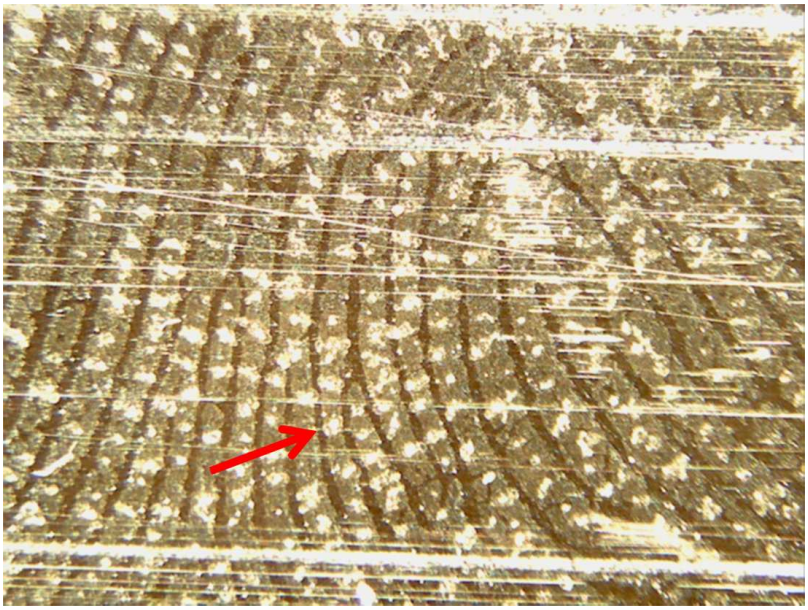

Figure 3.5: Fingermark on the smooth side of Gloss Finish Scotch Multitask tape developed by the deposition of a 50-nm-thick CTF of gold. Level-three detail is clearly observable in the developed fingermark. [Courtesy of Sarah Muhlberger]

the four adhesive tapes investigated. As an example, level-three detail is clearly observable in Fig. 3.5, showing a fingermark on the smooth side of Gloss Finish Scotch Multitask® tape which was developed with a 50-nm-thick CTF of gold. Other substrates, such as the smooth sides of Scotch Duct® tape (Fig. 3.3) and Gorilla® tape (Fig. 3.4), did require application of the hybrid cyanoacrylate-CTF development technique. The sole exception was the smooth side of Scotch Masking® tape, for which no development technique delivered a satisfactory outcome.

The CTF development technique also performed well on fingermarks on the sticky sides of Scotch Duct® tape, Gorilla® tape, and Gloss Finish Scotch Multitask® tape. However equally satisfactory performance was delivered by the traditional development technique of the application of Wetwop®, as exemplified in Figs. 3.6–3.8. Figure 3.9 shows that the cyanoacrylate fuming (with cyanoblue dye) yielded a superior result on the sticky side of Scotch Masking® tape than the CTF development technique.

The CTF development technique worked very well with fingermarks deposited on all three types of soft plastics: black garbage bags, white grocery bags, and clear sandwich bags. For black garbage bags (Fig. 3.10) and clear sandwich bags (Fig. 3.11), the CTF development technique

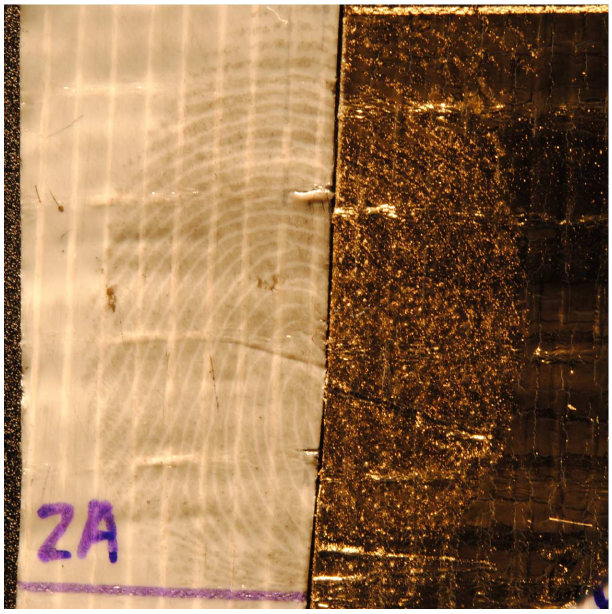

Figure 3.6: Fingermark on the sticky side of Scotch Duct® tape developed either (left) by the use of Wetwop® or (right) by the deposition of a 100-nm-thick CTF of nickel. [Courtesy of Sarah Muhlberger]

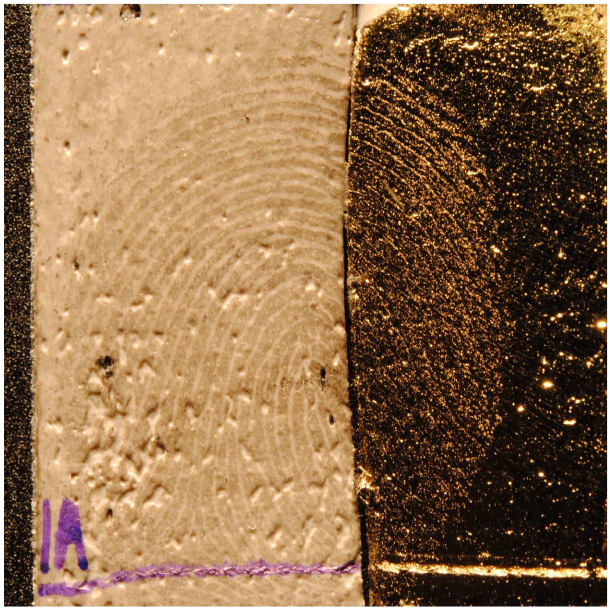

Figure 3.7: Fingermark on the sticky side of Gorilla® tape developed either (left) by the use of Wetwop® or (right) by the deposition of a 50-nm-thick CTF of gold. [Courtesy of Sarah Muhlberger]

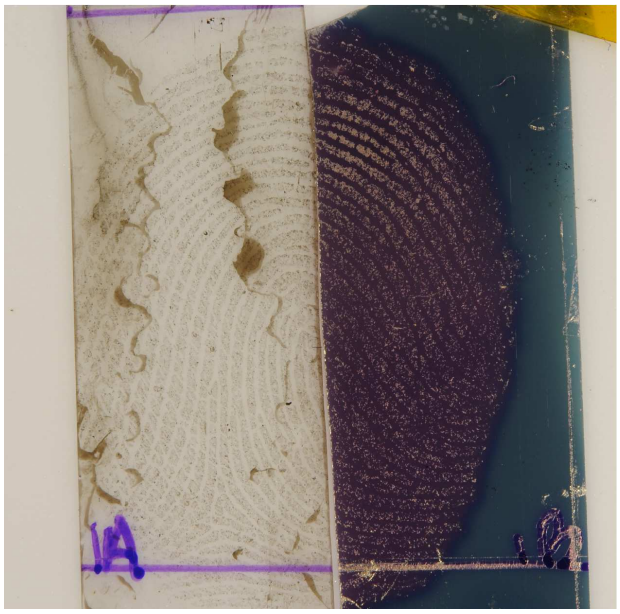

Figure 3.8: Same as Fig. 3.7, except for the sticky side of gloss finish Scotch Multitask® tape. [Courtesy of Sarah Muhlberger]

Figure 3.9: Fingermark on the sticky side of Scotch Masking® tape developed either (left) by the use of Wetwop® or (right) by the deposition of a 100-nm-thick CTF of nickel. [Courtesy of Sarah Muhlberger]

provided much better contrast for visualization than any traditional development techniques. Even on white grocery bags (Fig. 3.11), the CTF development technique performed as well as dusting with black magnetic powder, the best traditional development technique for the specific substrate.

Figure 3.10: Fingermark on a black garbage bag (soft plastic) developed either (left) by the use of white magnetic power or (right) by the deposition of a 100-nm-thick CTF of nickel. Level three detail is clearly seen in the CTF-developed fingermark. [Courtesy of Sarah Muhlberger]

The CTF development technique did not show superior performance for fingermarks on hard plastics. The best results were obtained with 100-nm-thick CTFs of Alq_3. As may be gathered from Figs. 3.13–3.16, the CTF development technique performed as well as dusting with red fluorescent powder for fingermarks on black ABS (Fig. 3.13) and white nylon (Fig. 3.16). On white ABS (Fig. 3.14) and black nylon (Fig. 3.15), respectively, the CTF development technique was outperformed by dusting with black magnetic powder and red fluorescent powder.

Wood substrates are typically porous in nature, except when sealed with a polyurethane or equivalent coating. Fingermarks were deposited on smooth surfaces of commercial samples of cherry and walnut woods that had been stained and sealed. None of the selected evaporant materials worked well, with the exception of Alq_3. When exposed to short-wave ultraviolet radiation, the Alq_3-developed fingermarks possessed suitable contrast for identification of fingermark ridge

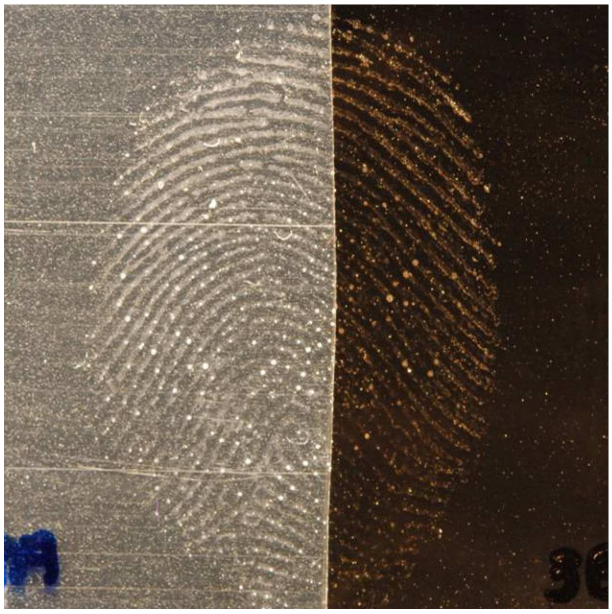

Figure 3.11: Fingermark on a clear sandwich bag (soft plastic) developed either (left) by the use of cyanoacrylate fuming or (right) by the deposition of a 50-nm-thick CTF of gold. Level three detail is clearly seen in the CTF-developed fingermark. [Courtesy of Sarah Muhlberger]

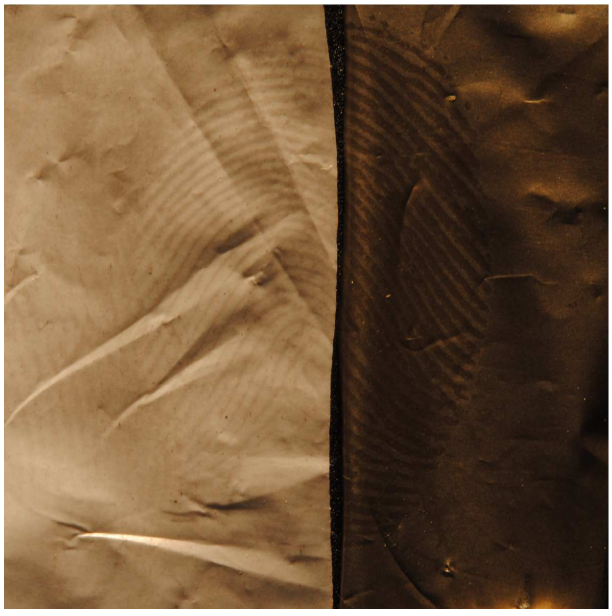

Figure 3.12: Fingermark on a white grocery bag (soft plastic) developed either (left) by the use of black magnetic power or (right) by the deposition of a 100-nm-thick CTF of nickel. [Courtesy of Sarah Muhlberger]

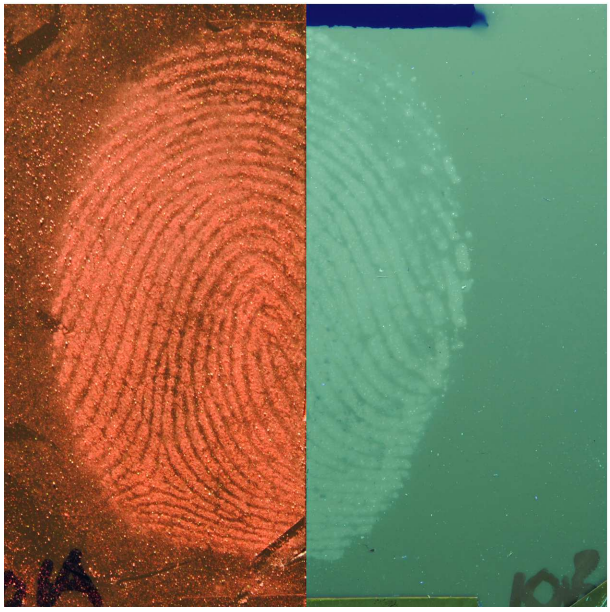

Figure 3.13: Fingermark on black ABS developed either (left) by the use of red fluorescent powder or (right) by the deposition of a 100-nm-thick CTF of Alq_3. Short-wave ultraviolet illumination is needed to see the detail in the CTF-developed part of the fingermark. [Courtesy of Sarah Muhlberger]

detail. None of the chosen traditional methods performed satisfactorily.

Discharged cartridge casings have no traditionally accepted method for development of fingermarks on them, and many of the previously discussed methods have been applied in order to find a method with acceptable performance [74]. In this study, fingermarks placed on cartridge casings before the discharge of a 9 mm firearm were developed by the hybrid cyanoacrylate-CTF technique used also for developing fingermarks on adhesive tapes. A special fixture for mounting the discharged cartridge casing to the stage in the vacuum chamber had to be devised and fabricated. Furthermore, as the substrate (cartridge casing) is not flat but possesses a convex cross section at the macroscopic length scale, the rocking motor was used to continually change the angle χ_v between 10 and 90 deg with a temporal period of ~ 9 s during deposition [33]. Also for this case, the fingermark donor was different from the one for all other cases reported in this paper. Alq_3 was evaporated to deposit 100-nm-thick CTF. As can be observed in Fig. 3.19, under short-wave ultraviolet illumination, the developed fingermark has sufficient detail for identification.

The foregoing examples have shown that the CTF development technique is superior to traditional development techniques in some instances. In other instances, a traditional development

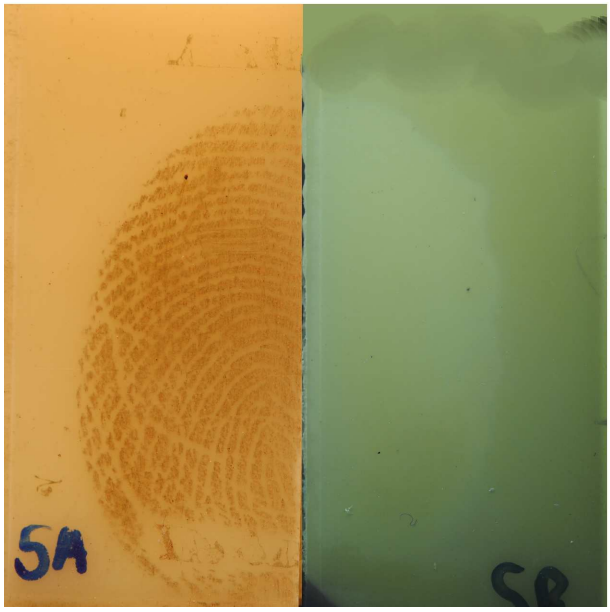

Figure 3.14: Fingermark on white ABS developed either (left) by the use of black magnetic powder or (right) by the deposition of a 100-nm-thick CTF of Alq_3. Short-wave ultraviolet illumination is needed to see the detail in the CTF-developed part of the fingermark. [Courtesy of Sarah Muhlberger]

technique produces better outcomes than the CTF development technique. But there are also substrates for which the CTF development technique and the best traditional development technique deliver equally good results: contrast as well as the visibility of identifiable details, including level-three details, are equivalent between the two techniques. These substrates are significant for ongoing research on the sensitivity of the CTF development technique compared to that of traditional development techniques through depletion studies. It is possible that future research will show that the CTF development of fingermarks is superior to traditional development of fingermarks that are aged, degraded, or exposed to environmentally insulting conditions. Such outcomes may emerge, particularly when only a small amount of fingermark residue is present, because CTF development relies on the topology of the fingermark rather than on some physical or chemical reaction with the fingermark residue.

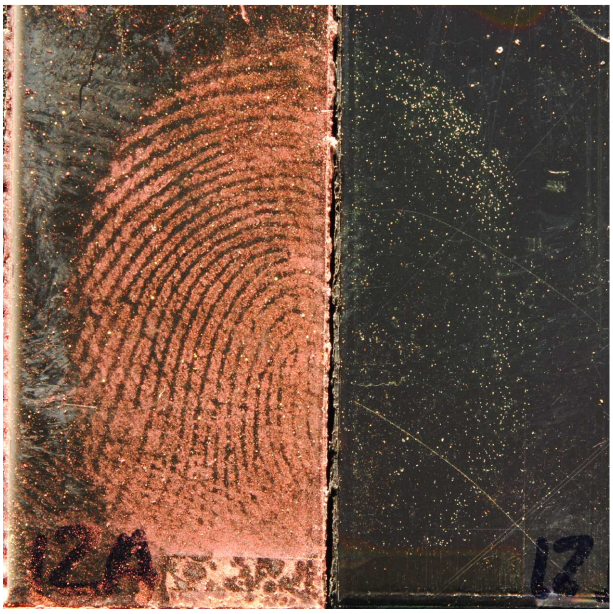

Figure 3.15: Fingermark on black nylon developed either (left) by the use of red fluorescent powder or (right) by the deposition of a 100-nm-thick CTF of Alq_3. Short-wave ultraviolet illumination is needed to see the detail in the CTF-developed part of the fingermark. [Courtesy of Sarah Muhlberger]

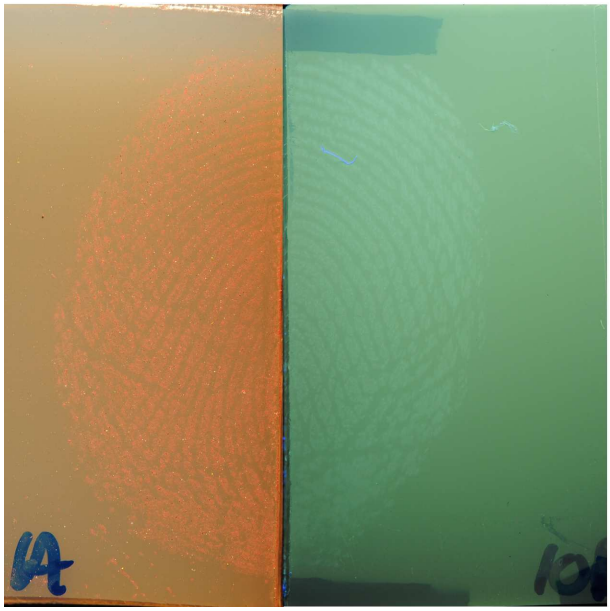

Figure 3.16: Same as Fig. 3.15 except that the substrate is white nylon. [Courtesy of Sarah Muhlberger]

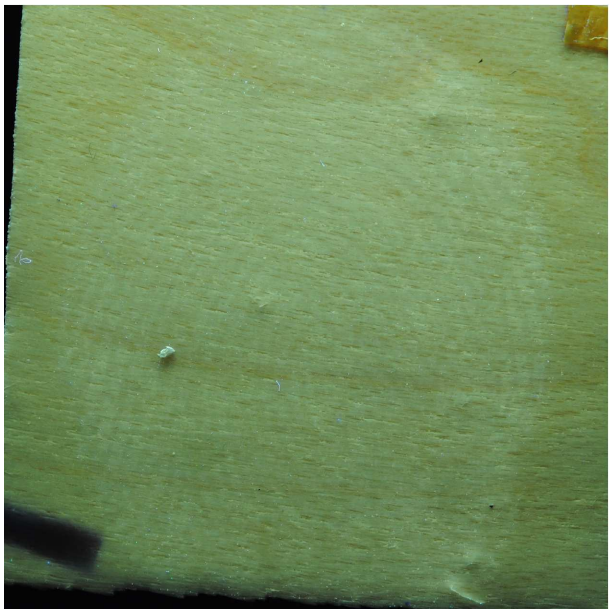

Figure 3.17: Fingermark on stained and sealed cherry wood, developed by the deposition of a 100-nm-thick CTF of Alq_3, fluoresces under illumination by a short-wave ultraviolet source. [Courtesy of Sarah Muhlberger]

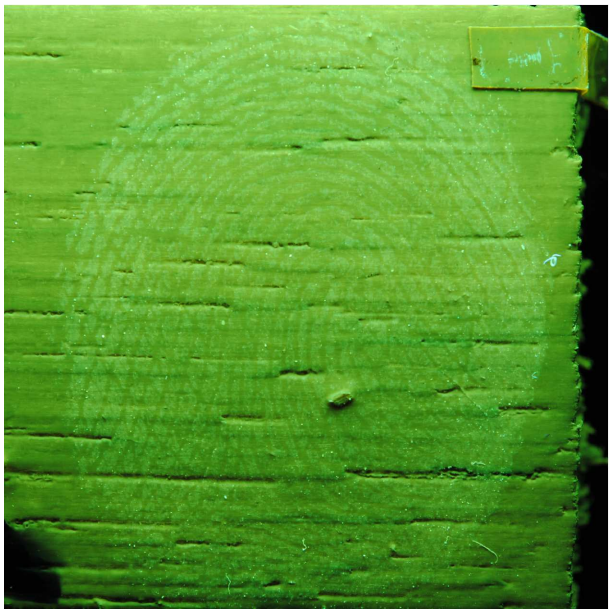

Figure 3.18: Same as Fig. 3.17 except that the substrate is stained and sealed walnut wood. [Courtesy of Sarah Muhlberger]

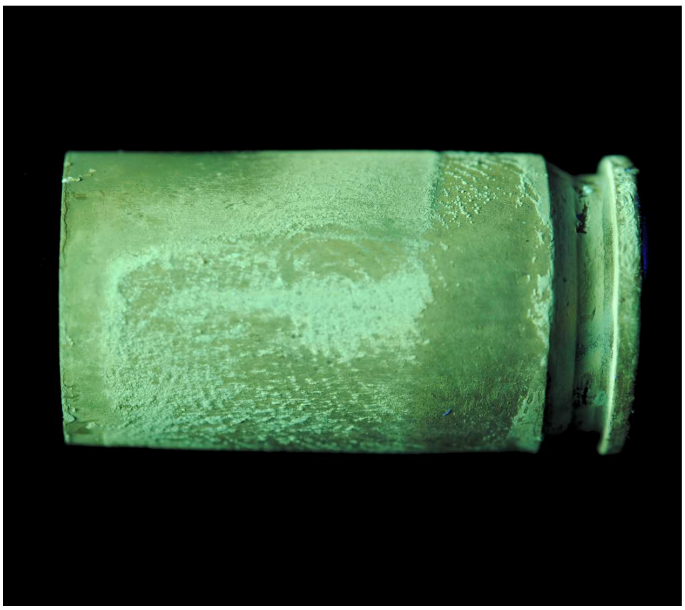

Figure 3.19: Fingermark on a cartridge casing developed after discharge by a hybrid technique involving pretreatment of the fingermark by cyanoacrylate fuming followed by the deposition of a 100-nm-thick CTF of Alq_3. Short-wave ultraviolet illumination is needed to see the detail.

3.4.1 Comparison of CEFR with Slanted-CTFs and Normal Deposition for the Development of Fingermarks

When introducing a development technique that utilizes more complicated apparatus or processing, the question of what is being gained from this added complexity naturally arises. To address this, I conducted a series of experiments which compare the CEFR development described earlier in Sec. 3.2 with the more simplified deposition of slanted-CTFs and the normal deposition of a dense thin film. As described in Sec. 1.3, the combination of a tilted and rapidly rotating substrate produces film morphology characterized by columns oriented normal to the substrate surface. If the substrate is tilted but not rotated during the deposition, the film morphology will be characterized by columns which grow roughly in the direction from which the incident vapor flux was arriving. In the case where the substrate is held normal to the direction from which the incident vapor flux is arriving, a relatively dense thin film is deposited.

In order to compare these three deposition methods, a split-fingermark protocol was implemented to allow for the side-by-side comparison between the CEFR development and the slanted-CTF development without substrate rotation, and the normal thin film development

without substrate tilting or rotation, respectively.

Details of the fingermark grading scheme using a clarity map used here can be found in Appendix A. A clarity map visually identifies the regions of different clarity ratings of a photographed fingermark. Regions which contain definitive minutiae are given the highest clarity rating and assigned the color green, regions containing debatable minutiae are given the second highest clarity rating and assigned the color yellow, regions containing debatable ridge flow are given the second lowest rating and assigned the color yellow, and finally regions identified as background are given the lowest clarity rating and assigned the color black. From this clarity map, the fraction of a fingermark area classified as being of the highest clarity can be calculated and used to quantitatively compare the results of two development techniques.

In this way, it was found that the half of the fingermark developed by CEFR demonstrated greater clarity when compared to either of the other two development techniques. In Fig. 3.20 a clarity map is shown overlaying a photograph of a split fingermark of which the left side was developed by CEFR while the right side was developed with a slanted-CTF (without substrate rotation). From this clarity map it is apparent that CEFR development performs substantially better than development with a slanted-CTF. This experiment was repeated 3 times and resulted in a mean area identified as having the highest clarity of 25% for the CEFR developed half of the fingermark and 2.3% for the slanted-CTF developed half.

Figure 3.21 shows another clarity map, this time with CEFR developed on the left half and a normally developed half on the right. In this case, the mean area identified as having the highest clarity over 3 experiments is 22% for the CEFR developed half and 6.3% for the normally developed (without substrate tilt or rotation) half. This result justifies the use of the slightly more complicated to produce vertical-CTFs over both slanted-CTFs and normally deposited film for the development of fingermarks.

3.5 Partial Bloody Fingermarks

A partial bloody fingermark has both a bloody part and a non-bloody part. A combination of two development techniques has to be used to develop partial bloody fingermarks. The bloody part is often developed by causing a protein stain to react with proteins in the blood. Solutions of acid violet 17 or amido black are examples of protein stains. Alternatively, a chemical solution that

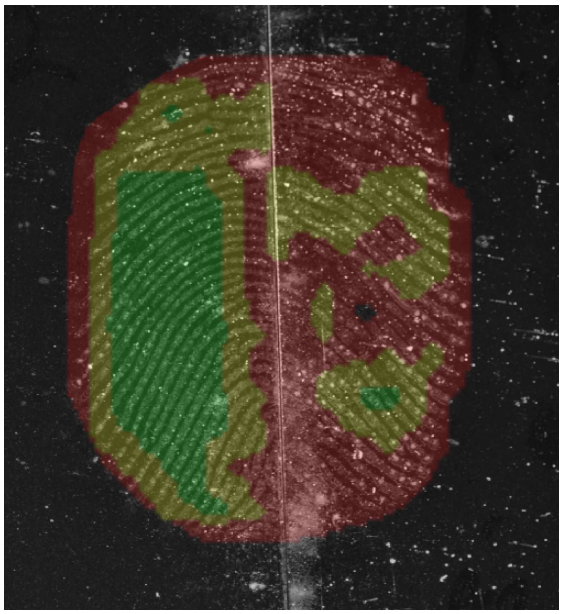

Figure 3.20: Clarity map of the CEFR developed portion is on the left and the slanted-CTF developed portion is on the right.

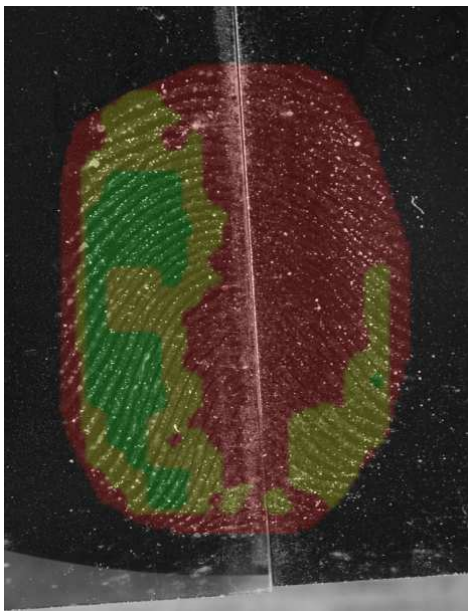

Figure 3.21: Clarity map of the CEFR developed portion is on the left and normally developed is on the right.

causes a peroxidase-activity color change when exposed to blood is used. Solutions of fluorescein or hemascein are examples. Dusting with a powder is commonly used to develop the non-bloody

part of the fingermark either before or after the bloody portion is developed.

The use of two development techniques on one fingermark may cause problems. Many of the techniques used to develop the bloody part involve the reaction of a solution with the fingermark and subsequent rinsing with another solution or water. The use of solutions and/or water often distorts the non-bloody part. Even if the non-bloody part is dusted prior to the solution treatment of the bloody part, the powder is removed during the rinsing phase. Extreme care must be exercised, often to little avail because of the delicate nature of fingermarks. Furthermore, repeated handling enhances the possibility of damaging the fingermark. Finally, the chemicals used to develop the bloody part can hinder the ability to collect DNA samples from the residual blood.

Clearly, a technique that does not rely on chemical interactions and which can simultaneously develop both the bloody and the non-bloody parts is needed. With the aim of exploiting the topology of both parts for simultaneous development, the deposition of a CTF on a partial bloody fingermark appears promising. The differential reflection of light from the various facets of the undulating CTF allow visualization. A detailed investigation was undertaken to assess the efficacy of the CEFR technique to develop partial bloody fingermarks on a representative set of non-porous substrates. Additionally, as the chemicals in the sebaceous secretion and the blood are preserved on entombment by the CTF, the possible collection of DNA samples at a later time is enticing. CTFs of several evaporant materials were deposited in order to decide on the optimal material for a specific substrate, and comparison was made with several traditional development techniques.

Substrates used for the optimization of CTF development on partial bloody fingermarks included: (i) brass, (ii) anodized aluminum, (iii) black ABS, (iv) white ABS, (v) black garbage bags, (vi) clear sandwich bags, (vii) black nylon, (viii) white nylon, (xi) white grocery bags, and (x) stainless steel. The results of this optimization study are given in Table 3.5 along with the best traditional development technique. The CTF and traditional technique were then compared using a split fingermark protocol; the technique which was found to perform better is in bold in Table 3.5. In Fig. 3.22 a partial bloody fingermark on stainless steel is shown. A 100-nm-thick CTF of nickel was used to develop both the bloody and non-bloody portion of the right side of the fingermark simultaneously. The left part of the same figure shows the development resulting from cyanoacrylate fuming followed by dusting with regular black powder.

It was found that CTF development was superior to traditional development methods for

Figure 3.22: Partial bloody fingermark on 420-grade stainless steel developed either (left) by the use of cyanoacrylate fuming followed by dusting with regular black powder or (right) by the deposition of a 100-nm-thick CTF of nickel. [Courtesy of Sarah Muhlberger]

partial bloody fingermarks on: brass, stainless steel, anodized aluminum, black and white ABS, white nylon, and clear soft plastic. CTF development was shown to be capable of simultaneously developing both the non-bloody and bloody portion of a partial bloody fingermark. This presents a significant advantage over traditional development techniques where multiple development techniques are used in sequence. In some cases the method used to develop one portion of a fingermark may damage the other portion. By developing both portions simultaneously the CTF technique minimizes the potential for this type of damage as well as damage cause in the general handling of the substrate. Additionally the CTF technique produces superior development for several forensically relevant substrates.

3.6 Sensitivity of CTF Development vs Traditional Techniques

In this section, I report on the ability of the CTF technique to develop fingermarks that are depleted in sebaceous secretions. Although on-scene fingermarks contain both eccrine and seba-

Table 3.5: Summary of the results of CTF optimization and comparison with the best traditional development technique (excluding VMD) for partial bloody fingermarks. The best performing technique is shown in bold. If neither technique is in bold, no suitable development was achieved. Note: Eu(tta)$_3$phen is an organic fluorescent material similar to Alq$_3$.

Substrate	Best Evaporant Material	CTF Thickness (nm)	Best Traditional Development Technique
Brass	**Alq$_3$**	100	Amido black and Black magnetic powder
Stainless Steel	**Nickel**	100	Cyanoacrylate and cyanoblue
Anodized Aluminum	**Alq$_3$**	100	Amido black and Black magnetic powder
ABS-black	**Chalcogenide glass**	1000	Amido black and White magnetic powder
ABS-white	**Chalcogenide glass**	1000	Amido black and Black magnetic powder
Nylon-black	Gold	50	Amido black and White magnetic powder
Nylon-white	**Chalcogenide glass**	1000	Amido black and Black magnetic powder
Soft Plastic-black (Garbage bag)	Eu(tta)$_3$phen	100	White magnetic powder
Soft Plastic-white (Grocery bag)	Eu(tta)$_3$phen	100	Black magnetic powder
Soft Plastic-clear (Sandwich bag)	**Gold**	50	Amido black and Black magnetic powder

ceous secretions, sebaceous secretions were chosen partly to limit the variability and complexity in the experimental protocol–to address that fraction of the fingermark residue which is accounted for in many commonly used on-scene development techniques and forms the bulk of the residue that gives the fingermark its topology. Eccrine secretions contain about 99% water that readily evaporates in many environmental conditions or becomes part of the sebaceous emulsion.

This investigation is important to ascertain the range of clarity of sebaceous fingermarks

that the CTF technique can develop. If this technique can develop a fingermark of low quality because it contains a low amount of secretions, then it is sensitive enough to be used in difficult cases. The clarity, details, and contrast of the fingermarks developed with the CTF technique were compared with those developed with selected traditional development techniques–which exploit physical and/or chemical interactions with the secretions to develop a fingermark. If the amount of reactants in the secretions is insufficient for the interaction(s) to occur, then the chosen traditional development technique would be ineffective. It was hypothesized that the CTF technique would be less affected by this problem because the CTF technique should not directly depend on the amount of reactants in the secretions but on the fingermark topology.

In order to prevent interference from eccrine secretions, the grooming process began by tightly wrapping clear thin plastic wrap around the fingertip. The fingertip was then wiped across the donor's forehead, nose, and chin for 10 seconds to collect secretions. Every second fingermark was placed on the substrate of interest until the 12th fingermark was made. The odd numbered fingermarks in every series were place onto a glass slide.

The substrates used in this study included: (i) brass, (ii) anodized aluminum, (iii) stainless steel, (iv) black nylon, (v) white nylon, (vi) black ABS, and (vii) white ABS. As before, a spit-print protocol was used to compare development methods. For each substrate investigated, the traditional development technique that gave the best results in our laboratory had been identified in Table 3.3. Accordingly, the following traditional techniques were used: (i) dusting with red fluorescent powder, (ii) dusting with black powder, (iii) dusting with white powder, (iv) cyanoacrylate fuming, and (v) cyanoacrylate fuming with cyanoblue dye. The result of these experiments are summarized in Table 3.6.

It was found that development with the CTF technique was more sensitive when compared to selected traditional techniques on: brass and anodized aluminum. Additionally, the CTF technique exhibited similar sensitivity when compared to the selected traditional techniques on: stainless steel black and white ABS, and black and white nylon.

Table 3.6: Summary of the result of experiments to compare the sensitivity of the CTF technique with traditional techniques (excluding VMD). The table lists the best evaporant material and the best traditional development technique, with the better performing of the two in bold. If neither technique is in bold neither technique was found to be superior.

Substrate	Best Evaporant Material	CTF Thickness (nm)	Best Traditional Development Technique
Brass	**Chalcogenide glass**	1000	Cyanoacrylate fuming and Black powder
Stainless Steel	Chalcogenide glass	1000	Cyanoacrylate fuming and Cyanoblue
Anodized Aluminum	**Alq_3**	100	Black magnetic powder
ABS-black	Gold	50	White magnetic powder
ABS-white	Alq_3	100	Black magnetic powder
Nylon-black	Alq_3	100	Red flourescent powder
Nylon-white	Chalcogenide glass	1000	Black powder

3.7 CTF Development vs. Vapor-Metal-Deposition Technique

In this section I report on the comparison between the CTF technique and another fingermark development technique that utilizes thermal evaporation termed vapor-metal deposition (VMD). Beyond this similarity, there are many differences between the two techniques including: (i) the morphology of the deposited thin film and (ii) the mechanism by which each techniques makes fingermarks visible and identifiable. These differences are discussed in Sec. 3.7.1 and 3.7.2 respectively.

The substrates used in this study included: (i) glass, (ii) clear sandwich bags, (iii) white grocery bags, (iv) the smooth side of Scotch Multitask® tape, (v) black garbage bags, (vi) and partial bloody fingermarks on stainless steel. As before, a spit-print protocol was used to compare development methods. For each substrate investigated, the evaporant material that gave the best result as identified in Table 3.3 was used. Accordingly, the following evaporants were used: (i)

chalcogenide glass, (ii) gold, (iii) nickel, (iv) gold, (v) nickel, (vi) and chalcogenide glass. The result of these experiments are summarized in Table 3.7.

3.7.1 Thin-Film Morphology

Before I present the results of our comparison between the CTF and VMD techniques for fingermark development, a brief discussion on relevant aspects of thin-film growth and morphology is appropriate.

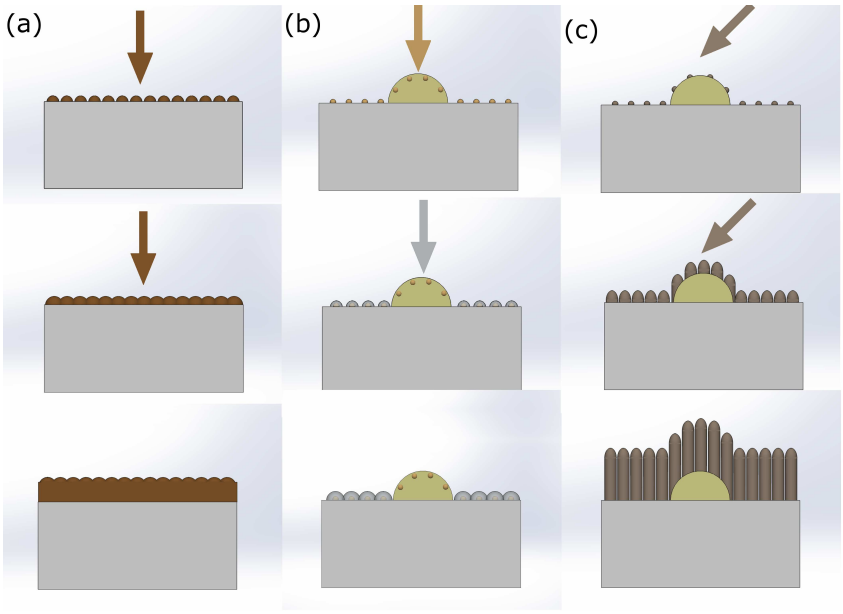

Figure 3.23: Top to bottom: schematics of three main stages of (a) thermal evaporation with the vapor flux normally incident on a planar substrate, (b) the VMD technique implemented on a substrate with a fingermark, and (c) the CEFR technique implemented on a substrate with a fingermark.

As shown in Fig. 3.23(a), several stages occur during the conventional deposition of a thin film on a flat surface by a thermal evaporation method. During the first stage illustrated in the top panel of Fig. 3.23(a), the vapor arriving normally at the substrate initially condenses onto the surface as discrete clusters of atoms. These discrete clusters of atoms then serve as nucleation sites on which the adatoms in the subsequently arriving vapor collect. In this way the initial nucleation sites grow as discrete islands until they reach such a size that they begin to coalesce, as shown in the middle panel of Fig. 3.23(a). Nanoscale structures are formed thereby, their morphology depending on the deposition conditions. The film then begins to grow at a

relatively uniform rate with a density of between 80 and 100% of its bulk value depending on deposition parameters, as shown in the bottom panel of Fig. 3.23(a). The morphology of the thin film depends on the morphology of the constituent nanoscale structures created by coalescence of the islands formed during the very early stages of growth.

With the VMD technique, the inability of zinc to form nucleation sites on many materials while readily clustering on gold nucleation sites, is exploited to create selective deposition that gives rise to visual contrast. The VMD process is schematically depicted in Fig. 3.23(b). A very small amount of gold is deposited onto the sample prior to evaporation of zinc. Gold readily condenses onto many materials. In the typical case of a fingermark, gold forms nucleation sites on the non-fingermarked portion of the substrate, whereas it slightly penetrates the sebaceous material composing the fingermark. This is shown in the top panel of Fig. 3.23(b). Zinc is evaporated next. Gold nucleation sites being available for zinc condensation on the background but not on the sebaceous material, zinc envelops the gold nucleation sites on the background only, as depicted in the middle panel of Fig. 3.23(b). As zinc continues to be deposited, the zinc islands continue to expand. However, as deposition is stopped when the film is still in the island-growth stage, the film may be characterized as an assembly of somewhat hemispherical islands of radius of about 25 nm, as shown in the bottom panel of Fig. 3.23(b).

For the CTF (CEFR) technique, as shown schematically in the top panel of Fig. 3.23(c), the substrate's surface is positioned obliquely with respect to the direction of the incident vapor. This results in self-shadowing as well as competition among the initial nucleation sites for growth, with the assumption that the substrate is stationary during deposition. The taller nucleation sites preferentially receive the incoming vapor, while the shorter nucleation sites receive a lesser amount of the vapor. This competitive growth continues from the initial nucleation sites as they grow into islands. By the time the islands have reached a height of about 25 nm, depending on the material being deposited, the taller amongst them have been established as the ones to receive a greater quantity of the arriving vapor. The vapor that is now reaching the taller islands will only arrive at their uppermost tips, and the islands grow roughly towards the vapor source without substantially increasing in diameter, thereby giving rise to a slanted-columnar morphology. Because the substrate is rotated rapidly about the central normal axis, the columns grow along the substrate's surface normally rather than tilted toward the vapor source. The materials which have been selected for the CTF technique are able to condense on both the

substrate and sebaceous materials. As a result, the columns are able to grow conformally over the entire surface, covering both the fingermark and substrate, as shown in the middle panel of Fig. 3.23(c). The topography of a non-planar fingermarked substrate is translated along the columns to produce a replicate surface constituted by the upper surface of the columns. This is exemplified by the bottom panel of Fig. 3.23(c).

3.7.2 Mechanism by Which Fingermark Visibility is Improved

In both the CTF and the VMD techniques, the fingermark is developed by producing contrast between the substrate/background and the sebaceous material. A VMD-treated substrate offers the needed information as a visual contrast: the non-fingermarked portion of the substrate appears dark because it is coated with zinc (or zinc suboxide), while the fingermarked portion has the color of the substrate because the fingermark is highly transparent.

For fingermarks developed with the CTF technique, the substrate appears dark (resp., bright) while the fingermark appear bright (resp., dark) in comparison, when a dark (resp., bright) evaporant material is used. This visual contrast is produced by the way in which the conformally coated, non-planar fingermark scatters incoming light quite differently from the relatively planar coated non-fingermarked portion of the substrate. Since the CTF thickness over both parts of the substrate is uniform, light incident at a higher elevation differs in phase from light incident at a lower elevation. Therefore, light reflected from a higher elevation differs in phase from light reflected from a lower elevation. Additional dependence on elevation arises for a non-metallic CTF because light can partially penetrate the non-metallic CTF as well as the covered fingermark, thereby incorporating a dependence on the optical properties and amounts of all materials involved.

3.7.3 Experimental Details

Fingermarks were collected following the procedure established in Sec. 3.3.1. The selected substrates use for comparison included: (i) stainless steel, (ii) black garbage bags, (iii) white grocery bags, (iv) clear sandwich bags, (v) Gloss Finish Scotch Multitask® tape, (vi) glass microscope slides, and (vii) fingermarks were placed on silicon to aid in obtaining SEM images of the morphology of the respective thin film. A split-fingermark protocol was used to allow for the side-by-side

comparison of the CTF- and VMD-developed fingermarks.

3.7.4 Results and Discussion

It was found that the CTF technique performed better on clear sandwich bags while the VMD technique was found to be superior on Gloss Finish Scotch Multitask® tape. Both techniques worked well on glass but there was a greater contrast between the substrate and fingermark when the CTF technique was used. Neither technique worked well on black garbage bags of a generic brand. It was found that using the CTF and the VMD techniques can lead to the degradation of non-bloody fingermarks on stainless steel, but the degradation using the CTF technique is minimal. These results are shown in Table. 3.7.

To demonstrate the differences in thin-film morphology due to the application of the CTF and the VMD techniques, cross-sectional SEM images were taken of fingermarks developed with both techniques. Figure 3.24(a) shows a fingermark developed with with VMD. The islands have grown just enough as to begin coalescing. The zinc deposit is roughly 25 nm thick and as yet mostly discontinuous.

This can be contrasted with Figs. 3.24(b-d) in which cross-sectional SEM images of CTFs are presented. In Fig. 3.24(b), a $\sim$ 50-nm-thick gold film can be seen on a planar substrate of silicon. Discrete vertical columns growing from the underlying substrate are clearly evident, thereby underscoring the columnar morphology of even the thinnest films deposited by the CTF technique for fingermark development.

Figure 3.24(c) depicts a $\sim$ 100-nm-thick CTF of nickel deposited over some sebaceous material. Not only the silicon substrate, but the fingermark residue itself is coated by the CTF. Finally, Fig. 3.24(d) is an image of an $\sim$ 1800-nm-thick chalcogenide-glass CTF deposited over some sebaceous material on a glass slide. The upright-columnar morphology due to rapid substrate rotation is as evident in this image as in Fig. 3.24(b). Moreover, Fig. 3.24(d) demonstrates the high level of uniformity found in the thickness of the CTF covering both the non-fingermarked and fingermarked portions of the substrate.

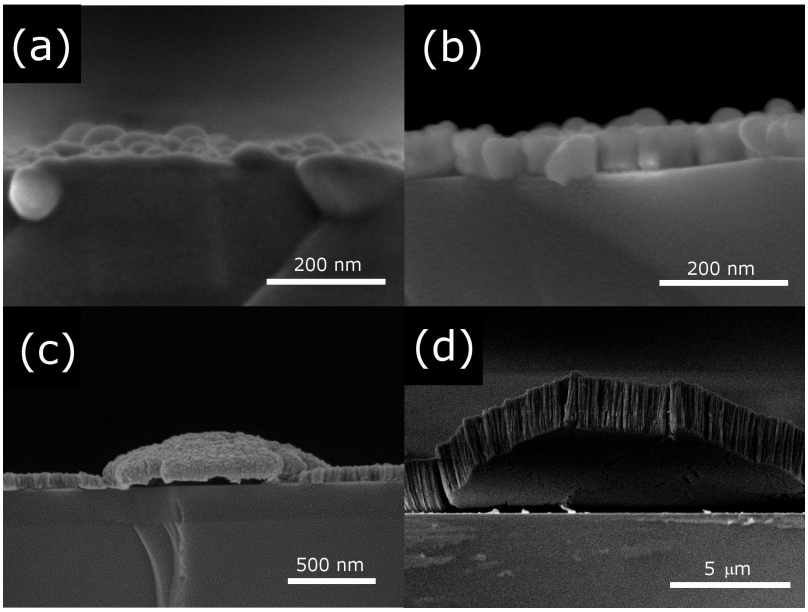

Figure 3.24: Cross-sectional SEM images of (a) a zinc film deposited atop a gold film on a fingermarked silicon substrate by the VMD technique, (b) a gold CTF deposited on a planar silicon substrate by the CTF technique, (c) a fingermark ridge on a silicon substrate conformally coated with a nickel CTF, and (d) a fingermark ridge on a glass slide conformally coated with a chalcogenide-glass CTF.

3.8 Concluding Remarks

Extensive studies were carried out to ascertain the efficacy of the physical vapor deposition of a conformal columnar thin film on a fingermark on a non-porous substrate of forensic relevance for fingermark development and visualization. CTF development was attempted in a vacuum chamber, by implementing the conformal-evaporated-film-by-rotation technique, which is an adaptation of a basic thin film deposition technique called thermal evaporation for the conformal coating of non-planar surfaces. On all combinations of the evaporant material and the surface bearing the fingermark, several traditional development techniques were also implemented. In many but not all instances, the CTF development technique either outperformed the best traditional development technique or performed equally well.

In some instances, first fuming the fingermark with cyanoacrylate and then depositing a CTF on it produced significantly superior development, most possibly because the fuming step enhance the fingermark topology, which was then revealed by the CTF frown on top. This two-step process is promising as a hybrid development technique.

Table 3.7: Summary of the result of experiments to compare the CTF technique with the VMD technique. The table lists the best CTF material for each substrate. Substrates for which the CTF technique was found to be superior or indicated by bold text, those for which VMD was found to be superior are italicized, and if neither technique was found to be superior plain text is used.

Substrate	Best Evaporant Material	CTF Thickness (nm)
Glass	Chalcogenide glass	1000
Stainless Steel (partial bloody)	Chalcogenide glass	1000
Clear Sandwich Bag	Gold	50
White Grocery Bag	Nickel	100
Black Garbage Bag	Nickel	100
Scotch Multitask® tape	Gold	50

Systematic optimization studies lead to the conclusion that only a moderate vacuum is needed in the CEFR apparatus to develop fingermarks, whereas the pressures in proof-of-principle studies [46, 54] were lower by two orders of magnitude. This finding will greatly facilitate the use of the CTF development technique in crime laboratories, and also buttresses the possibility of producing fieldable CEFR apparatus capable of developing fingermarks on-scene.

In the second setting for testing the efficacy of thermally evaporated conformal thin films on non-traditional/non-planar substrates, the development of sebaceous fingermarks placed forensically relevant substrates was selected. This setting demonstrates three key features of thermal evaporation: (i) compatibility with very temperature-sensitive substrates, (ii) capability of simultaneously coating substrates of vastly different chemical and physical properties, and (iii) an ability to conformally deposit films with vertical-columnar morphology which improved functionality over normally deposited and slanted-CTFs without substrate rotation.

Chapter 4

A Warm-Up: Modeling the Grating Coupled Excitation of Tamm Waves[‡]

As the third setting for testing the efficacy of thermally evaporated conformal thin films on non-traditional/non-planar substrates, the observation of a new class of electromagnetic surface wave, termed a Dyakonov-Tamm wave, was selected. This setting was selected to demonstrate the ability to conformally deposit films with a specific and complicated morphology which imparts certain optical properties to the resulting film. This required preliminary work which is reported in Ch. 4 and 5. The theoretical results produced in Ch. 5 guide the observation of the Dyakonov–Tamm wave guided by a planar interface in Ch. 6, and guided by a non-planar interface in Ch. 7.

4.1 Chapter Summary

Here I present a study of multiple Tamm waves whose propagation is guided by the interface of a periodically corrugated homogeneous dielectric material and a periodically nonhomogeneous material. I present theory and simulation that supports the claim that multiple Tamm waves of different linear polarization and phase speed can be supported by the interface. This is done by comparing results of the canonical boundary-value problem for the interface of two semi-infinite materials with the angular location of peaks in absorptance while varying the incident angle.

[‡]This chapter is based on: Pulsifer, D. P., Faryad, M., and Lakhtakia, A., "Grating-coupled excitation of Tamm waves," *Journal of the Optical Society of America B* **29**, 2260–2269 (2012).; erratum: **30**, 177 (2013).

Evidence that the Tamm waves are localized to the interface is found, and an approach for experimental verification is formulated.

This chapter represents a warm-up in which I develop experience in modeling electromagnetic surface waves. The methods used here to investigate the Tamm wave are extended in Ch. 5 to model the excitation and propagation of the Dyakonov–Tamm wave.

4.2 Electromagnetic Surface Waves

Electromagnetic surface waves are a class of electromagnetic phenomena which propagate guided by the interface of two dissimilar materials, and the optical properties of the partnering materials dictate the type of electromagnetic surface wave which can be supported at the interface [75]. This localization to the interface gives electromagnetic surface waves high sensitivity to changes in the optical properties of the partnering materials near the interface [76]. Changes in the optical properties near the interface can cause the wavenumber of the electromagnetic surface wave to change or the phenomena to disappear entirely [75]. This sensitivity is most often exploited for sensing applications [77–80], but electromagnetic surface waves also show potential for applications in microscopy, photovoltaics, and communication [75]. Many of these applications have been realized for plasmonic electromagnetic surface waves [81–83], but due to the much lower dissipation of dielectrics when compared to metals, optical electromagnetic surface waves may find a multitude of new applications.

Historically, the first prediction of an electromagnetic surface wave excited at optical frequencies was made in 1957 by Ritchie, when he presented a plasma oscillation explanation for energy losses of fast electrons in thin metal films [84]. In the $1960's$ surface plasmon waves (SP) were extensively studied by Turbadar, Raether, Kretschmann, and Otto resulting in the development of simple methods to optically excite SP waves at the interface between a metal and air [85–87]. In the case where air is replaced by a homogeneous, isotropic, dielectric material the electromagnetic surface wave is described as a surface-plasmon-polariton (SPP) wave. In the decades since, the study of electromagnetic surface waves has primarily centered on SPP waves and their applications.

A second type of electromagnetic surface wave was predicted in 1977 [88]. This wave was predicted to occur at the interface of two isotropic dielectric materials, at least one of which was

periodically non-homogeneous in the direction normal to the interface. These electromagnetic surface waves were named Tamm waves as they are analogous to the electronic states predicted to exist at the surface of a crystal by Tamm in 1932 [89]. The experimental observation of Tamm waves followed shortly thereafter [90] and more recently their application to sensing has been demonstrated as well [79, 80, 91].

A third type of electromagnetic surface wave was named for Dyakonov's 1988 work [92]. This surface wave was predicted to occur at the interface of two homogenious dielectric materials, at least one of which was anisotropic [93]. The existence of the Dyakonov wave was verified by Takayama et al. in 2009 using the interface of a potassium titanyl phosphate biaxial crystal and an index-matching fluid in a prism-coupled configuration. The sensitivity of the Dyakonov wave to different index-matching fluids also demonstrated its applicability to sensing [94]. Observation of the Dyakonov wave was particularly difficult due to its limited angular existence domain [93].

Dyakonov–Tamm waves propagate guided by the interface of two dielectric materials, one of which must be anisotropic and periodically nonhomogeneous normal to the interface [92, 93]. The existence of the Dyakonov–Tamm wave [47] was predicted in 2007 by Polo and Lakhtakia when the anisotropic material properties that allow for Dyakonov waves, and the periodically nonhomogeneous material properties that support Tamm waves [89] were considered in combination. As with other surface waves [76], Dyakonov–Tamm waves are highly sensitive to the optical properties of the material found near the interface, and could find applications in optical sensing, waveguiding, and integrated optics [93].

4.3 Introduction

Tamm developed theory to describe the electronic surface states of wide band-gap semiconductors in 1932 [89]. Analogous to these Tamm states are Tamm waves which are a class of electromagnetic surface waves (ESWs) that are guided by the interface of a periodically nonhomogeneous isotropic dielectric material and a homogeneous isotropic dielectric material or a periodically nonhomogeneous isotropic dielectric material [95, 96]. Although the existence of Tamm waves had been inferred experimentally in 1978 [90], these were clearly observed in 1999 when Robertson and May utilizing a prism coupling configuration. In this experiment, a sapphire prism was used to couple light into a 1D photonic crystal consisting of alternating layers of TiO_2 and SiO_2 that

had been deposited on a sapphire substrate. A high-refractive-index substrate such as sapphire was used to satisfy the conditions for coupling light into the 1D photonic crystal which has a high average refractive index due to the presence of TiO_2. Reflectance of an *s*-polarized laser beam was measured at a single near-infrared frequency while the angle of incidence was made more oblique. Through this experiment they observed a single narrow dip (0.08^o wide) in reflectance corresponding to the launch of a Tamm wave. The observation was confirmed at three different near-infrared frequencies [97].

Recently, by solving the canonical boundary value problem of a semi-infinite rugate filter matched with a semi-infinite homogeneous dielectric [96], it has been theoretically shown that materials can be selected to allow multiple Tamm waves at a single interface to be excited by both *s*- and *p*- polarized incident light of a single frequency. These multiple Tamm waves differ in their electric and magnetic field profiles. Based on these results, I propose a method for observing multiple Tamm waves through a grating-coupled configuration. Grating coupling differs from prism coupling in that a periodically corrugated interface allows ESWs to be launched from air rather than through the use of a prism [98]. This is advantageous in that it simplifies the experimental set-up by eliminating the selection of an appropriate prism/substrate pair, thereby giving us greater flexibility in selecting substrate materials and materials for the periodically nonhomogeneous partnering material [99]. This has the added benefit of removing prism/index-matching-fluid and index-matching fluid/substrate interfaces which could complicate experimental verification. Additionally, the use of grating coupling would allow for the measurement of reflectance vs incidence angle, transmittance vs incidence angle, or both. The periodic patterning of substrates with features on the scale of an optical wavelength has become commonplace [100] and does not stand as a barrier to the implementation of a grating-coupled configuration for observing ESWs.

Here I investigate theory and provide calculations for a case where multiple ESWs can be launched through grating coupling of periodically nonhomogeneous isotropic dielectric layer in the form of a rugate filter with a periodically corrugated homogeneous isotropic dielectric layer. These calculations demonstrate that resonant peaks in absorptance are due to waves localized to the rugate-filter/dielectric interface. I also go on to demonstrate the effect of varying several parameters of both the rugate filter and the dielectric layer. Finally, I give modeling results that set the stage for multiple Tamm waves to be experimentally observed through measuring

transmittance and reflectance vs. incident angle. The material parameters for the rugate filter are similar to those taken from Maab et al. [96] to allow for easy comparison.

Since the theoretical formulation of the boundary value problem undertaken in this paper is the same as has been provided elsewhere [101], only a brief description is provided in Sec. 4.4. Representative numerical results showing the excitation of Tamm waves in grating-coupled configuration are provided in Sec. 4.5. Finally, a few comments on the experimental implementation of the problem undertaken in this paper are provided in Sec. 4.5.4, and concluding remarks are presented in Sec. 4.6. An $\exp(-i\omega t)$ time-dependence is implicit, with ω denoting the angular frequency. The free-space wavenumber, the free-space wavelength, and the intrinsic impedance of free space are denoted by $k_0 = \omega\sqrt{\epsilon_0\mu_0}$, $\lambda_0 = 2\pi/k_0$, and $\eta_0 = \sqrt{\mu_0/\epsilon_0}$, respectively, with μ_0 and ϵ_0 being the permeability and permittivity of free space. Vectors are in boldface, the asterisk denotes the complex conjugate, and the Cartesian unit vectors are identified as $\mathbf{u}_x$, $\mathbf{u}_y$, and $\mathbf{u}_z$.

4.4 Theoretical formulation in brief

The boundary-value problem is shown schematically in Fig. 4.1. The regions $z < 0$ and $z > d_3$ are vacuous, the region $0 \leq z < d_1$ is occupied by a rugate filter of period 2Ω and relative permittivity

$$\epsilon_{rug}(z) = \left[\left(\frac{n_b + n_a}{2}\right) + \left(\frac{n_b - n_a}{2}\right)\sin\left(\pi\frac{d_2 - z}{\Omega}\right)\right]^2 , \tag{4.1}$$

and the region $d_2 < z \leq d_3$ is occupied by an isotropic homogeneous dielectric material with spatially uniform relative permittivity $\epsilon_d = n_d^2$.

The region $d_1 < z < d_2$ contains a surface-relief grating with period L along the x axis. The relative permittivity $\epsilon_g(x,z) = \epsilon_g(x \pm L, z)$ in the reference unit cell $0 < x < L$ of this region is taken to be as

$$\epsilon_g(x,z) = \begin{cases} \epsilon_d - [\epsilon_d - \epsilon_{rug}\ (z)]\,\mathcal{U}\left(d_2 - z - g(x)\right), & x \in (0, L_1) \\ \epsilon_{rug}(z), & x \in (L_1, L) \end{cases} , \tag{4.2}$$

with

$$g(x) = (d_2 - d_1)\sin\left(\frac{\pi x}{L_1}\right), \quad L_1 \in (0, L), \tag{4.3}$$

and

$$\mathcal{U}(\zeta) = \begin{cases} 1, & \zeta \geq 0, \\ 0, & \zeta < 0. \end{cases} \tag{4.4}$$

The thickness of the homogeneous dielectric material is $L_d = d_3 - d_2$, the depth of the surface-relief grating is $L_g = d_2 - d_1$, and the thickness of the rugate filter is d_1.

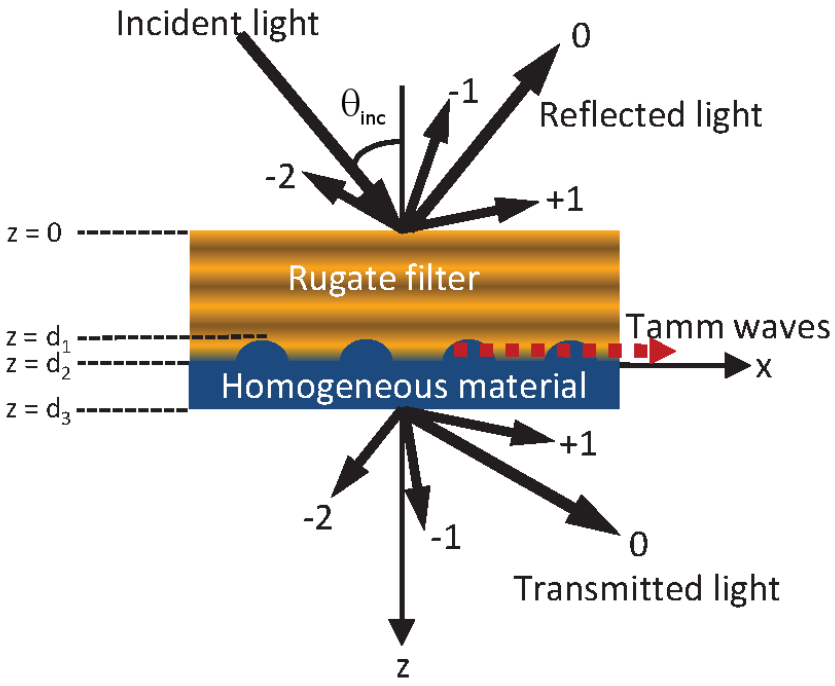

Figure 4.1: Schematic of the boundary-value problem involving the periodically corrugated interface of a homogeneous dielectric material and a periodic multi-layered isotropic dielectric material. The incident field is a plane wave, whereas both the reflected and transmitted fields are discrete angular spectrums of plane waves. The label "0" is attached to the specular components of the reflected and transmitted plane waves, the nonspecular components being labeled as "± 1", etc.

Let a plane wave propagating in the xz plane be incident on the plane $z = 0$ at an angle θ_{inc} with respect to the z axis. The incident, reflected, and transmitted electric field phasors can be written in terms of the Floquet harmonics as follows:

$$\mathbf{E}_{inc}(\mathbf{r}) = \sum_{n\in\mathbb{Z}} \left(a_s^{(n)} \mathbf{u}_y + a_p^{(n)} \mathbf{p}_n^+ \right) \exp\left[i \left(k_x^{(n)} x + k_z^{(n)} z \right) \right] , \; z \leq 0 \,, \tag{4.5}$$

$$\mathbf{E}_{ref}(\mathbf{r}) = \sum_{n\in\mathbb{Z}} \left(r_s^{(n)} \mathbf{u}_y + r_p^{(n)} \mathbf{p}_n^- \right) \exp\left[i \left(k_x^{(n)} x - k_z^{(n)} z \right) \right] , \; z \leq 0 \,, \tag{4.6}$$

$$\mathbf{E}_{tr}(\mathbf{r}) = \sum_{n\in\mathbb{Z}} \left(t_s^{(n)} \mathbf{u}_y + r_p^{(n)} \mathbf{p}_n^+ \right) \exp\left\{ i \left[k_x^{(n)} x + k_z^{(n)} \left(z - d_3 \right) \right] \right\} \,, \; z \geq d_3 \,. \tag{4.7}$$

The order of a Floquet harmonic is denoted by $n \in \mathbb{Z}$, the wavenumbers

$$k_x^{(n)} = k_0 \sin\theta_{inc} + 2\pi n / L \tag{4.8}$$

and

$$k_z^{(n)} = +\sqrt{k_0^2 - \left(k_x^{(n)} \right)^2} \,, \tag{4.9}$$

and the unit vector

$$\mathbf{p}_n^{\pm} = \mp \frac{k_z^{(n)}}{k_0} \hat{\mathbf{u}}_x + \frac{k_x^{(n)}}{k_0} \hat{\mathbf{u}}_z \,. \tag{4.10}$$

Coefficients for the incident field phasor are denoted by $a_{s,p}^{(n)}$, for the reflected field phasor by $r_{s,p}^{(n)}$, and for the transmitted field phasor by $t_{s,p}^{(n)}$, where the subscript s identifies the s-polarization state and the subscript p identifies the p-polarization state. When the incident plane wave is p polarized, $a_p^{(n)} = \delta_{n0}$ V m^{-1} and $a_s^{(n)} \equiv 0 \, \forall n \in \mathbb{Z}$, where $\delta_{nn'}$ is the Kronecker delta; when the incident plane wave is s polarized, $a_p^{(n)} \equiv 0$ and $a_s^{(n)} = \delta_{n0}$ V m^{-1} $\forall n \in \mathbb{Z}$. The Floquet harmonics of order $n = 0$ in Eqs. (4.6) and (4.7) represent specularly reflected and transmitted plane waves, respectively, whereas nonspecular plane waves—whether of the propagating or the evanescent type—are represented by the Floquet harmonics of order $n \neq 0$.

The relative permittivity in the region $0 \leq z \leq d_3$ can be expanded as a Fourier series with respect to x as

$$\epsilon(x,z) = \sum_{n\in\mathbb{Z}} \epsilon^{(n)}(z) \exp\left(i 2\pi n x / L \right) \,, \quad z \in [0, d_3] \,, \tag{4.11}$$

where

$$\epsilon^{(0)}(z) = \begin{cases} \epsilon_{rug}(z) \,, & z \in [0, d_1] \,, \\ \frac{1}{L} \displaystyle\int_0^L \epsilon_g(x,z) dx \,, & z \in (d_1, d_2) \,, \\ \epsilon_d \,, & z \in [d_2, d_3] \,, \end{cases} \tag{4.12}$$

and

$$\epsilon^{(n)}(z) = \begin{cases} \frac{1}{L} \displaystyle\int_0^L \epsilon_g(x,z) \exp\left(-i 2\pi n x / L \right) dx \,, & z \in (d_1, d_2) \\ 0 \,, & \text{otherwise} \end{cases} \; ; \; \forall \; n \neq 0 \,. \tag{4.13}$$

The electric field phasor may be written in the region $0 \leq z \leq d_3$ in terms of the Floquet harmonics as

$$\mathbf{E}(r) = \sum_{n\in\mathbb{Z}} \mathbf{E}^{(n)}(z) \exp\left(ik_x^{(n)} x\right) \ , \ z \in [0, d_3] \ , \tag{4.14}$$

with $\mathbf{E}^{(n)}(z) = E_x^{(n)}(z)\hat{\mathbf{u}}_x + E_y^{(n)}(z)\hat{\mathbf{u}}_y + E_z^{(n)}(z)\hat{\mathbf{u}}_z$ unknown. An analogous expression is written for $\mathbf{E}(r)$ in the same region.

Substitution of Eqs. (4.11) and (4.14) in the frequency-domain Maxwell curl postulates results in an infinite system of coupled first-order differential equations which can not be solved on a digital computer. Therefore, the Floquet modes are restricted to $|n| \leq N_t$, and the finite system of ordinary differential equations can then be expressed compactly as

$$\frac{d}{dz}\left[\mathbf{f}(z)\right] = i\left[\underline{\underline{P}}(z)\right] \cdot \left[\mathbf{f}(z)\right], \quad z \in (0, d_3) \ , \tag{4.15}$$

where the column vector $[\mathbf{f}(z)]$ with $4(2N_t + 1)$ components is defined as

$$\left[\mathbf{f}(z)\right] = \left[\left[\mathbf{E}_x(z)\right]^T, \ \left[\mathbf{E}_y(z)\right]^T, \ \eta_o\left[\mathbf{H}_x(z)\right]^T, \ \eta_o\left[\mathbf{H}_y(z)\right]^T\right]^T \tag{4.16}$$

and the $4(2N_t + 1) \times 4(2N_t + 1)$-matrix $\left[\underline{\underline{P}}(z)\right]$ is given by

$$\left[\underline{\underline{P}}(z)\right] = \begin{bmatrix} [\underline{0}] & [\underline{0}] & [\underline{0}] & k_0\left[\underline{I}\right] - \frac{1}{k_0}\left[\underline{\underline{K}}_x\right] \cdot \left[\underline{\epsilon}(z)\right]^{-1} \cdot \left[\underline{\underline{K}}_x\right] \\ [\underline{0}] & [\underline{0}] & -k_0\left[\underline{I}\right] & [\underline{0}] \\ [\underline{0}] & \frac{1}{k_0}\left[\underline{\underline{K}}_x\right]^2 - k_0\left[\underline{\epsilon}(z)\right] & [\underline{0}] & [\underline{0}] \\ k_0\left[\underline{\epsilon}(z)\right] & [\underline{0}] & [\underline{0}] & [\underline{0}] \end{bmatrix} . \tag{4.17}$$

Whereas $[\underline{0}]$ is the $(2N_t + 1) \times (2N_t + 1)$ null matrix, $[\underline{I}]$ is the $(2N_t + 1) \times (2N_t + 1)$ identity matrix, $\left[\underline{\underline{K}}_x\right] = \text{diag}\left[k_x^{(n)}\right]$, and $\left[\underline{\epsilon}(z)\right] = \left[\epsilon^{(n-m)}(z)\right]$. Furthermore, the $(2N_t + 1)$ column vector

$$\left[\mathbf{X}_\sigma(z)\right] = \left[X_\sigma^{(-N_t)}(z), \ X_\sigma^{(-N_t)}(z), \ ..., \ X_\sigma^{(0)}(z), \ ..., \ X_\sigma^{(N_t-1)}(z), \ X_\sigma^{(N_t)}(z)\right]^T , \tag{4.18}$$

for $X \in \{E, H\}$ and $\sigma \in \{x, y, z\}$.

The boundary-value problem was formulated using the well-known rigorous coupled-wave approach(RCWA) [102,103] and was implemented using a stable algorithm [101,104]. The accuracy

of the solution using RCWA depends on the value of N_t, the number of terms of Floquet harmonics in the representation of field phasors being $2N_t+1$. As the formulation of the boundary-value problem and the numerical algorithm have been explained elsewhere in detail [101], I skip the details to go directly to representative numerical results in the next section.

4.5 Numerical Results and Discussion

For p-polarized incidence,

$$R_p = \sum_{n=-N_t}^{N_t} |r_p^{(n)}|^2 \,\mathrm{Re}\left(\frac{k_z^{(n)}}{k_z^{(0)}}\right) \tag{4.19}$$

is the total reflectance and

$$T_p = \sum_{n=-N_t}^{N_t} |t_p^{(n)}|^2 \,\mathrm{Re}\left(\frac{k_z^{(n)}}{k_z^{(0)}}\right) \tag{4.20}$$

is the total transmittance. The corresponding quantities for s-polarized incidence are

$$R_s = \sum_{n=-N_t}^{N_t} |r_s^{(n)}|^2 \,\mathrm{Re}\left(\frac{k_z^{(n)}}{k_z^{(0)}}\right) \tag{4.21}$$

and

$$T_s = \sum_{n=-N_t}^{N_t} |t_s^{(n)}|^2 \,\mathrm{Re}\left(\frac{k_z^{(n)}}{k_z^{(0)}}\right) , \tag{4.22}$$

respectively. The quantities of greatest interest are the absorptances

$$A_p = 1 - R_p - T_p \tag{4.23}$$

and

$$A_s = 1 - R_s - T_s \,, \tag{4.24}$$

both computed as functions of θ_{inc}.

All calculations were made for free-space wavelength $\lambda_0 = 633$ nm. In order to study the excitation of Tamm waves, the constitutive parameters of partnering dielectric materials were chosen from Ref. [96]. Thus, $n_a = 1.45$, $n_b = 2.32$, and $\Omega = \lambda_0$ were fixed for the rugate filter, whereas n_d was kept variable. The chosen parameters allowed a comparison of results obtained for the grating-coupled configuration in this paper and the canonical boundary-value problem in

Ref. [96]. For the computation of absorptances, $N_t = 10$ was fixed after ascertaining that the absorptances for $N_t = 10$ converged to within $\pm 1\%$ when $N_t = 11$.

4.5.1 Canonical boundary-value problem

The corresponding canonical boundary-value problem—when both partnering materials are semi-infinite in thickness and their interface is planar—has already been solved with the assumption that a Tamm wave propagates along the x axis with an $\exp(i\kappa x)$ variation and is independent of y [96]. When $n_d = 1.515$, four p-polarized Tamm waves are possible, one each with relative wavenumber $\kappa/k_0 \in \{1.5496, 1.7553, 1.9822, 2.2034\}$; likewise, four s-polarized Tamm waves are possible with relative wavenumber $\kappa/k_0 \in \{1.5560, 1.7735, 1.9966, 2.2144\}$.

4.5.2 Grating-coupled configuration

The way to identify the excitation of a Tamm wave is to first plot the absorptances A_p and A_s as functions of the incidence angle θ_{inc}, and then identify those absorptance peaks whose angular location depends on neither the thickness d_1 of the rugate filter nor the thickness L_d of the homogenous partnering material beyond some threshold values of both thicknesses. I set $n_d = n'_d(1 + i\delta)$ with $\delta = 10^{-4}$ for all numerical results reported for the grating-coupled configuration, so that significant values of absorptances would help identify guided-wave propagation.

Accordingly, A_p and A_s were calculated as functions of θ_{inc} and are presented in Figs. 4.2 and 4.3, respectively, when $n'_d = 1.515$, $L_d = \lambda_0$, $L_g = 50$ nm, and $d_1 \in \{4\Omega, 6\Omega, 8\Omega\}$. Three values of d_1 were chosen to identify and rule out the waveguide modes that can propagate in the bulk of finitely thick rugate filter [97], because waveguide modes must depend on the thickness of the dielectric material [105].

In Fig. 4.2, four A_p-peaks at $\theta_{inc} \in \{11.976, 24.364, 40.130, 60.388\}$ deg are independent of the thickness d_1 of the rugate filter beyond some threshold value. The relative wavenumber $k_x^{(1)}/k_0$ of the Floquet harmonic of order $n = 1$ is provided in Table 4.1 for these values of θ_{inc}. Also provided in Table 4.1 are values of κ/k_0 predicted by the solution of the canonical boundary-value problem. The two sets of data agree very well, indicating that all four p-polarized Tamm waves are very likely excited in the grating-coupled configuration as Floquet harmonics of order $n = 1$.

The angular location of the A_p-peak at $\theta_{inc} \simeq 12$ deg varies slightly in Fig. 4.2 with the

Table 4.1: Angular location θ_{inc} and relative wavenumber $k_x^{(1)}/k_0$ of the Floquet harmonic of order $n = 1$ for all four A_p-peaks in Fig. 4.2 and all four A_s-peaks in Fig. 4.3 that are independent of the thickness d_1 beyond some threshold value. Also shown are matching values of κ/k_0 predicted by the solution of the canonical boundary-value problem for $\delta = 0$.

θ_{inc}	$k_x^{(1)}/k_o$	κ/k_0
p polarization		
11.976°	1.5408	1.5496
24.364°	1.7459	1.7553
40.130°	1.9779	1.9822
60.388°	2.2027	2.2034
s polarization		
12.264°	1.5458	1.5560
25.594°	1.7653	1.7735
41.333°	1.9938	1.9966
64.325°	2.2346	2.2144

thickness d_1 of the rugate filter; however, this A_p-peak was found to be independent for $d_1 > 10\Omega$. The slight dependence of this A_p-peak on low values of d_1 is due to the fact that the Tamm wave possibly excited is not strongly localized to the plane $z = d_1$ in the rugate filter.

In Fig. 4.3, four A_s-peaks at $\theta_{inc} \in \{12.264, 25.594, 41.333, 64.325\}$ deg are independent of d_1 for sufficiently large d_1. Again, in Table 4.1 the relative wavenumber $k_x^{(1)}/k_0$ of the Floquet harmonic of order $n = 1$ agrees very well with a value of κ/k_0 predicted by the canonical boundary-value problem, for each of these four values of θ_{inc}.

To rule out the possibility that the absorptance peaks identified in Figs. 4.2 and 4.3 represent the propagation of waveguide modes in the bulk of the homogeneous partnering material [105], both A_p and A_s were computed as functions of θ_{inc} for $n'_d = 1.515$, $L_g = 50$ nm, $d_1 = 6\Omega$, and $L_d \in \{\lambda_0, 2\lambda_0, 3\lambda_0\}$. Plots are provided in Figs. 4.4 and 4.5. The angular locations of the four A_p-peaks at $\theta_{inc} \in \{11.976, 24.364, 40.130, 60.388\}$ deg in Fig. 4.4 are independent of the value of L_d for sufficiently high L_d. The angular locations of these peaks are also very similar to those found in Fig. 4.2.

Similarly, four A_s-peaks are identified in Fig. 4.5 at $\theta_{inc} \in \{12.216, 25.598, 41.332, 64.297\}$ deg. These peaks are very weakly dependent on the value of L_d. The A_s peaks located at $\theta_{inc} \in \{25.598, 41.332\}$ deg are very close to their counterparts in Fig. 4.3, while the ones located at $\theta_{inc} \in \{12.216, 64.297\}$ deg are slightly displaced from the angular locations of their counterparts in Fig. 4.3. I conclude that all eight absorptance peaks are indeed indicative of the excitation of

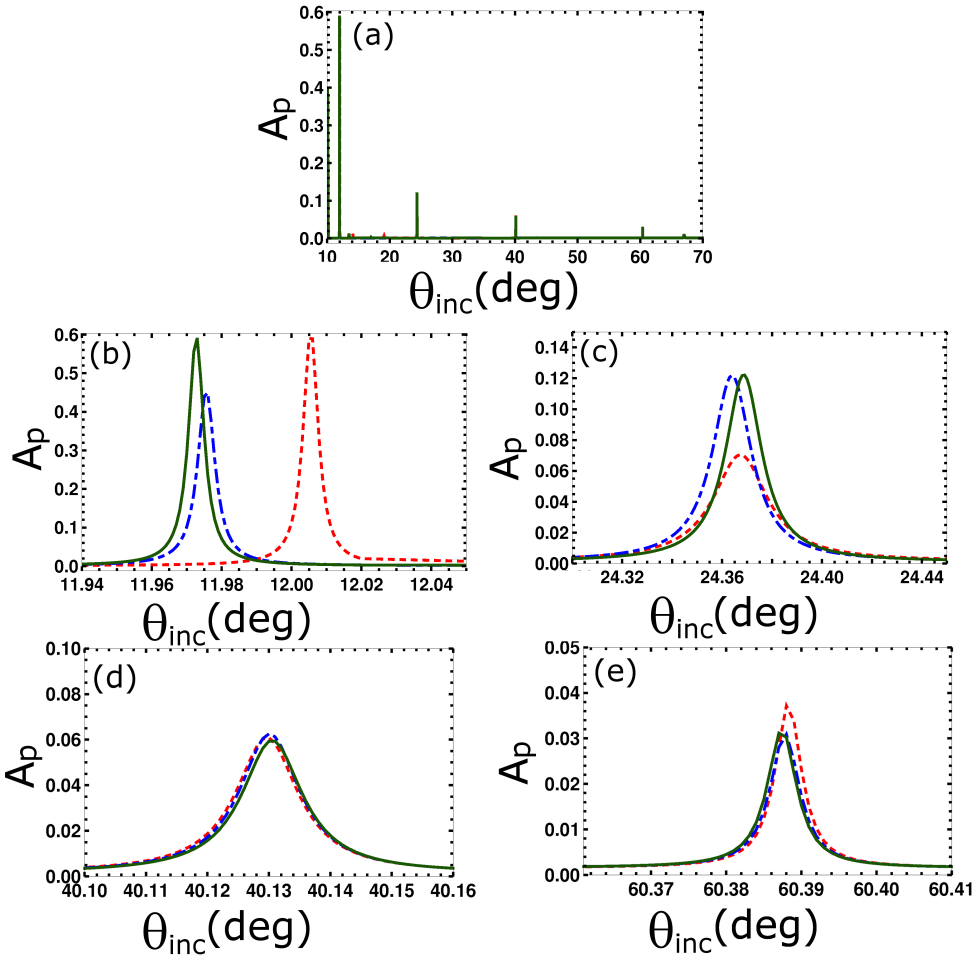

Figure 4.2: Absorptance A_p vs. the incidence angle θ_{inc} when $\lambda_0 = 633$ nm, $n_a = 1.45$, $n_b = 2.32$, $n_d = 1.515(1 + i\delta)$, $\delta = 10^{-4}$, $\Omega = \lambda_0$, $L_d = \lambda_0$, and $L_g = 50$ nm. The red dashed lines are for $d_1 = 4\Omega$, the blue chain-dashed lines for $d_1 = 6\Omega$, and the solid green lines for $d_1 = 8\Omega$. Panel (a) shows the plots of A_p over a wider angular domain, and panels (b)-(e) show the parts of the plots in panel (a) around the peaks that represent the excitation of p-polarized Tamm waves.

Tamm waves.

4.5.3 Localization of Tamm waves

The localization of the Tamm waves identified through these eight absorptance peaks in Sec. 4.5.2 was investigated by examining the spatial variation of the x-component of time-averaged Poynting

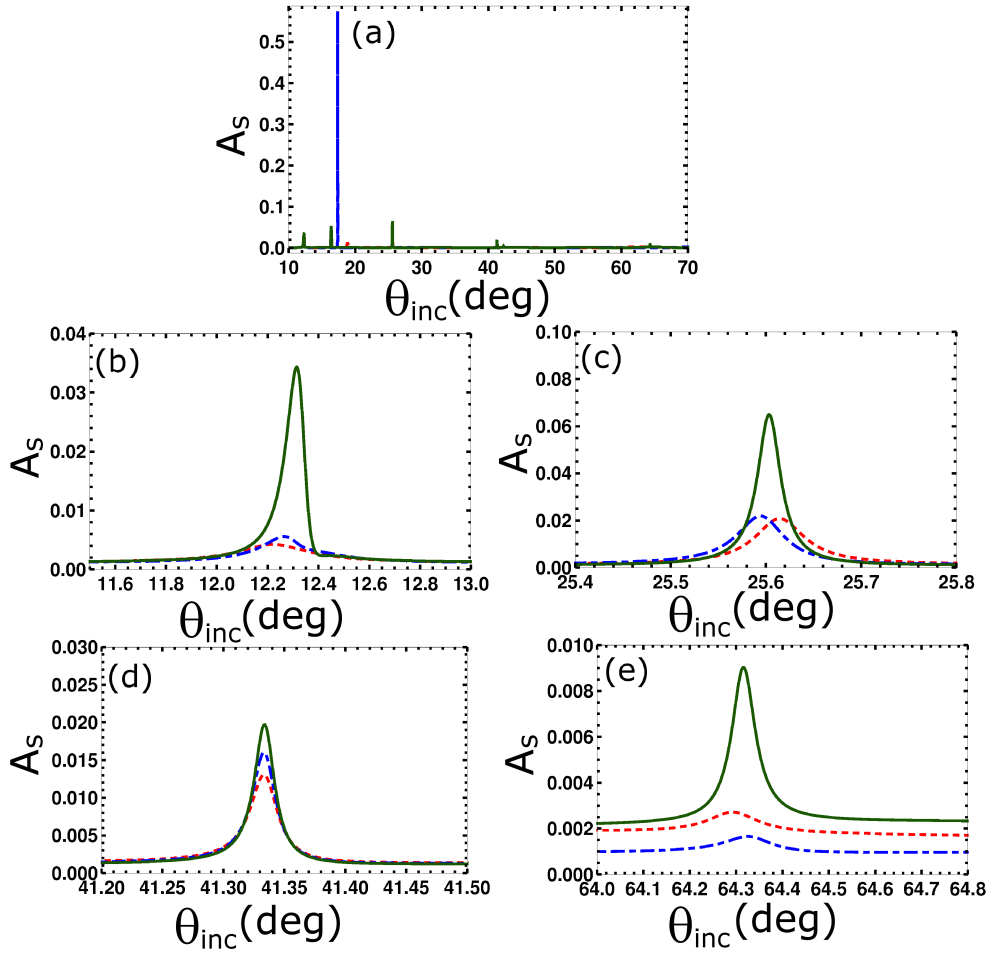

Figure 4.3: Same as Fig. 4.2, except that A_s is plotted vs. θ_{inc}.

vector

$$\mathbf{P}(x,z) = \frac{1}{2}\,\mathrm{Re}\left[\mathbf{E}(x,z)\times\mathbf{H}^{*}(x,z)\right]\,. \tag{4.25}$$

Figure 4.6(a) shows the spatial variation of $P_x(x,z)$ when $x = 3L/4$, $n_d' = 1.515$, $L_d = 2\lambda_0$, $L_g = 50$ nm, $d_1 = 6\Omega$, and $\theta_{inc} = 11.976$ deg, at which angle of incidence a Tamm wave is excited by an incident p-polarized plane wave. Clearly, the power density is maximal in the vicinity of the mean grating plane $z = (d_1 + d_2)/2$ and decays away from that region, not monotonically, but in accord with the Floquet–Lyapunov theorem [106] because of the periodicity of the matrix $[\underline{\underline{P}}(z)]$. The spatial profiles at $\theta_{inc} \in \{24.364, 40.130, 60.388\}$ deg —the angular locations of the other three A_p-peaks in Fig. 4.2 that indicate the excitation of p-polarized Tamm waves—have

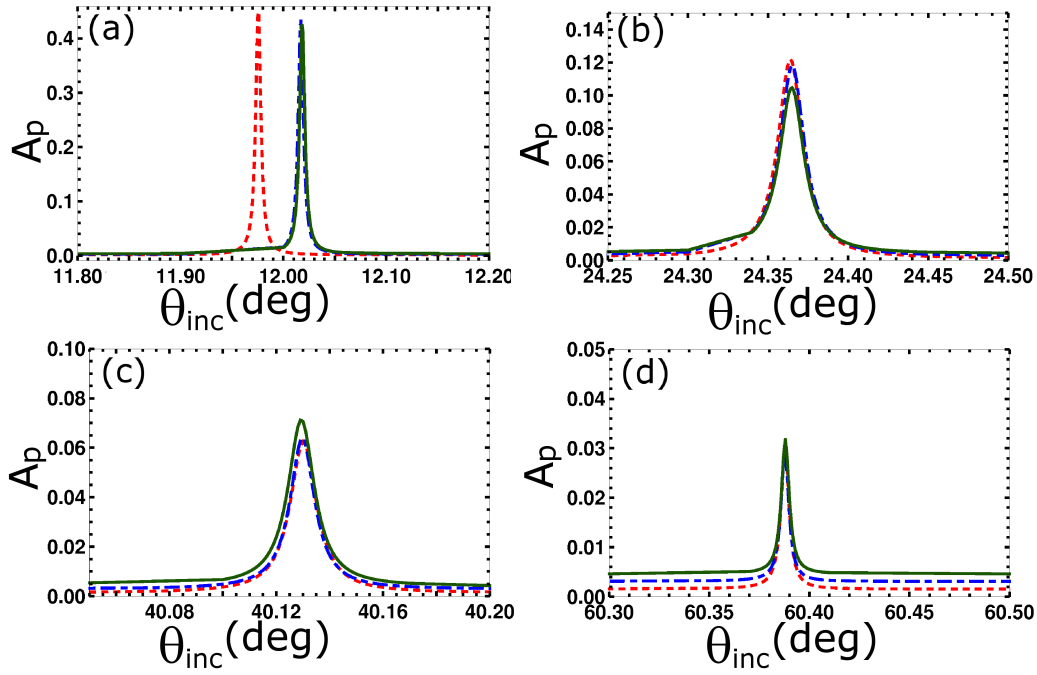

Figure 4.4: Absorptance A_p vs. the incidence angle θ_{inc} when $\lambda_0 = 633$ nm, $n_a = 1.45$, $n_b = 2.32$, $n_d = 1.515(1 + i\delta)$, $\delta = 10^{-4}$, $\Omega = \lambda_0$, $L_g = 50$ nm, and $d_1 = 6\Omega$. The red dashed lines are for $L_d = \lambda_0$, the blue chain-dashed lines for $L_d = 2\lambda_0$, and the solid green lines for $L_d = 3\lambda_0$. Only those parts of the plots are shown that have A_p-peaks representing the excitation of p-polarized Tamm waves.

the same localization characteristics as in Fig. 4.6(a).

Figure 4.6(b) shows the variation of $P_x(x, z)$ with z for the same parameters as Fig. 4.6(b) except that $\theta_{inc} = 41.335$ deg and the incident plane wave is s polarized. According to Sec. 4.5.2, an s-polarized Tamm wave is excited. Again, the power density is maximal in the vicinity of the mean grating plane $z = (d_1 + d_2)/2$ and decays away from that region in accord with the Floquet–Lyapunov theorem [106], showing localization to the mean grating plane. The spatial profiles (not shown) of $P_x(x, z)$ at the other three A_s-peaks identified in Fig. 4.3 as indicative of the excitation of s-polarized Tamm waves also exhibit similar localization.

The A_s-peak at $\theta_{inc} \simeq 17.4$ deg in Fig. 4.3 represents the excitation of a waveguide mode because the angular location is strongly dependent on the thickness d_1 of the rugate filter. This is also confirmed by the spatial variation of $P_x(x, z)$ provided in Fig. 4.6(c), because the power density is distributed in both bulk partnering materials, but does not show localization.

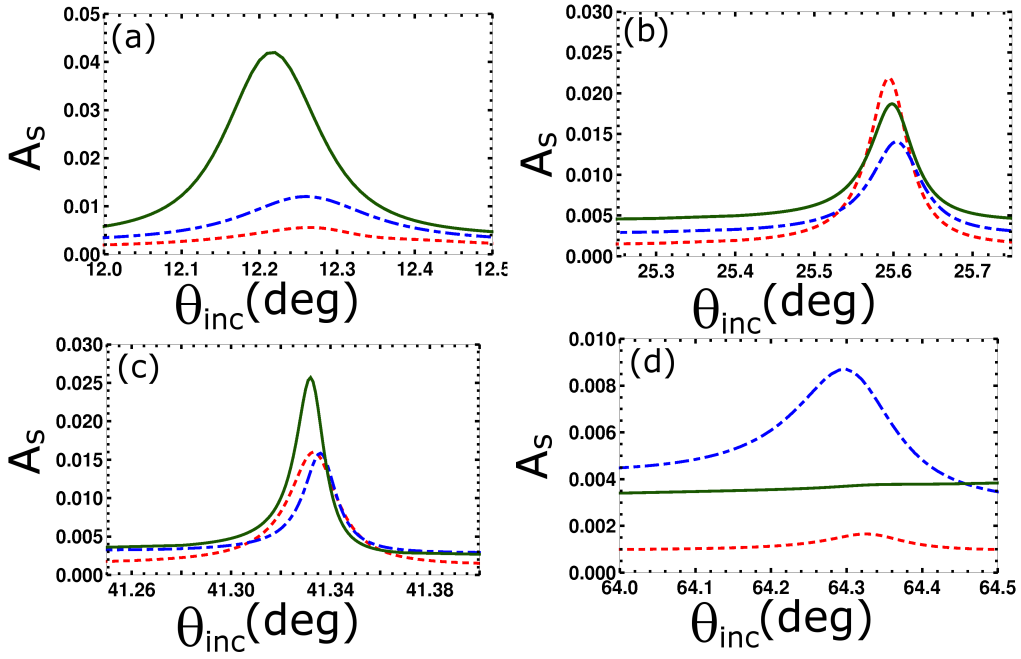

Figure 4.5: Same as Fig. 4.4, except that A_s is plotted vs. θ_{inc}.

4.5.4 Potential for sensing application

In the foregoing subsections, I have presented the plots of A_p and A_s vs. the incidence angle θ_{inc} in order to identify the absorptance peaks that represent the excitation of Tamm waves. Absorptance curves are better than reflectance or transmittance curves to identify the peaks representing the excitation of surface waves; however, in experimental research, the reflectance and transmittance data are directly measurable from which the absorptance data have to be deduced. Accordingly, I have provided the plots of total reflectance and total transmittance vs. θ_{inc} for p-polarized incidence and s-polarized incidence in Figs. 4.7 and 4.8, respectively, when $n_d = 1.515(1 + i10^{-4})$, $L_d = 2\lambda_0$, $L_g = 50$ nm, and $d_1 = 6\Omega$.

The spikes associated with the four p-polarized Tamm waves in the plots of total reflectance and total transmittance in Fig. 4.7 have magnitudes between 0.5 and 0.7 and half-widths between 0.005 deg and 0.015 deg, and the counterpart spikes in Fig. 4.8 for the four s-polarized Tamm waves possess magnitudes between 0.1 and 0.7 and half-widths between 0.02 deg and 0.2 deg. The large magnitudes of the resonant spikes should give a large signal-to-noise ratio for experimental measurements, but the narrow half-widths will result in poorly resolved peak profiles.

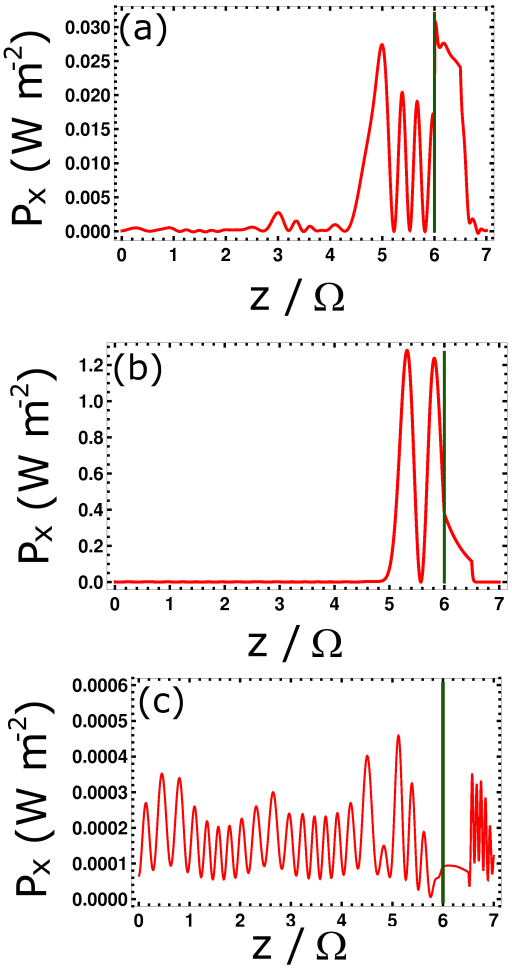

Figure 4.6: Variation of $P_x(x,z)$ when $x = 3L/4$, $\lambda_0 = 633$ nm, $n_a = 1.45$, $n_b = 2.32$, $n_d = 1.515(1 + i\delta)$, $\delta = 10^{-4}$, $\Omega = \lambda_0$, $L_d = 2\lambda_0$, $L_g = 50$ nm, and $d_1 = 6\Omega$. (a) The incident plane wave is p polarized and $\theta_{inc} = 11.976$ deg (Tamm wave). (b) The incident plane wave is s polarized and $\theta_{inc} = 41.335$ deg (Tamm wave). (c) The incident plane wave is s polarized and $\theta_{inc} = 17.381$ deg (waveguide mode). The solid green vertical line is the interface of the two partnering materials.

However, the narrowness of the spikes could be advantageous in any type of sensing application. SPP waves, a class of surface waves guided by metal/dielectric interfaces, are often used for sensing [77] because the conditions for the launch of an SPP wave shift with the refractive index of the partnering dielectric material. As with SPP waves, Tamm waves are also sensitive to changes in refractive index. From the results presented thus far, it can be deduced that the widths of spikes associated with Tamm waves are small fractions of the widths of absorptance

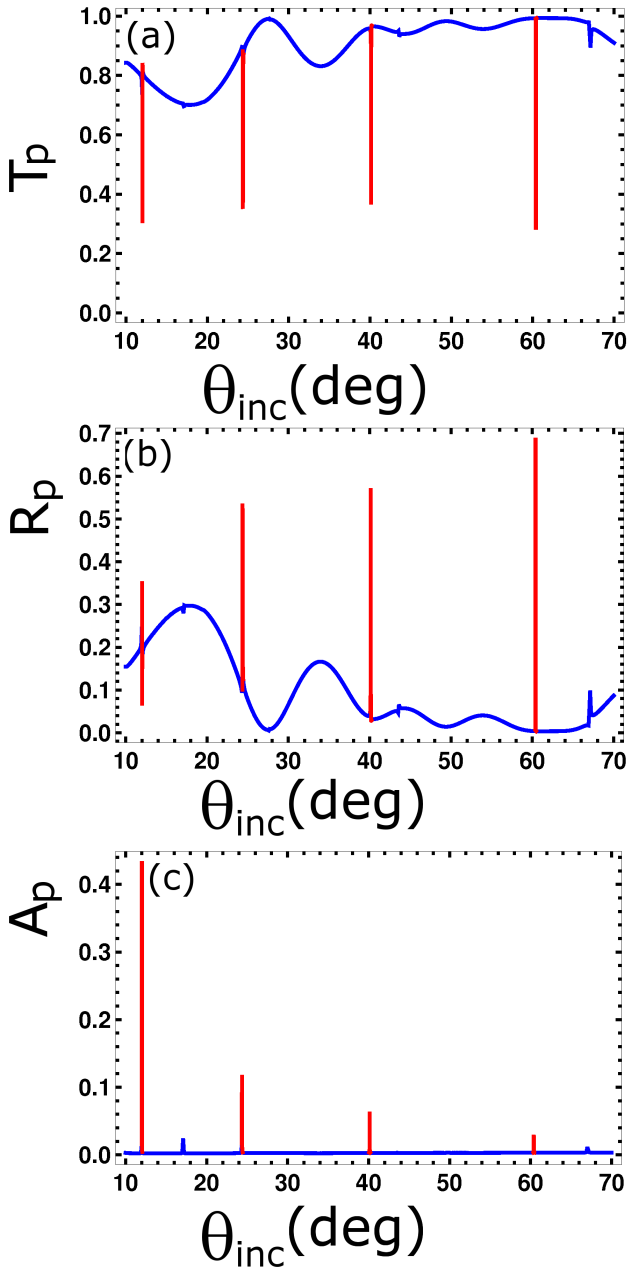

Figure 4.7: (a) Total transmittance T_p, (b) total reflectance R_p, and (c) absorptance A_p vs. θ_{inc} when $\lambda_0 = 633$ nm, $n_a = 1.45$, $n_b = 2.32$, $n_d = 1.515(1 + i\delta)$, $\delta = 10^{-4}$, $\Omega = \lambda_0$, $L_d = \lambda_0$, $L_g = 50$ nm, and $d_1 = 6\Omega$. The red spikes identify the Tamm waves.

peaks associated with SPP waves [101]. This narrowness should allow a much more precise measurement of any shift in refractive index when compared to those detected by SPP-wave-based techniques.

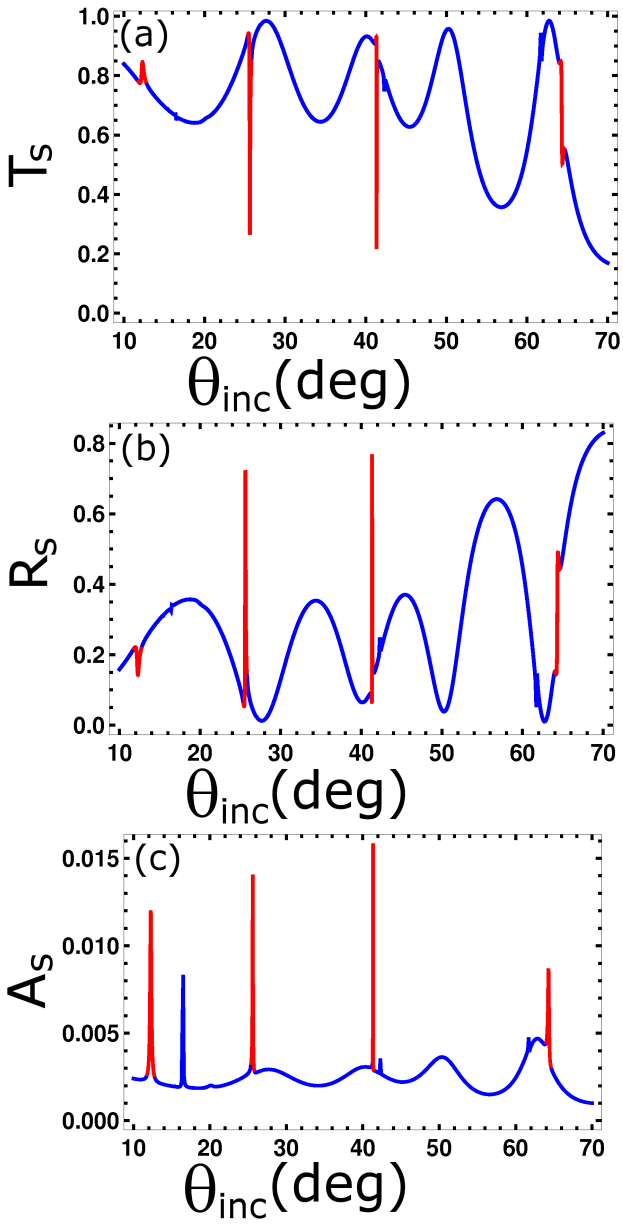

Figure 4.8: (a) Total transmittance T_s, (b) total reflectance R_s, and (c) absorptance A_s vs. θ_{inc} when $\lambda_0 = 633$ nm, $n_a = 1.45$, $n_b = 2.32$, $n_d = 1.515(1 + i\delta)$, $\delta = 10^{-4}$, $\Omega = \lambda_0$, $L_d = \lambda_0$, $L_g = 50$ nm, and $d_1 = 6\Omega$. The red spikes identify the Tamm waves.

In order to illustrate the dependence of the angular location of an absorptance peak associated with the excitation of a Tamm wave, I plotted A_p and A_s vs. θ_{inc} for $L_d = 2\lambda_0$, $L_g = 50$ nm,

$d_1 = 6\Omega$, and $n'_d \in \{1, 1.515, 1.7\}$, in Figs. 4.9 and 4.10, respectively.

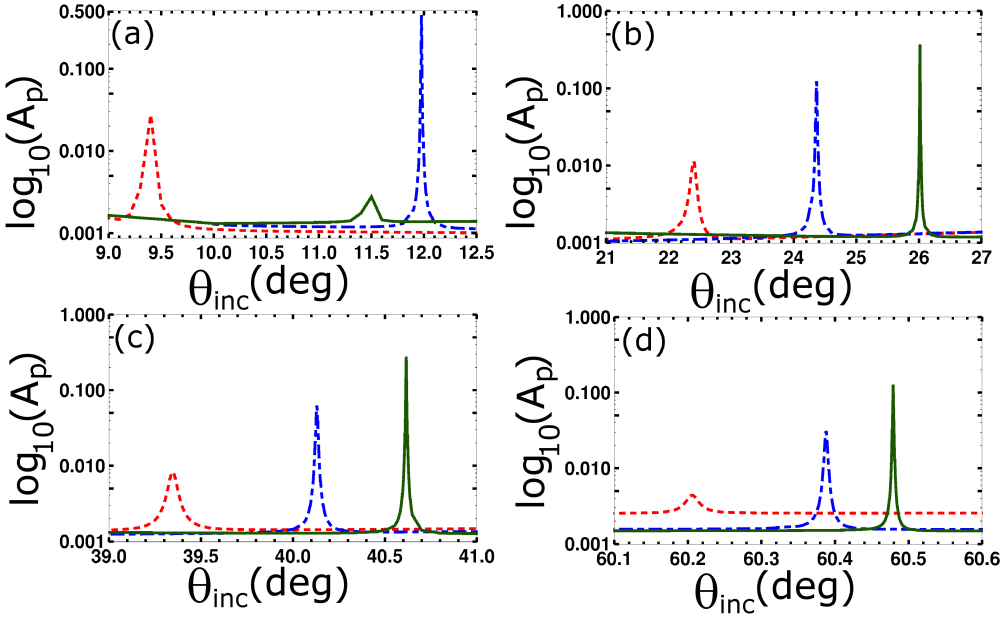

Figure 4.9: Absorptance A_p vs. the incidence angle θ_{inc} when $\lambda_0 = 633$ nm, $n_a = 1.45$, $n_b = 2.32$, $n_d = n'_d(1 + i\delta)$, $\delta = 10^{-4}$, $\Omega = \lambda_0$, $L_d = \lambda_0$, $L_g = 50$ nm, and $d_1 = 6\Omega$. The red dashed line is for $n'_d = 1$, the blue chain-dashed line for $n'_d = 1.515$, and the solid green line for $n'_d = 1.7$. Panels (a)-(d) show close ups of the plots around the A_p-peaks representing the excitation of Tamm waves.

Figure 4.9(a) shows the A_p-peaks corresponding to Tamm waves for $n'_d = 1$ and $n'_d = 1.515$. No peak can be seen for $n'_d = 1.7$, the absence being in accord with Fig. 1 of Ref. [96]. The shallow peak at $\theta_{inc} \simeq 11.5$ deg (green solid line) does not indicate the excitation of a Tamm wave as it is not predicted by the solution of the canonical boundary-value problem. From Figures 4.9(b-d) I deduce a trend of the A_p-peaks shifting to higher angular locations with increasing n'_d. In each panel, the peak for $n'_d = 1$ appears leftmost, the peak for $n'_d = 1.515$ in the middle, and the peak for $n'_d = 1.7$ appearing rightmost.

Figure 4.10 presents the same data as Fig. 4.9 except that it shows results for s polarization. Of note is Fig. 4.10(d) in which the trend of increasing angle of incidence of the A_s-peak with n'_d is bucked with the peak for $n'_d = 1.515$ appearing rightmost.

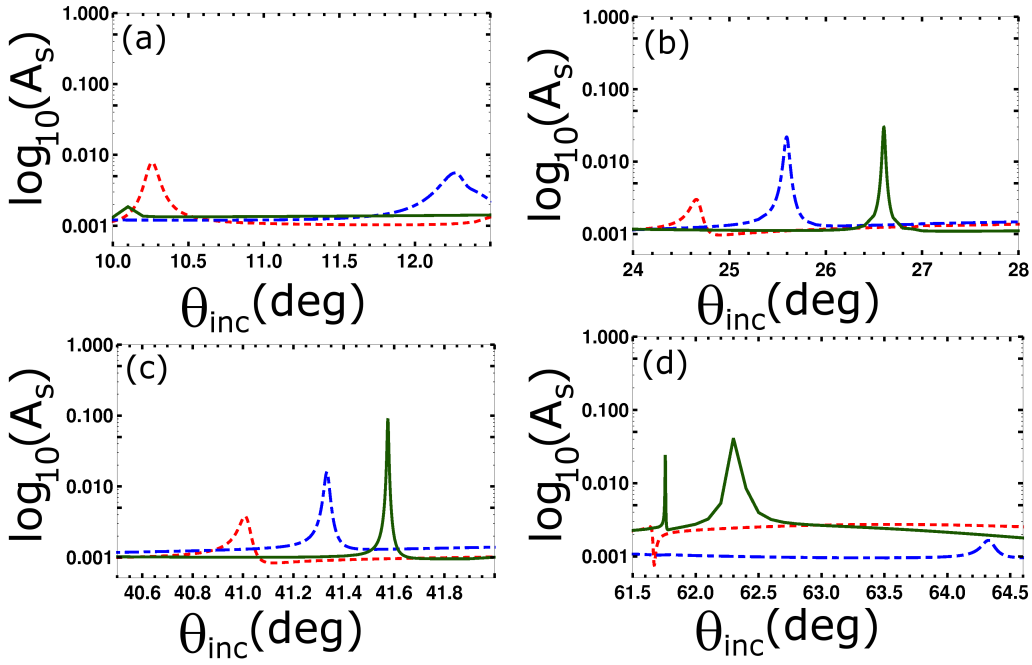

Figure 4.10: Same as Fig. 4.9, except that A_s is plotted vs. θ_{inc}.

4.5.5 Propagation Lengths of Tamm Waves

The solution of the boundary-value problem underlying the grating-coupled configuration does not yield the attenuation rate of the surface wave. The same deficiency arises with the prism-coupled configuration. Only the solution of the canonical boundary-value problem yields $1/\mathrm{Im}(\kappa)$ as the e-folding distance or the propagation length.

As $n_{a,b}$ are taken to be purely real and $n_d = 1.515$ in Sec. 4.5.1, the values of κ reported in that section for the canonical problem are purely real. If the value of n_d is changed to $1.515(1+i10^{-4})$, then, for example, one of the eight values of κ/k_0 changes from 1.9966 to $1.9966 + i9.5790 \times 10^{-7}$. If, however, the value of n_d is changed to $1.38 + i7.61$ (metal), the Tamm wave transmutes into an SPP wave with $\kappa/k_0 = 1.9836 + i6.0026 \times 10^{-4}$. Thus, whereas the phase speeds of the Tamm wave and the SPP wave are almost equal, the propagation length of the Tamm wave is more than 600× greater than that of the SPP wave. Not only would the propagation lengths of Tamm waves be advantageous for communications, they would also impart greater sensitivity to optical sensors exploiting the surface-wave phenomenon.

4.6 Concluding Remarks

I have used the results of the canonical boundary value problem for the interface of a rugate filter and a homogeneous dielectric material to identify multiple Tamm waves in the practical grating coupled problem. These waves were verified as ESWs by: showing that the power density distribution is concentrated at the rugate filter/homogeneous dielectric material interface, showing that the absorptance peaks indicative of the launch of a Tamm wave are independent of rugate-filter thickness and the homogeneous dielectric layer's thickness. I also demonstrated the dependence of the absorptance peaks' locations on the refractive index of the homogeneous dielectric material; this could give rise to sensitive optical sensors. To aid in the future experimental verification of the existence of multiple Tamm waves, I presented results of transmittance and reflectance calculations. However, as shown in Ch. 5, the Dyakonov–Tamm wave should be easier to detect than the Tamm wave and therefore easier to exploit.

Chapter 5

Prism-Coupled Excitation of the Dyakonov-Tamm Wave[‡]

Because thin films deposited by thermal evaporation are often anisotropic, thermal evaporation is better suited to producing thin films with the optical properties required to support the propagation of the Dyakonov–Tamm wave. As such, I now shift my focus away from the modeling of Tamm waves in Ch. 4 and take up the problem of the Dyakonov–Tamm wave. In Ch. 5 the preliminary modeling work required to establish a starting point for the experimental observation of the Dyakonov–Tamm wave is reported.

5.1 Chapter Summary

The Dyakonov–Tamm wave is a surface electromagnetic wave that propagates along the interface of two dielectric materials of which at least one is periodically nonhomogeneous and anisotropic. Here I investigate the effects of altering several geometric parameters of a chiral sculptured thin film which meets the periodic nonhomogeneity and anisotropy requirements; allowing it to support the propagation of a Dyakonov–Tamm wave when paired with a homogeneous isotropic material represented by a dense dielectric film. A chiral sculptured thin film is particularly well suited to this task because its morphology is easily altered through the manipulation of a few

[‡]This chapter is based on: Pulsifer, D. P., Faryad, M., and Lakhtakia, A., "Parametric investigation of prism-coupled excitation of Dyakonov–Tamm," *Journal of the Optical Society of America B* **30**, 2081–2089 (2013).

deposition parameters. The results of theoretically modeling the effects of the variation of these parameters is presented. These results should provide a foundation from which experimental observation of Dyakonov–Tamm waves can be made.

5.2 Introduction

Dyakonov–Tamm waves propagate guided by the interface of two dielectric materials, one of which must be periodically nonhomogeneous and anisotropic [92, 93]. The existence of the Dyakonov–Tamm wave [47] was predicted in 2007 by Polo and Lakhtakia when the anisotropic material properties that allow for Dyakonov waves, and the periodically nonhomogeneous material properties that support Tamm waves [89] were considered in combination. As with other surface waves [76], Dyakonov–Tamm waves are highly sensitive to the optical properties of the material found near the interface, and could find applications in optical sensing, waveguiding, and integrated optics [93].

Owing to the periodic nonhomogeneity of the anisotropic dielectric material, Dyakonov–Tamm waves can exhibit a 360 deg angular existence domain [47, 101, 107] just like Tamm waves. The angular existence domain is the range of angles in the xy plain in which the propagation of an electromagnetic surface wave is allowed to propagate. A chiral sculptured thin film (chiral STF) is an anisotropic periodically nonhomogeneous dielectric material, constituted of a collection of parallel nanowires all of which have a helicoidal shape which is oriented along the z axis [31]. This morphology is obtained by orienting a substrate at an oblique angle in relation to a directional vapor flux while simultaneously rotating the substrate about its surface normal. By controlling the substrate's motion and the film's deposition rate, the morphology of the chiral STF can be controlled [31]. In this way, the inclination angle χ and pitch 2Ω can be directly controlled while the film's porosity and degree of bianisotropy can be indirectly altered for a given material. This level of control makes chiral STFs particularly well suited for use in designing an interface which will support Dyakonov–Tamm waves.

A chiral STF can be partnered with a homogeneous isotropic dielectric material in a canonical boundary-value problem wherein, each material is made to occupy each half space, and the propagation of the Dyakonov–Tamm wave is investigated by solving the dispersion equation for propagation in the x-direction at the interface of the materials [47, 107].

Because the canonical problem is impossible to implement experimentally, I also investigated the case where the partnering materials are of a finite thickness in a prism-coupled configuration. This prism-coupled configuration has been used for the experimental verification of both Dyakonov [94] and Tamm [97] waves due to its ease of implementation.

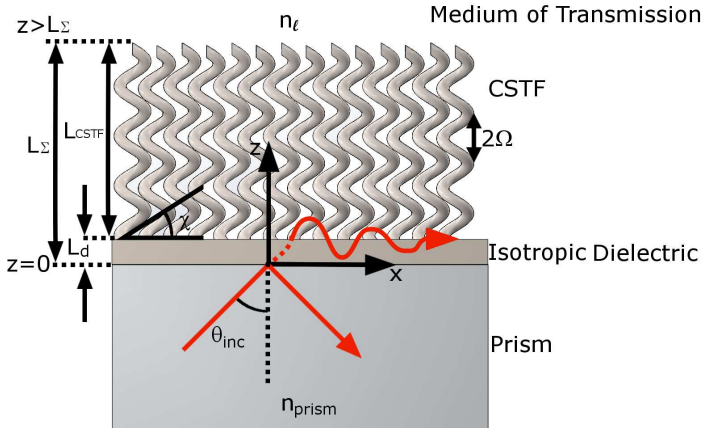

Figure 5.1: Schematic of the prism-coupled configuration. The half-space $z < 0$ is occupied by the prism material and the half-space $z > L_\Sigma$ is occupied by another homogeneous isotropic material, both assumed to have negligible dissipation.

The plan of this chapter is as follows: In Sec. 5.3, brief outlines of the theory of the prism-coupled configuration and an underlying canonical boundary-value problem for Dyakonov–Tamm-wave propagation are provided. Numerical results of a parametric investigation are presented and discussed in Sec. 5.4, followed by concluding remarks in Sec. 5.5. An $\exp(-i\omega t)$ dependence on time t is implicit, with ω denoting the angular frequency and $i = \sqrt{-1}$. The free-space wavenumber and the free-space wavelength are denoted by $k_0 = \omega\sqrt{\epsilon_0\mu_0}$ and $\lambda_0 = 2\pi/k_0$, respectively, with μ_0 being the permeability and ϵ_0 the permittivity of free space (i.e., vacuum). Vectors are in boldface, and the Cartesian unit vectors are identified as $\mathbf{u}_x$, $\mathbf{u}_y$, and $\mathbf{u}_z$.

5.3 Theoretical Preliminaries

5.3.1 Prism-coupled configuration

Let the half-space $z > L_\Sigma$ be occupied by another homogeneous and isotropic dielectric material with relative permittivity $\epsilon_\ell = n_\ell^2 > 0$, as is shown schematically in Fig. 5.1. Let the half-space

$z < 0$, representing a prism, be occupied by a homogeneous and isotropic dielectric material with relative permittivity $\epsilon_{prism} = n_{prism}^2 > 0$. Both materials are supposed to have negligible dissipation at the frequency of interest, so that n_{prism} and n_ℓ are real and positive.

First the homogeneous partnering material and then the chiral STF are supposed to have been deposited on a substrate that has the same refractive index as the prism material. Therefore, in a theoretical study, we can take the region between the two half-spaces to be occupied by the partnering materials. The region $0 < z < L_d$ is occupied by a homogeneous, isotropic, dielectric material with relative permittivity $\epsilon_d = n_d^2$. The region $L_d < z < L_d + L_{CSTF} = L_\Sigma$ is occupied by a chiral STF whose permittivity dyadic [31]

$$\underline{\underline{\epsilon}}_{CSTF}(z,\omega) = \epsilon_0 \, \underline{\underline{S}}_z(\zeta) \cdot \underline{\underline{S}}_y \cdot \underline{\underline{\epsilon}}^{\circ}_{ref}(\omega) \cdot \underline{\underline{S}}_y^{-1} \cdot \underline{\underline{S}}_z^{-1}(\zeta) \tag{5.1}$$

depends on the dyadics

$$\left.\begin{aligned} \underline{\underline{S}}_z(\zeta) &= (\mathbf{u}_x\mathbf{u}_x + \mathbf{u}_y\mathbf{u}_y)\cos(h\pi\zeta/\Omega) + (\mathbf{u}_y\mathbf{u}_x - \mathbf{u}_x\mathbf{u}_y)\sin(h\pi\zeta/\Omega) + \mathbf{u}_z\mathbf{u}_z \\ \underline{\underline{S}}_y &= (\mathbf{u}_x\mathbf{u}_x + \mathbf{u}_z\mathbf{u}_z)\cos\chi + (\mathbf{u}_z\mathbf{u}_x - \mathbf{u}_x\mathbf{u}_z)\sin\chi + \mathbf{u}_y\mathbf{u}_y \\ \underline{\underline{\epsilon}}^{\circ}_{ref}(\omega) &= \epsilon_a(\omega)\,\mathbf{u}_z\mathbf{u}_z + \epsilon_b(\omega)\,\mathbf{u}_x\mathbf{u}_x + \epsilon_c(\omega)\,\mathbf{u}_y\mathbf{u}_y \end{aligned}\right\}, \tag{5.2}$$

where $\zeta = z + \gamma\Omega/\pi$ and γ is an offset angle for generality of the direction of surface-wave propagation.

The principal relative permittivity scalars ϵ_a, ϵ_b, and ϵ_c of the chiral STF are functions of the angular frequency. The helicoidal variation of the permittivity dyadic of the chiral STF is offset in the plane $z = 0$ relative to the x axis by the angle $h\gamma$. The structural handedness parameter $h = 1$ for right-handedness but $h = -1$ for left-handedness. After defining the ratio

$$N_p = L_{CSTF}/2\Omega\,, \tag{5.3}$$

let me note that usually $N_p \in \{1, 2, 3, ...\}$ in theoretical research on chiral STFs. However, non-integer values of N_p are considered in Sec. 5.4.1 because of a significant effect on the propagation of Dyakonov–Tamm waves.

Let an arbitrarily polarized plane wave, propagating in the half-space $z \leq 0$ with its wave vector lying wholly in the xz plane and making an angle $\theta_{inc} \in [0, 90)$ deg with respect to the

z axis, be incident on the homogeneous partnering material. The incident and reflected electric field phasors are respectively represented as

$$\begin{aligned}\mathbf{E}_{inc}(\mathbf{r}) &= [a_s\mathbf{u}_y + a_p\,(-\mathbf{u}_x\cos\theta_{inc} + \mathbf{u}_z\sin\theta_{inc})] \\ &\quad \times \exp\left[ik_0 n_{prism}\,(\mathbf{u}_x\sin\theta_{inc} + \mathbf{u}_z\cos\theta_{inc})\ \bullet\ \mathbf{r}\right]\,, \quad z \le 0\,, \end{aligned} \tag{5.4}$$

and

$$\begin{aligned}\mathbf{E}_{ref}(\mathbf{r}) &= [r_s\mathbf{u}_y + r_p\,(\mathbf{u}_x\cos\theta_{inc} + \mathbf{u}_z\sin\theta_{inc})] \\ &\quad \times \exp\left[ik_0 n_{prism}\,(\mathbf{u}_x\sin\theta_{inc} - \mathbf{u}_z\cos\theta_{inc})\ \bullet\ \mathbf{r}\right]\,, \quad z \le 0\,. \end{aligned} \tag{5.5}$$

Here and hereafter, a_p and a_s are the amplitudes of the p- and s-polarized components of the incident plane wave; r_p and r_s are the amplitudes of the p- and s-polarized components of the reflected plane wave; and $\mathbf{r} = \mathbf{u}_x x + \mathbf{u}_y y + \mathbf{u}_z z$ is the position vector.

The transmitted electric field phasor is written as

$$\begin{aligned}\mathbf{E}_{tr}(\mathbf{r}) &= [t_s\mathbf{u}_y + t_p\,(-\mathbf{u}_x\cos\theta_{tr} + \mathbf{u}_z\sin\theta_{tr})] \\ &\quad \times \exp\left[ik_0\,(\mathbf{u}_x n_{prism}\sin\theta_{inc} + \mathbf{u}_z n_\ell\cos\theta_{tr})\ \bullet\ (\mathbf{r} - \mathbf{u}_z L_\Sigma)\right]\,, \\ &\quad z \ge L_\Sigma\,. \end{aligned} \tag{5.6}$$

According to the law of Ibn Sahl [108],

$$n_{prism}\sin\theta_{inc} = n_\ell\sin\theta_{tr}\,. \tag{5.7}$$

Whereas θ_{inc} is a real angle, θ_{tr} can be a complex angle if $n_\ell < n_{prism}$.

The procedure to determine the reflection amplitudes r_s and r_p as well as the transmission amplitudes t_s and t_p in terms of the amplitudes a_s and a_p of the incident plane wave is well known and has been explained elsewhere [109]. After determining the reflection and transmission

amplitudes, the reflectances

$$\left.\begin{array}{ll} R_{ss} = |r_s/a_s|^2\Big|_{a_p=0}, & R_{ps} = |r_p/a_s|^2\Big|_{a_p=0} \\ R_{pp} = |r_p/a_p|^2\Big|_{a_s=0}, & R_{sp} = |r_s/a_p|^2\Big|_{a_s=0} \end{array}\right\}, \tag{5.8}$$

and transmittances

$$\left.\begin{array}{ll} T_{ss} = \upsilon|t_s/a_s|^2\Big|_{a_p=0}, & T_{ps} = \upsilon|t_p/a_s|^2\Big|_{a_p=0} \\ T_{pp} = \upsilon|t_p/a_p|^2\Big|_{a_s=0}, & T_{sp} = \upsilon|t_s/a_p|^2\Big|_{a_s=0} \end{array}\right\}, \tag{5.9}$$

can be calculated, with $\upsilon = (n_\ell/n_{prism})\,\mathrm{Re}\,(\cos\theta_{tr})\,/\cos\theta_{inc}$. The absorptances for s- and p-polarized incidence conditions can thereafter be calculated, respectively, as

$$A_s = 1 - (R_{ss} + R_{ps} + T_{ss} + T_{ps}) \tag{5.10}$$

and

$$A_p = 1 - (R_{pp} + R_{sp} + T_{pp} + T_{sp})\ . \tag{5.11}$$

Each absorptance has zero as its lower bound and unity as its upper bound, because all materials involved are passive.

The excitation of a Dyakonov–Tamm wave in the prism-coupled configuration is identified after plotting the absorptances as functions of the angle of incidence. These plots contain several peaks. If the location of a peak on the θ_{inc}-axis is independent of the thicknesses of both partnering materials (beyond threshold values) as well as of the polarization state of the linearly polarized incident plane wave, then that peak indicates the excitation of a Dyakonov–Tamm wave. The angular location of such a peak is indicated by θ_{inc}^{DT}. Further confirmation is sought from the solution of an underlying canonical boundary-value problem [47, 110].

5.3.2 Canonical Boundary-Value Problem

In the canonical boundary-value problem underlying the prism-coupled configuration, neither of the two partnering materials is of finite thickness but occupies a half space instead, as shown schematically in Fig. 5.2. Let the chiral STF fill the half-space $z > 0$, while the half-space

$z < 0$ is filled by the homogeneous and isotropic partnering material. Furthermore, let the Dyakonov–Tamm wave propagate along the x axis in the xy plane with its field phasors having an $\exp(i\kappa x)$ dependence on x and none on y, the dependence of the field phasors on z being initially undetermined. The complete formulation available elsewhere [47] yields a dispersion equation that must be satisfied by the relative wavenumber κ/k_0 of the Dyakonov–Tamm wave. This dispersion equation can be solved numerically for κ/k_0, using a combination of the search and the Newton–Raphson methods [111].

Usually, both partnering materials are taken to have very small dissipation. The solution of the canonical problem for the selected duo of partnering materials then yields

$$\theta_C = \sin^{-1}\left[\mathrm{Re}\left(\kappa\right)/k_0 n_{prism}\right] \tag{5.12}$$

as a prediction of the angle of incidence θ_{inc}^{DT} for which a Dyakonov–Tamm wave should be excited in the prism-coupled configuration.

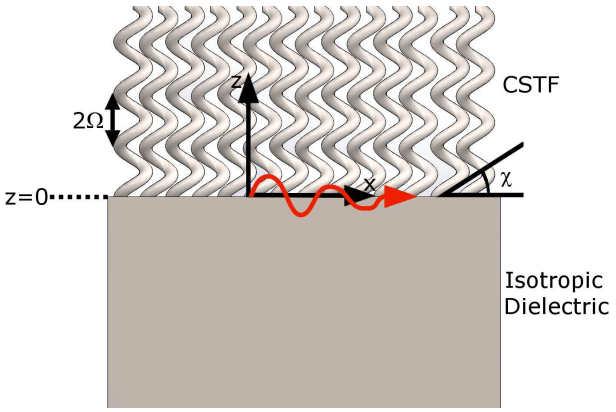

Figure 5.2: Schematic of the canonical problem. Both partnering materials are taken to occupy half spaces.

5.4 Numerical Results and Discussion

For all numerical results presented here, the free-space wavelength was fixed at $\lambda_0 = 633$ nm. The homogeneous partnering material was taken to have a refractive index $n_d = 1.377\left(1 + i10^{-4}\right)$. I also fixed $n_{prism} = 1.779$ (SF11 glass) and $n_\ell = 1$ (air).

The chiral STF was chosen to obey the relationships

$$\left.\begin{aligned}
\epsilon_a &= m\left[1.0443 + 2.7394\left(\tfrac{2\chi_v}{\pi}\right) - 1.3697\left(\tfrac{2\chi_v}{\pi}\right)^2\right]^2 \\
\epsilon_b &= m\left[1.6765 + 1.5649\left(\tfrac{2\chi_v}{\pi}\right) - 0.7825\left(\tfrac{2\chi_v}{\pi}\right)\right]^2 \\
\epsilon_c &= m\left[1.3586 + 2.1109\left(\tfrac{2\chi_v}{\pi}\right) - 1.0554\left(\tfrac{2\chi_v}{\pi}\right)^2\right]^2 \\
\chi &= \tan^{-1}\left(2.8818\tan\chi_v\right)
\end{aligned}\right\} \tag{5.13}$$

in terms of the angle $\chi_v \in (0, \pi/2]$ made by the average direction of the collimated vapor flux with respect to the plane of the substrate during thermal evaporation. When $m = 1$, the foregoing relations describe columnar thin films made by Hodgkinson *et al.* [112] from the evaporation of patinal titanium oxide. In the absence of constitutive data on actual chiral STFs, I have taken Eqs. (5.13) to apply to a chiral STF simply for illustration. Unless otherwise mentioned, $\Omega = 150$ nm, $\chi_v = 20$ deg, $N_p = 6$, $m = 1$, $h = 1$, $\gamma = 45$ deg, and $L_d = 300$ nm in the remainder of this section.

In each of the following subsections, the effect of one descriptive parameter of the chiral STF is discussed while keeping the other parameters fixed.

5.4.1 Effect of N_p

The excitation of Dyakonov–Tamm waves in the prism-coupled configuration has to be ascertained by plotting the absorptances A_p and A_s as functions of the incidence angle θ_{inc}. The excitation of a Dyakonov–Tamm wave is indicated by an absorptance peak whose location on the θ_{inc}-axis is independent of the thicknesses of both partnering materials, given that each is greater than some threshold value that is required for the Dyakonov–Tamm wave to develop well. Additionally, the angular location must not depend on the polarization state of the incident plane wave. Finally, for confirmation the angular location of the peak has to be compared with the prediction θ_C.

Figure 5.3 shows plots of A_p and A_s computed as functions of θ_{inc}, when $\Omega = 150$ nm, $\chi_v = 20$ deg, $m = 1$, $h = 1$, $\gamma = 45$ deg, $L_d = 300$ nm, and $N_p \in \{5, 6, 7\}$. An absorption peak located at $\theta_{inc}^{DT} \in \{59.0, 58.8, 58.7\}$ deg for $N_p \in \{5, 6, 7\}$ was identified as indicative of the excitation of a Dyakonov–Tamm wave. Confirmation was found from comparison to the solution $\theta_C = 58.6$ deg of the underlying canonical problem, and a further increase of N_p to 10 in steps of unity showed

that θ_{inc}^{DT} indeed converged to θ_C. This result for the prism-coupled configuration was found to be nearly independent of the thickness $L_d \in [150, 1000]$ nm of the homogeneous partnering material.

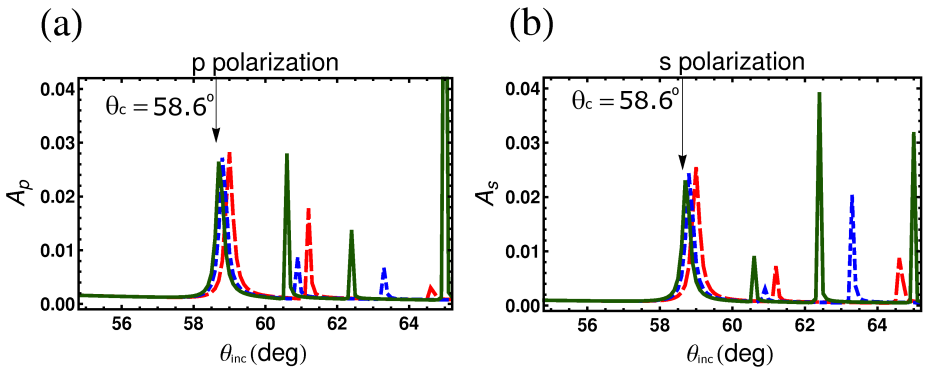

Figure 5.3: Absorptances (a) A_p and (b) A_s as functions of θ_{inc} in the prism-coupled configuration when $\Omega = 150$ nm, $\chi_v = 20$ deg, $m = 1$, $h = 1$, and $\gamma = 45$ deg; $n_d = 1.377\left(1 + i10^{-4}\right)$ and $L_d = 300$ nm; $n_{prism} = 1.779$; and $n_\ell = 1$. The red dashed, blue dot-dashed, and green solid lines, respectively, represent the absorptances when $N_p = 5$, 6, and 7. A black arrow indicates the location of θ_C predicted by the solution of the canonical configuration.

Additional confirmation was sought by examining the variations of the magnitudes of the Cartesian components of the electric field phasor with respect to z, in the prism-coupled configuration. For this purpose, I set $L_d = 2\Omega$, $N_p = 6$, $a_p = 1$, and $a_s = 0$. Figure 5.4(a) clearly shows that all components of the electric field phasor decay away from the interface $z = L_d$, when $\theta_{inc} = 58.8$ deg. The decay on the chiral STF side of the interface has an oscillatory pattern, which is in conformality with the Floquet theory for ordinary differential equations with periodic coefficients [106]. Parenthetically, the much higher values of the magnitudes of the electric-field components in Fig. 5.4(a) in comparison to the unit magnitude of the incident electric field are coupled with extremely low values of the magnitudes of the magnetic-field components, and the principle of conservation of energy is not violated.

In contrast to Fig. 5.4(a), the field phasors in Fig. 5.4(b) for $\theta_{inc} = 60.8$ deg do not decay away from the interface on the chiral STF side of the interface. As an absorptance peak is present in the plot of A_p against θ_{inc} in Fig. 5.3(a), this peak denotes the excitation of a waveguide mode which is strongly dependent on the thicknesses of both partnering materials [105, 113].

The foregoing results suggest that the use of a chiral STF with $N_p \geq 6$ would be sufficient

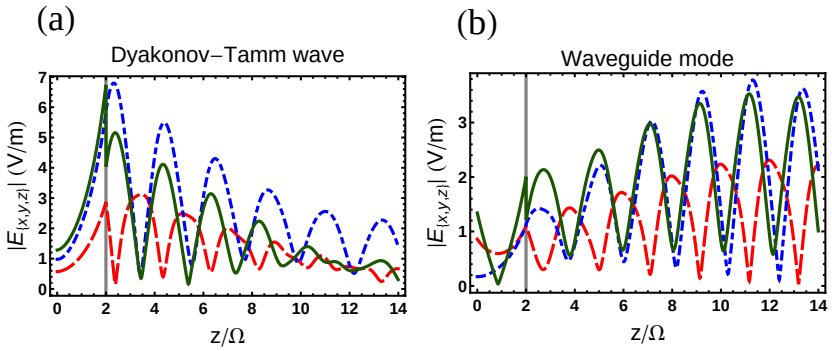

Figure 5.4: Variations of the magnitudes of the Cartesian components of the electric field phasor along the z axis for (a) a Dyakonov–Tamm wave and (b) a waveguide mode excited in the prism-coupled configuration. Geometric and constitutive parameters are the same as in Fig. 5.3, except that $L_d = 2\Omega$ and $N_p = 6$. The red dashed, the blue dot-dashed, and the solid green lines, respectively, represent the x-, y- and z-directed components. The vertical gray line represents the interface $z = L_d$ of the partnering materials. The incident plane wave is p-polarized ($a_p = 1,\ a_s = 0$). (a) $\theta_{inc} = \theta_{inc}^{DT} = 58.8$ deg and (b) $\theta_{inc} = 60.8$ deg.

for the experimental observation of a well-formed Dyakonov–Tamm wave in the prism-coupled configuration.

So far, the ratio $N_p = L_{CSTF}/2\Omega$ has been an integer, as indeed is commonplace in the literature on the optical response characteristics of chiral STFs. However, the issue of partial periods is of practical importance as slight variations in the final thickness of the chiral STF could result in otherwise unexplained shifts in the observation of absorptance peaks associated with the launch of a Dyakonov–Tamm wave. Because both partnering materials occupy half spaces in the underlying canonical problem, it naturally is unable to account for the effects of non-integer values of N_p.

Setting $N_p \in \{6.0, 6.1, 6.2, 6.3, 6.4, 6.5\}$, I computed the absorptances A_p and A_s as functions of θ_{inc}, when $\Omega = 150$ nm, $\chi_v = 20$ deg, $m = 1$, $h = 1$, $\gamma = 45$ deg, and $L_d = 300$ nm. The computed data are plotted in Fig. 5.5, wherein absorptance peaks indicative of the Dyakonov–Tamm-wave phenomenon are observed at $\theta_{inc}^{DT} \in \{58.8, 58.9, 59.0, 59.2, 58.4, 58.7\}$ deg. Accordingly, the angular location of a Dyakonov–Tamm wave periodically deviates from θ_C, as N_p increases from

a sufficiently large integer to the next. As a result of this periodic shift in the angular location of a Dyakonov–Tamm wave, care must be taken in any effort to experimentally observe the Dyakonov–Tamm wave to ensure that N_p is an integer. Failure to do so could complicate the effort by introducing otherwise unexplained shifts in the angular location of absorptance peaks suspected to correspond to the launch of a Dyakonov–Tamm wave.

5.4.2 Effect of Ω

The structural period 2Ω of a chiral STF can be varied in experiments by altering either the deposition rate or the substrate rotation speed or both [31]. As Ω describes the rate of spatial variation of the dielectric properties of the chiral STF along the z axis, variation in its value is expected to affect the expected angular location of a Dyakonov–Tamm wave in the prism-coupled configuration. In order to investigate this issue, the value of 2Ω was varied between 300 and 450 nm in 50 nm steps, when $\chi_v = 20$ deg, $N_p = 6$, $m = 1$, $h = 1$, $\gamma = 45$ deg, and $L_d = 300$ nm. The plots of A_p and A_s aginst θ_{inc} are shown in Fig. 5.6. For $2\Omega \in \{300, 350, 400, 450\}$ nm, the canonical problem yielded $\theta_C \in \{58.6, 64.2, 68.2, 71.4\}$ deg; in the prism-coupled configuration, corresponding absorptance peaks were found at $\theta_{inc}^{DT} \in \{58.8, 64.2, 68.2, 71.4\}$ deg. These results suggests that increasing 2Ω will increase the angle of incidence at which the Dyakonov–Tamm wave will be excited in the prism-coupled configuration.

The dependence of θ_{inc}^{DT} on Ω can be advantageous for experimental observation of Dyakonov–Tamm waves. The angular location of the Dyakonov-Tamm wave must fall within a θ_{inc}-range for which data can be collected experimentally. Because the structural period of the chiral STF can be easily set during deposition, this parameter must be properly chosen to control the angular location at which the Dyakonov–Tamm wave is excited.

5.4.3 Effect of χ_v

The vapor flux angle χ_v can be set experimentally by either appropriately tilting the stage to which the substrate is affixed or appropriately orienting the vapor source relative to a substrate whose position and orientation are fixed [31]. Manipulation of χ_v results in changes in χ as well as the three eigenvalues ϵ_a, ϵ_b, and ϵ_c of $\underline{\underline{\epsilon}}_{CSTF}$. Typically, $\chi > \chi_v$ for $\chi_v < 90$ deg. As χ_v nears 90 deg, the difference between the two angles lessens; when $\chi_v = 90$ deg, so is χ. Likewise, the

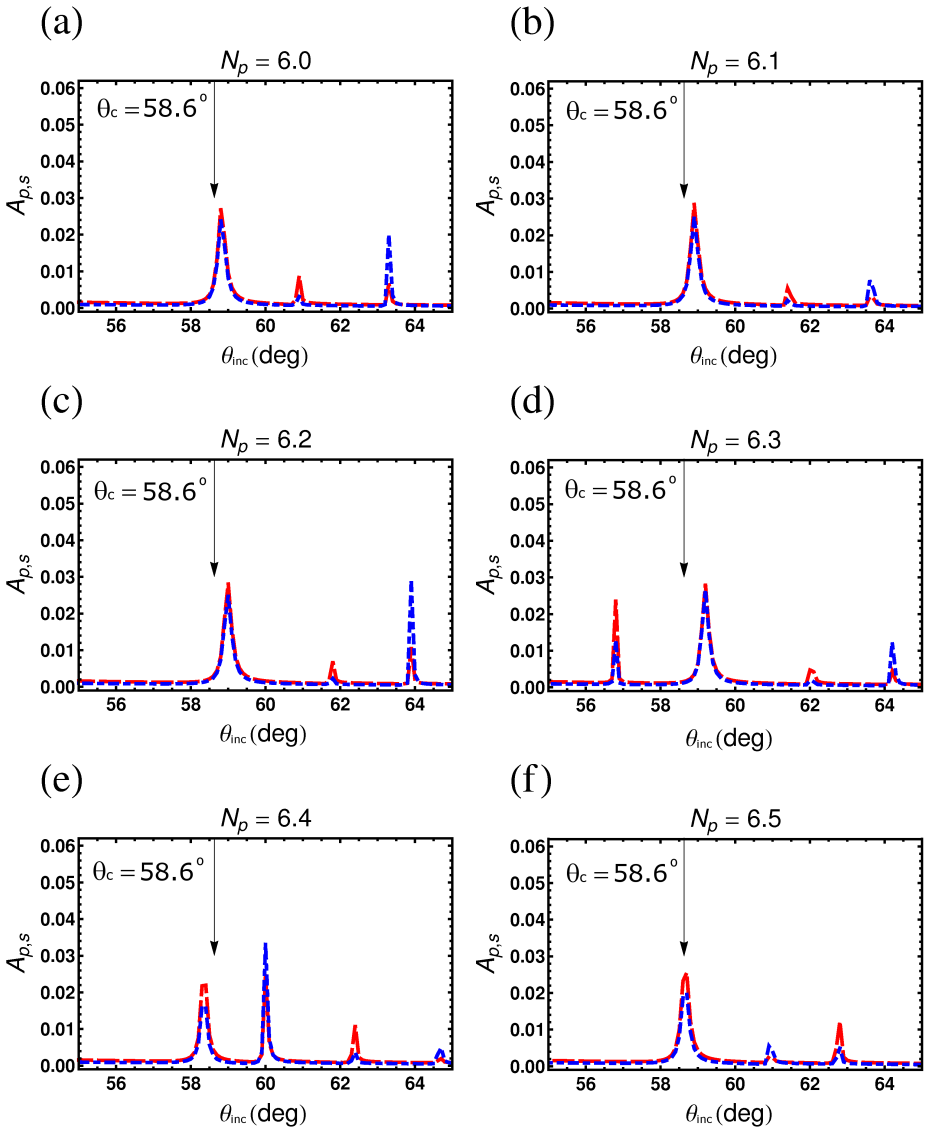

Figure 5.5: Absorptances A_p and A_s as functions of θ_{inc} in the prism-coupled configuration when (a) $N_p = 6.0$, (b) $N_p = 6.1$, (c) $N_p = 6.2$, (d) $N_p = 6.3$, (e) $N_p = 6.4$, and (f) $N_p = 6.5$. Other parameters are as follows: $\Omega = 150$ nm, $\chi_v = 20$ deg, $m = 1$, $h = 1$, and $\gamma = 45$ deg; $n_d = 1.377\left(1 + i10^{-4}\right)$ and $L_d = 300$ nm; $n_{prism} = 1.779$; and $n_\ell = 1$. A black arrow indicates the location of θ_C predicted by the solution of the canonical configuration.

difference between ϵ_a and ϵ_c vanishes when $\chi_v = 90$ deg. Moderately low values of χ_v provide large differences between ϵ_a, ϵ_b, and ϵ_c [112].

The effect of the value of χ_v was investigated by varying it between 16 and 30 deg while holding the other parameters fixed as follows: $\Omega = 150$ nm, $N_p = 6$, $m = 1$, $h = 1$, $\gamma = 45$

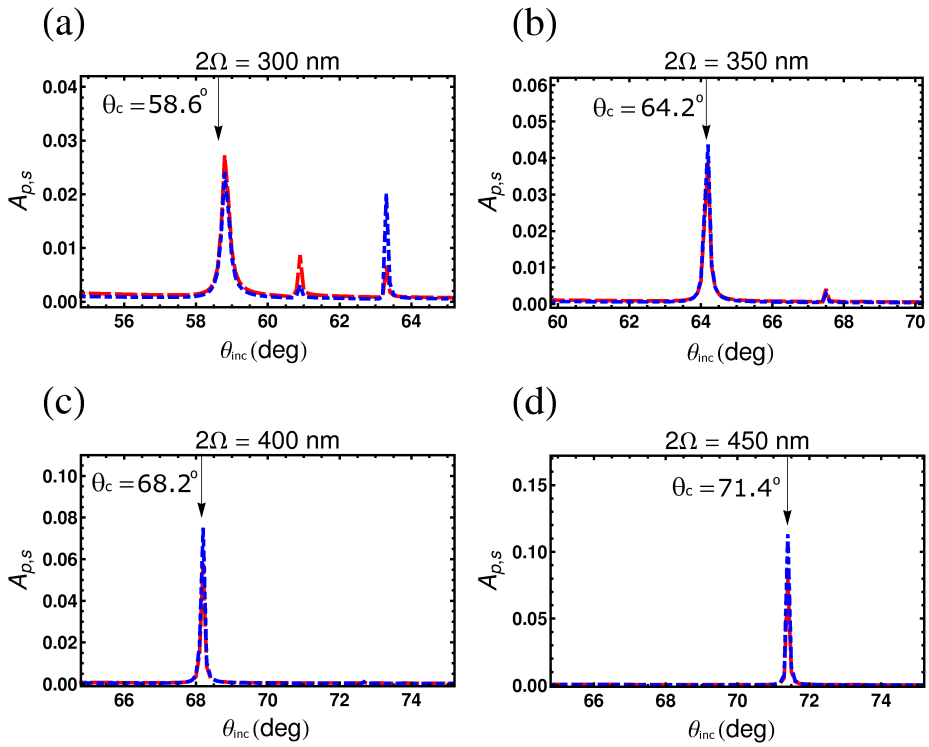

Figure 5.6: Absorptances A_p and A_s as functions of θ_{inc} in the prism-coupled configuration when (a) $\Omega = 150$ nm, (b) $\Omega = 175$ nm, (c) $\Omega = 200$ nm, and (d) $\Omega = 225$ nm. Other parameters are as follows: $\chi_v = 20$ deg, $N_p = 6$, $m = 1$, $h = 1$, and $\gamma = 45$ deg; $n_d = 1.377\left(1 + i10^{-4}\right)$ and $L_d = 300$ nm; $n_{prism} = 1.779$; and $n_\ell = 1$. The red dashed line is for A_p and the blue dot-dashed line for A_s. A black arrow indicates the location of θ_C predicted by the solution of the canonical problem.

deg, and $L_d = 300$ nm. Data for $\chi_v \in \{16, 20, 25, 30\}$ deg were selected for presentation. The plots of A_p and A_s against θ_{inc} presented in Fig. 5.7 show that Dyakonov–Tamm waves are excited at $\theta_{inc}^{DT} \in \{54.7, 58.8, 64.0, 70.4\}$ deg. Corresponding solutions of the canonical problem yielded $\theta_C \in \{54.4, 58.6, 64.0, 70.6\}$ deg. These data indicate that the angle of incidence for the excitation of a Dyakonov–Tamm wave in the prism-coupled configuration increases as χ_v increases in a range in which the local birefringence of the chiral STF is quite high.

As with the structural period, the vapor flux angle χ_v provides a route to tailor the angular location at which the Dyakonov–Tamm wave is excited in the prism-coupled configuration. Although this may appear to be a straightforward approach to designing an appropriate chiral STF, it would be difficult to implement due to the need to calibrate the deposition equipment for several values of χ_v. Additionally, χ_v influences many of the chiral STF's mechanical and optical

properties; making any direct comparison among chiral STFs produced at different values of χ_v problematic.

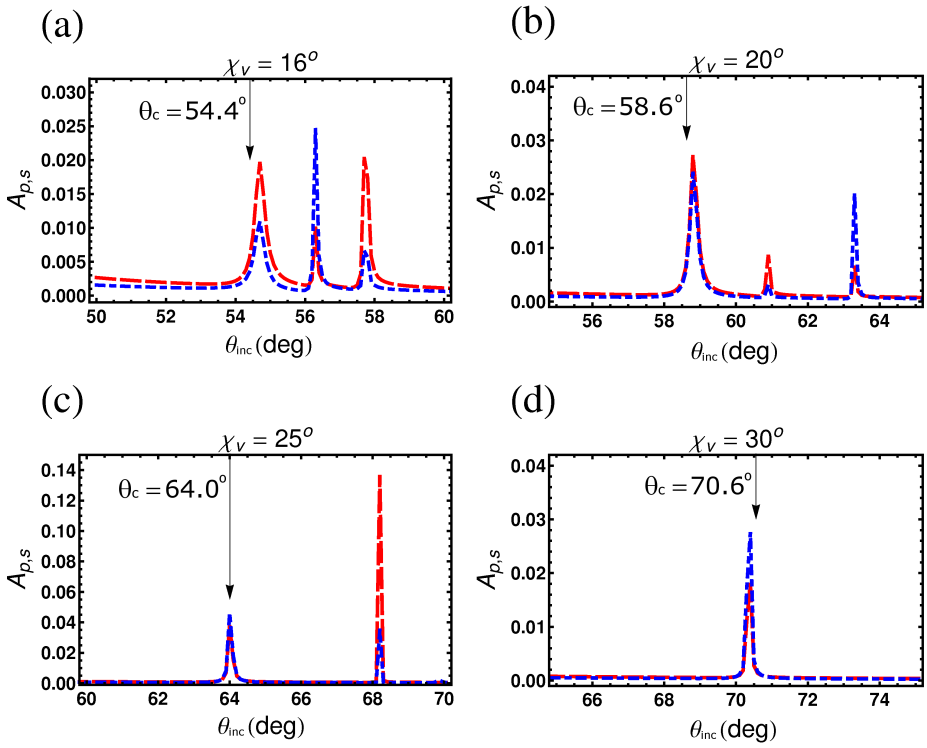

Figure 5.7: Absorptances A_p and A_s calculated as functions of θ_{inc} in the prism-coupled configuration when (a) $\chi_v = 16$ deg, (b) $\chi_v = 20$ deg, (c) $\chi_v = 25$ deg, and (d) $\chi_v = 25$ deg. Other parameters are as follows: $\Omega = 150$ nm, $\chi_v = 20$ deg, $N_p = 6$, $m = 1$, $h = 1$, and $\gamma = 45$ deg; $n_d = 1.377\left(1 + i10^{-4}\right)$ and $L_d = 300$ nm; $n_{prism} = 1.779$; and $n_\ell = 1$. The red dashed line is for A_p and the blue dot-dashed line for A_s. A black arrow indicates the location of θ_C predicted by the solution of the canonical problem.

5.4.4 Effect of γ

The offset angle γ effectively denotes the direction of propagation of the Dyakonov–Tamm wave, not in relation to the laboratory coordinate system, but with respect to a coordinate system whose x and y axes co-rotate about the z axis with the nanohelixes of the chiral STF. If Dyakonov–Tamm-wave propagation occurs for a specific value of γ, then it also occurs for $\gamma = \gamma + 180°$, due to the two-fold rotation symmetry of $\underline{\underline{\epsilon}}_{CSTF}$. Therefore, only the range $[0, 180)$ deg of γ needs to be investigated.

After fixing $\Omega = 150$ nm, $\chi_v = 20$ deg, $N_p = 6$, $m = 1$, $h = 1$, and $L_d = 300$ nm, it was found that solutions of the canonical problem exist for $\gamma \in [0, 13] \cup [21, 180)$ deg but not for $\gamma \in (13, 21)$ deg. From the plots of A_p and A_s as functions of θ_{inc} presented in Fig. 5.8 for $\gamma \in \{30, 60, 90, 120, 150, 180\}$ deg, we determined $\theta_{inc}^{DT} \in \{59.4, 57.9, 55.8, 52.9, 51.3, 49.9\}$ deg, while the solutions of the canonical problem yielded $\theta_C \in \{59.2, 57.8, 55.7, 53.6, 51.9, 50.9\}$ deg, correspondingly.

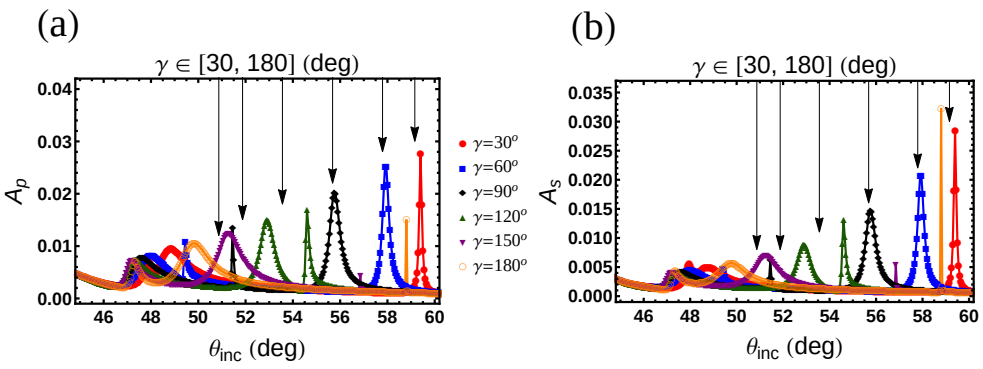

Figure 5.8: Absorptances (a) A_p and (b) A_s as functions of θ_{inc} in the prism-coupled configuration for $\gamma = \{30, 60, 90, 120, 150, 180\}$ deg, when $\Omega = 150$ nm, $\chi_v = 20$ deg, $N_p = 6$, $m = 1$, and $h = 1$; $n_d = 1.377\left(1 + i10^{-4}\right)$ and $L_d = 300$ nm; $n_{prism} = 1.779$; and $n_\ell = 1$. A black arrow indicates the location of θ_C predicted by the solution of the canonical problem.

Clearly, γ can be chosen in order to set the angular location of a Dyakanov–Tamm wave experimentally. The offset angle is particularly suited to this task, as it simply requires the rotating stage to which the substrate for the chiral STF is attached to be advanced or retarded prior to initiating the deposition. Alternatively, the substrate can also be rotated to the appropriate angle when it is attached to the prism before measurements are made. This is particularly appealing because just one sample could be used to find advantageous values of γ experimentally.

But the use of the offset angle to tailor the angular location of the Dyakanov–Tamm wave is not without complication. As can be observed in Fig. 5.8, the absorptance peaks associated with the excitation of a Dyaknov–Tamm wave broaden and θ_{inc}^{DT} exhibits poorer agreement with θ_C as γ increases, the discrepancy becoming severe for values of $\gamma > 90$ deg when N_p is moderate in

value.

5.4.5 Effect of m

When the foregoing calculations were repeated with $m = 1.1$—i.e., a 10% increase in the magnitudes of all components of $\underline{\underline{\epsilon}}_{CSTF}$—at least one solution of the canonical problem was found to exist for every $\gamma \in [0, 180)$ deg. More interestingly, two solutions were found to exist for every $\gamma \in [1, 23]$ deg. Given that the dielectric properties of no chiral STF have been completely measured, the dependence on m was considered to get an idea of how a chiral STF made by evaporating an isotropic material with a somewhat different bulk refractive index may function in the present context.

I calculated A_p and A_s as functions of θ_{inc} when $\Omega = 150$ nm, $\chi_v = 20$ deg, $N_p = 6$, $h = 1$, $\gamma = 45$ deg, and $L_d = 300$ nm, for $m \in \{0.93, 1.00, 1.15, 1.25\}$. Analysis of the data in Fig. 5.9 indicated that $\theta_{inc}^{DT} \in \{54.3, 58.8, 68.7, 78.6\}$ deg. The corresponding predictions from the solution of the canonical problem are $\theta_C \in \{54.3, 58.6, 68.7, 78.6\}$ deg. My conclusion is that a small increase in the bulk refractive index of the evaporant material raises the angle of incidence for the excitation of a Dyakonov–Tamm wave.

5.5 Concluding Remarks

Various parameters of a chiral sculptured thin film that partners a homogeneous isotropic material were theoretically investigated for their effects on the propagation of a Dyakonov–Tamm wave in the prism-coupled configuration. In each case, an absorptance peak that was independent of the integer number of periods in the chiral STF beyond a threshold, was identified for the prism-coupled configuration and its angular location θ_{inc}^{DT} was compared to the angular location θ_C predicted by the solution of the underlying canonical problem.

The prism (and the refractive-index-matched substrate) should be made of an isotropic dielectric material of relative permittivity that exceeds the highest principal relative permittivity scalar of the chiral STF. The other partnering material should also have a relative permittivity smaller than of the prism, and must have a slight dissipation for appreciable absorptance. From several parametric studies, it was concluded

(i) the chiral STF needs to have a moderate number of periods for experimental observation;

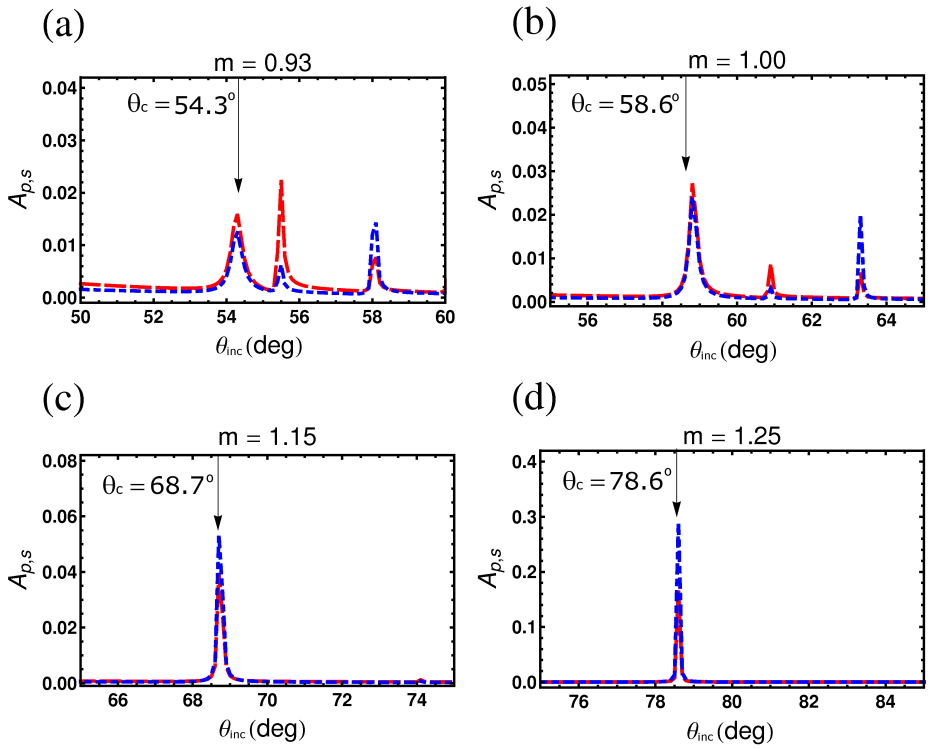

Figure 5.9: Absorptances A_p and A_s as functions of θ_{inc} in the prism-coupled configuration when (a) $m = 0.93$, (b) $m = 1.00$, (c) $m = 1.15$, and (d) $m = 1.25$. Other parameters are as follows: $\Omega = 150$ nm, $\chi_v = 20$ deg, $N_p = 6$, $h = 1$, and $\gamma = 45$ deg; $n_d = 1.377\left(1 + i10^{-4}\right)$ and $L_d = 300$ nm; $n_{prism} = 1.779$; and $n_\ell = 1$. The red dashed line is for A_p and the blue dot-dashed line for A_s. A black arrow indicates the location of θ_C predicted by the solution of the canonical problem.

(ii) the experimental identification of the excitation of the Dyakonov–Tamm wave can become complicated, if the ratio of the the thickness of the chiral STF to its period is not an integer;

(iii) an increase in the period of the chiral STF results in a larger angle of incidence for experimental observation;

(iv) an increase in the vapor flux angle during the deposition of the chiral STF results in a larger angle of incidence for experimental observation;

(v) an increase in the offset angle results in a decrease of angle of incidence for experimental observation; and

(vi) an increase in the bulk refractive index of the material, from which the chiral STF is

fabricated, is likely to increase the angle of incidence for experimental observation.

Of the control parameters Ω, χ_v, and γ that can be used to influence Dyakonov–Tamm-wave propagation, the one most easily varied experimentally is γ, followed by 2Ω and finally χ_v. For a realistic set of materials, I found θ_{inc}^{DT} as low as ~ 50 deg and as high as ~ 70 deg, indicating that a great deal of control over the angular location of the Dyakanov–Tamm wave can be achieved by properly choosing the structural parameters of the chiral STF. As with other surface waves, Dyakonov–Tamm waves are expected to have significant sensing applications. Due to their large angular existence domain and broader absorptance peaks, it is expected that Dyakonov–Tamm waves will be much easier to excite experimentally than Dyakonov waves.

In Ch. 5, I have established trends in the propagation of the Dyakonov–Tamm that result from the alteration of various structural parameters of the chiral STF partnering material. Knowledge of these trends aided with the selection of the partnering materials and structural parameters of the chiral STF that are used in Ch. 6 to make the first experimental observation of the Dyakonov–Tamm wave.

Chapter 6

Observation of the Dyakonov–Tamm Wave in the Prism-Coupled Configuration[‡]

Guided by the theoretical results produced in Ch. 5, appropriate partnering materials were selected and the structural parameters of the partnering chiral STF which support the propagation of the Dyakonov–Tamm wave were found. In Ch. 6, the Dyakonov–Tamm wave is demonstrated in the prism-coupled configuration which utilizes a planar interface of the partnering materials. Subsequently, in Ch. 7 the Dyakonov–Tamm wave is demonstrated in the grating-coupled configuration which utilizes a periodically corrugated interface of the partnering materials.

6.1 Chapter Summary

The Dyakonov–Tamm wave is an electromagnetic surface wave that was predicted to exist at the interface of two dielectric materials at least one of which is anisotropic and periodically nonhomogeneous in the direction normal to the interface. In order to make the first experimental observation of the Dyakonov–Tamm wave the prism-coupled configuration was utilized to excite a Dyakonov–Tamm wave at the interface between a magnesium-fluoride thin film and a zinc-

[‡]This chapter is based on: Pulsifer, D. P., Faryad, M., and Lakhtakia, A., "Observation of the Dyakonov–Tamm wave," *Physical Review Letters*, accepted for publication.

selenide chiral sculptured thin film. In this configuration, the excitation of a Dyakonov–Tamm wave is indicated by a reflection dip that occurs at the same angle of incidence independent of the thickness of each partnering material, beyond some threshold, as well as the polarization state of the incident light.

This chapter represents a sequential step towards the experimental excitation of a Dyakonov–Tamm wave on a non-planar substrate. The prism-coupled configuration allows for planar substrates to be used order to more easily identify appropriate partnering materials and structural parameters of the chiral sculptured thin film that will support the propagation of the Dyakonov–Tamm wave. This design can then be adapted to demonstrate the grating-coupled excitation of the Dyakonov–Tamm wave.

6.2 Introduction

The most recently discovered electromagnetic surface wave was predicted by Lakhtakia and Polo in 2007 [47]. In this case the interface of two dielectric materials, one of which is both anisotropic and periodically nonhomogeneous in the direction perpendicular to the interface plane was found to support an electromagnetic surface wave. Because the interface supporting this surface wave combines attributes of both Tamm [88] and Dyakonov [92] waves, this electromagnetic surface wave was termed a Dyakonov–Tamm wave.

In the time since the initial discovery of the Dyakonov–Tamm wave, many interface configurations which are expected support Dyakonov–Tamm waves have been theoretically investigated [47, 107, 110, 114–116]. Of these, the interface of a chiral sculptured-thin-film (chiral STF) and a homogeneous, isotropic dielectric thin film have shown the greatest promise for efforts to experimentally verify the existence of the Dyakonov–Tamm wave [116].

A chiral STF is a collection of parallel nano-helices which can be produced by slowly rotating a substrate about its surface normal while directing a columnated vapor flux–in vacuum–at an oblique angle with respect to the substrate's surface [31]. By controlling the rate at which the vapor condenses onto the substrate, the angle at which the vapor impinges, and the speed at which the substrate rotates, the structural and optical properties of the chiral STF can be tailored. The ability to finely and easily tune the structural and optical properties of a chiral STF make them particularly well suited for the observation of the Dyakonov–Tamm wave [116].

Here I report the first experimental observation of the Dyakanov–Tamm wave. A prism-coupled configuration was adapted as the method to direct light towards the interface of a chiral STF and a homogeneous, isotropic dielectric material. In this configuration, shown schematically in Fig. 6.1(a), the hypotenuse of a right-angled isosceles prism is affixed to a substrate by a refractive-index-matching fluid. The prism and the substrate are optically matched, both having a refractive index n_{prism}. On the other face of the substrate, a homogeneous, isotropic dielectric material of thickness L_d and a chiral STF of thickness L_{CSTF} had been deposited earlier. The ratio $N_p = L_{CSTF}/2\Omega$ is an integer, where 2Ω is the structural period; then, N_p is the number of structural periods of the chiral STF. With the interface of the substrate and the isotropic partnering material serving as the plane $z = 0$, the region defined by $z > L_\Sigma = L_d + L_{CSTF}$ in Fig. 6.1(a) is occupied by air.

The plan for this chapter is as follows: In Sec. 6.3 the process by which samples were fabricated is presented. Next, the morphology of the thin films in the sample are characterized in Sec. 6.4. The excitation of the Dyakonov–Tamm wave in the prism-coupled configuration is described in Sec. 6.5. The results of the experiments are presented in Sec. 6.6. The Dyakonov–Tamm wave's localization and propagation length is compared to Tamm and SPP waves, respectively, in Sec. 6.7. Finally, conclusions are given in Sec. 6.8.

6.3 Fabrication of Samples

Samples were fabricated by first thermally evaporating an isotropic and homogeneous layer of magnesium fluoride onto a dense flint glass (SF11) substrate (Swiss Jewel Co., Philadelphia, PA, USA) in a custom-made vacuum chamber. The intended direction of Dyakonov–Tamm-wave propagation was marked by a straight line (the x axis in Fig. 6.1(a) on one face of the substrate, and then that face was affixed to the stage face. Then the substrate was shuttered, the chamber was evacuated to a pressure of 10 μTorr, and a current that slowly increased to 110 A was passed through a tungsten receptacle containing magnesium fluoride. The shutter was then removed, and the collimated portion of the magnesium-fluoride vapor flux was directed normally towards the substrate which was being rotated at 120 rpm. The current was adjusted manually to maintain a deposition rate of ~ 0.4 nm s^{-1}, as indicated by the quartz crystal monitor, while the layer of thickness L_d was being deposited. After being left in vacuum for several hours in order to cool,

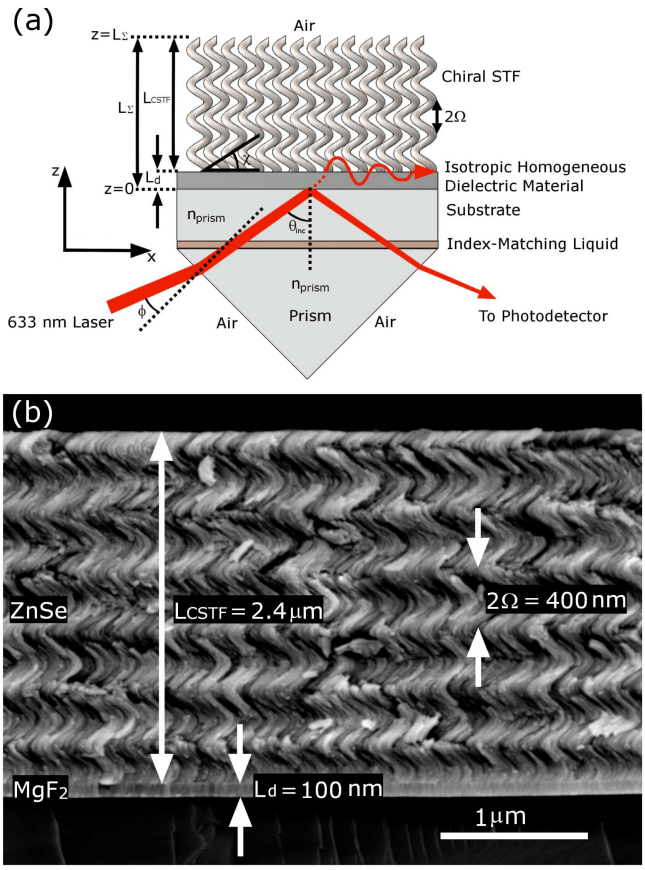

Figure 6.1: (a) Schematic representation of the prism-coupled configuration used to excite a Dyakonov–Tamm wave at the interface of a homogeneous isotropic dielectric layer and a chiral STF. The portion of the path of light relevant to the identification of surface waves in the prism-coupled configuration is also shown. (b) Cross-sectional field-emission SEM image of the magnesium-fluoride/zinc-selenide structure fabricated on a silicon wafer.

the sample was exposed to atmosphere.

Then the substrate was rotated about its surface normal by an offset angle 45 deg, as indicated by parametric simulations [116] to offer the most favorable conditions for the observation of a Dyakanov–Tamm wave. The source boat was then filled with zinc selenide, the magnesium-fluoride coated substrate was shuttered, the chamber was evacuated to a base pressure of 0.4 μTorr, and the current passing through the source boat was increased slowly to 98 A. The substrate was then reoriented so the collimated portion of the zinc-selenide vapor flux would be directed at 20 deg with respect to the substrate plane, a substrate rotation sequence was initiated, and the shutter was removed. The rotation sequence for the deposition of the chiral STF

involved 20 discrete steps per revolution while holding the substrate stationary for an interval of 75 s between each movement. As the current manually was adjusted to maintain a deposition rate of 0.27 nm s^{-1}, a structurally right-handed chiral STF with a structural period $2\Omega \sim 400$ nm was deposited. Once the desired final thickness of the chiral STF was achieved, the sample was shuttered, the current passing through the source boat was decreased to 0 A, and the sample was left under vacuum for several hours to cool prior to exposing it to atmosphere.

Samples of six different types were made: the magnesium-fluoride layer was either $L_d \sim 100$ or 150-nm thick, and the zinc-selenide chiral STF had either $N_p = 4$, or 5, or 6 structural periods.

6.4 Characterization of Morphology

Along with each flint-glass substrate, a silicon wafer was placed on the stage. Thus, the magnesium-fluoride/zinc-senelide structure was also deposited on the silicon wafer for the verification of morphology. The silicon wafer was used to avoid troubles caused by charging of the SF11 glass substrate when imaging with a scanning electron microscope (SEM). The wafer with the magnesium-fluoride/zinc-selenide structure was immersed in liquid nitrogen and fractured with a punch to reveal a cleaved plane for cross-sectional images to be obtained. Images were obtained for each combination of films on a field-emission SEM (FEI Nova NanoSEM 630, Hillsboro, OR, USA). As an example, the image in Fig. 6.1(b) reveals a $\sim$ 100 nm magnesium-fluoride layer conjoined with a chiral STF with $N_p = 6$ structural periods, each of thickness $2\Omega \sim 400$ nm.

6.5 Excitation of the Dyakonov–Tamm Wave

The prism-coupled configuration of Fig. 6.1(a) was implemented with a right-angled isosceles prism made of SF11 glass (Edmund Optics, Barrington, NJ, USA). The chosen index-matching fluid has a refractive index of 1.777 at 633 nm wavelength, as yielded by the Cauchy equation formulated using data supplied by the manufacturer (Cargille Laboratories, Cedar Grove, NJ, USA). The prism/sample combination was then mounted in a commercial device (Metricon 2010/M, Metricon, Pennington, NJ, USA). A 633-nm wavelength He-Ne laser (CVI Melles-Griot, Albuquerque, NM, USA) was oriented to ensure that the light incident on the prism would be p polarized (i.e., the magnetic field of the incident light would be aligned with the y axis).

With p-polarized light incident on a slanted face of the prism at an angle ϕ, the intensity $R(\phi)$ of the light exiting the other slanted face of the prism was measured. The angle of incidence θ_{inc} on the magnesium-fluoride/zinc-selenide structure was computed as $\theta_{inc} = 45^\circ + \sin^{-1}(n_{prism}^{-1} \sin\phi)$, with $n_{prism} = n_{SF11} = 1.779$. A half-wave plate was then inserted into the beam-path of the incident laser to convert the p-polarized light incident on the prism to the s-polarized light (i.e., the electric field would be aligned with the y axis), and the measurement of the intensity of the exiting light was repeated.

The sample was then removed from the hypotenuse of the prism and the intensity $R_\circ(\phi)$ of the light exiting the prism was again measured as a function of ϕ for each of the two incident polarization states. Measured values of the ratio $R(\theta_{inc})/R_\circ(\theta_{inc})$ were plotted against θ_{inc} for all six samples and for both polarization states. This normalization is meaningful, because total internal reflection occurs at the interface of the prism and air for $\theta_{inc} \geq \sin^{-1}(1/n_{prism}) = 34.2$ deg.

6.6 Results and Discussion

A sharp dip in the $R(\theta_{inc})/R_\circ(\theta_{inc})$ vs. θ_{inc} curve is indicative of the excitation of a surface wave, provided its location on the θ_{inc}-axis is independent of both L_d and N_p beyond certain threshold values of both parameters [75, 116]. This is reasonable because a surface wave is localized to a specific interface, and increasing the thickness of either partnering material beyond a threshold will not affect the spatial profiles of the fields of a surface wave.

Figure 6.2 shows $R(\theta_{inc})/R_\circ(\theta_{inc})$ vs. θ_{inc} curves for $N_p \in \{4, 5, 6\}$ when $L_d \sim 100$ nm. These three curves have a sharp dip in $R/R_\circ$ at $\theta_{inc} \sim 57.5$ deg. Aligned dips at $\theta_{inc} \sim 57.5$ deg also occur in Figs. 6.3(a) and (b) for $N_p = 6$ when $L_d \in \{100, 150\}$ nm for p- and s-polarization states, respectively. All of these dips indicate that a surface wave is indeed excited at $\theta_{inc} \sim 57.5$ deg.

The smaller change in the angular position of the dip in Fig. 6.2 when N_p changes to 6 from 5 than when it changes to 5 from 4 indicates that the Dyakonov–Tamm wave is essentially confined to within 6 structural periods (~ 2.4 μm) of the chiral STF. Similarly, a very small change in the angular position of the dip when L_d changes from 150 nm to 100 nm shows that the Dyakonov–Tamm wave is confined to within 150 nm in magnesium fluoride. In comparison, optical Tamm states are less localized than Dyakonov–Tamm waves. For instant, optical Tamm

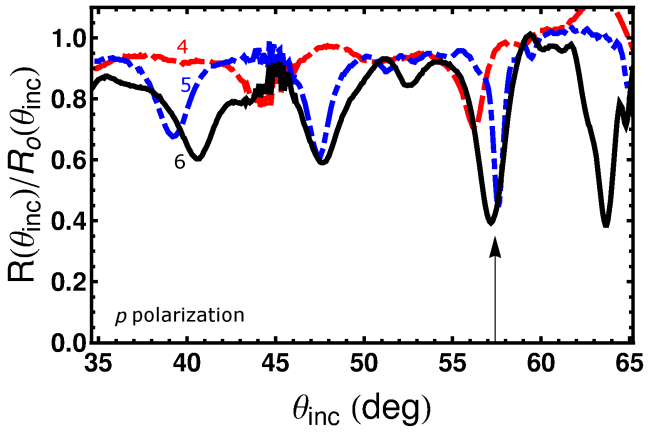

Figure 6.2: Measured values of $R(\theta_{inc})/R_{\circ}(\theta_{inc})$ vs. the incidence angle θ_{inc} for $N_p = 4$ (red dashed curve), 5 (blue dotted-and-dashed curve), and 6 (black curve), when $L_d \sim 100$ nm and the incident light is p polarized. The excitation of a Dyakonov–Tamm wave at $\theta_{inc} \sim 57.5$ deg is indicated by the vertical arrow.

states are spread at least 2 μm on either side of the interface between two piecewise homogeneous isotropic dielectric materials [95, Fig. 1] and at least 6 μm on either side of the interface of two continuously and periodically nonhomogeneous isotropic dielectric materials [96, Fig. 7].

The question of which interface is supporting the propagation of the surface wave arises. In the prism-coupled configuration, there are three relevant interfaces. The first interface, between the SF11 substrate and the magnesium-fluoride layer, can not support the propagation of a surface wave as there exists no solutions to the dispersion equation for that interface [75, App. C]. The other two relevant interfaces are the magnesium-fluoride/zinc-selenide interface $z = L_d$ and the zinc-selenide/air interface $z = L_\Sigma$. A surface wave guided by either of these two interfaces has to be a Dyakonov–Tamm wave, by definition. Thus, Figs. 6.2 and 6.3 are proof of the first observation of the Dyakonov–Tamm wave.

In order to resolve whether the Dyakonov–Tamm wave in Figs. 6.2 and 6.3 is guided by the magnesium-fluoride/zinc-selenide interface or the zinc-selenide/air interface, another experiment was conducted. The sample made for this experiment had $N_p = 5$ structural periods of the zinc-selenide chiral STF, but did not have the magnesium-fluoride layer. Because light in the prism is not evanescent when θ_{inc} is in a quite large neighborhood of 57.5 deg, the SF11/zinc-selenide interface can not guide a Dyakonov–Tamm wave in the prism-coupled experiment conducted with the magnesium-fluoride deficient sample. Therefore, any sharp dip at $\theta_{inc} \sim 57.5$ deg in

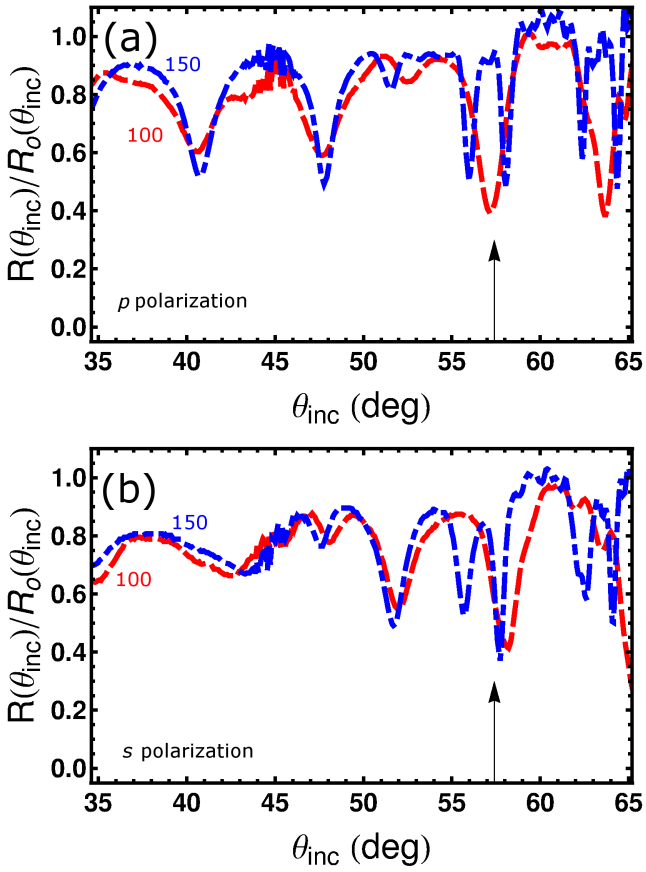

Figure 6.3: Measured values of $R(\theta_{inc})/R_{\circ}(\theta_{inc})$ vs. the incidence angle θ_{inc} for $L_d \sim 100$ nm (red dashed curve) and 150 nm (blue dotted-and-dashed curve), when $N_p = 6$. The incident light is either (a) p polarized or (b) s polarized. The excitation of a Dyakonov–Tamm wave is indicated by the vertical arrows at $\theta_{inc} \sim 57.5$ deg.

the $R(\theta_{inc})/R_{\circ}(\theta_{inc})$ vs. θ_{inc} curve for both polarization states can only be attributed to a Dyakonov–Tamm wave guided by the zinc-selenide/air interface. Figure 6.4 shows the results of this experiment which demonstrates, through the absence of a dip near $\theta_{inc} \sim 57.5$ deg, that the zinc-selenide/air interface did not guide the Dyakonov–Tamm wave observed in the earlier experiments. Accordingly, the Dyakonov–Tamm wave observed in Figs. 6.2 and 6.3 was guided by the interface of the magnesium-fluoride layer (a homogeneous, isotropic dielectric material) and the zinc-selenide chiral STF (a periodically nonhomogeneous, anisotropic dielectric material).

Note that reflectance dips at $\theta_{inc} \sim 48$ deg in Figs. 6.2 and 6.3 could indicate the excitation

of another Dyakonov–Tamm wave—with larger phase speed than the Dyakonov–Tamm wave excited at $\theta_{inc} \sim 57.5$ deg. This Dyakonov–Tamm wave would be less tightly bound to the magnesium-fluoride/zinc-selenide interface, because a dip at $\theta_{inc} \sim 48$ deg is missing in Fig. 6.2 for $N_p = 4$.

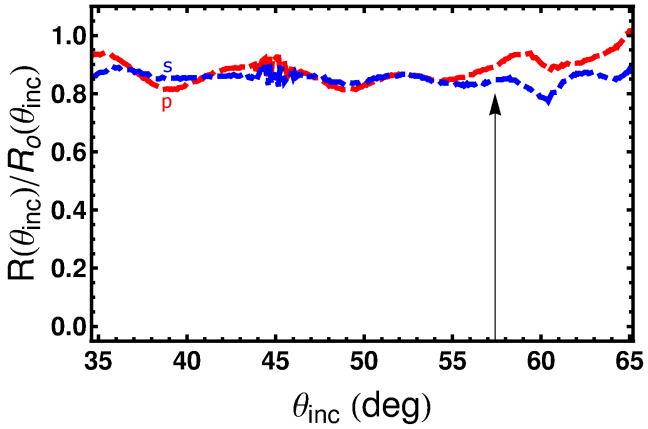

Figure 6.4: Measured values of $R(\theta_{inc})/R_\circ(\theta_{inc})$ vs. the incidence angle θ_{inc} for p polarized (red dashed curve) and s polarized (blue dotted-and-dashed curve) incident light, when the magnesium-fluoride layer is absent and $N_p = 5$. There is no dip at $\theta_{inc} \sim 57.5$ deg, indicating that a Dyakonov–Tamm wave is not excited at the zinc-selenide/air interface.

6.7 Comparing Localization with Tamm Waves and Propagation Length with SPP Waves

The solution of the canonical boundary-value problem shows that Dyakonov–Tamm waves must propagate without loss if the dissipation in the partnering dielectric materials is ignored [47]. Therefore, the losses in the propagation of Dyakonov–Tamm waves are not intrinsic and are only dependent on the losses in the partnering dielectric materials. This is in contrast to the propagation of SPP waves that requires one partnering material to be a metal [75, 77], which dissipates energy and is a fundamental obstacle in increasing the propagation length of the SPP waves. For a comparison of the propagation lengths of the Dyakonov–Tamm waves and SPP waves, the relevant canonical boundary-value problems were solved. In the absence of principal refractive index of the chiral STF made of zinc selenide, we chose chiral STF made by evaporating patinal titanium oxide. The same results should qualitatively hold for zinc-selenide chiral STF

since it has the same morphology as that of the chosen titanium-oxide chiral STF.

Table 6.1: Computed values of the propagation lengths of the surface waves guided by a planar interface of a titanium-oxide chiral STF with magnesium fluoride ($n_{MgF_2} = 1.377(1 + i10^{-4})$), gold ($n_{Au} = 0.183 + i3.433$), or aluminum ($n_{Al} = 0.75 + i3.9$) as the partnering material in the canonical boundary-value problem when $\chi_v = 20°$, $\Omega = 200$ nm, $\gamma = 45°$ and $\lambda_\circ = 633$ nm,.

Surface wave	Interface	Propagation length (μm)
Dyakonov–Tamm	MgF_2/chiral STF	509.3
SPP	gold/chiral STF	76.1
		2.4
	aluminum/chiral STF	43.8
		1.1

The propagation lengths of the Dyakonov–Tamm and SPP waves guided by the interfaces with the titanium-oxide chiral STF are presented in Table 6.1. The three principal refractive indexes of the titanium-oxide chiral STF were taken from Hodgkinson *et al.* [112] and a small imaginary part was added: ($n_a = 1.585(1+i10^{-4})$, $n_b = 1.986(1+i10^{-4})$, $n_c = 1.776(1+i10^{-4})$ at free-space wavelength $\lambda_\circ = 633$ nm. The other parameters of titanium-oxide chiral STF were chosen to be the same as for zinc selenide chiral STF fabricated for the experiments to observe the Dyakonov–Tamm waves: $\chi_v = 20$ deg, $\Omega = 200$ nm, and $\gamma = 45$ deg. For the homogeneous partnering dielectric material, magnesium fluoride ($n_{MgF_2} = 1.377(1 + i10^{-4})$), gold ($n_{Au} = 0.183 + i3.433$ [117]), and aluminum ($n_{Al} = 0.75 + i3.9$ [118]) were chosen. The propagation length was defined as the distance after which the amplitude of the electric field decays by a factor of $\exp(-1)$. Table 6.1 clearly shows that the Dyakonov–Tamm wave has a much larger propagation length than the SPP waves. Let us note that an interface of a metal and a chiral STF can guide multiple SPP waves of different phase speeds, spatial profiles, phase speeds, and degrees of localization but all of the same frequency and direction of propagation. The chosen metals (gold and aluminum) were found to guide two SPP waves with different propagation lengths, however, both of them are much shorter than the Dyakonov–Tamm wave.

6.8 Conclusions

The first experimental observation of the Dyakonov–Tamm wave, confirming theoretical predictions, opens a new avenue in the realm of electromagnetic surface waves. Optical sensing and

long-range on-chip communication are among the simpler applications of this new type of surface wave. In particular, as a chiral STF is a porous material that can be infiltrated by solutions of analytes, application for optical sensing should follow shortly. High sensitivity is expected because the Dyakonov–Tamm wave is expected to propagate over long distances due to the absence of non-dissipative partnering materials (such as metals) and thus have a large interaction volume. Furthermore, as multiple modes of Dyakonov–Tamm wave propagation are possible at the same frequency [119], multi-analyte sensing may be possible, with proper selection of the partnering materials.

In this chapter, the Dyakonov–Tamm wave was demonstrated in the prism-coupled configuration which utilized a planar interface of the partnering materials. In Ch. 7, the Dyakonov–Tamm wave is demonstrated in the grating-coupled configuration which utilizes a periodically corrugated interface of the partnering materials.

Chapter 7

Observation of the Dyakonov–Tamm Wave in the Grating-Coupled Configuration

In Ch. 6 the propagation of the Dyakonov–Tamm wave guided by a planar interface was demonstrated experimentally. The propagation of the Dyakonov–Tamm wave guided by a periodically corrugated interface is demonstrated in this chapter. The experimental procedure required the deposition of a conformal thin film with a specific and complicated morphology on a non-planar substrate. Thereby the efficacy of thermally evaporated conformal thin films on non-traditional/non-planar substrates is demonstrated.

7.1 Chapter Summary

Here I report the experimental observation of the Dyakonov–Tamm wave excited in the grating coupled-configuration. Magnesium-fluoride gratings were produced in a two-stage replication process which served as the isotropic homogeneous partnering material to the periodically non-homogeneous and anisotropic material fabricated from zinc selenide as a chiral sculptured thin film. The transmittance of a *p*-polarized 633-nm laser beam was measured as a function of the incidence angle for several thicknesses of the chiral STF to identify dips which are independent

in their angular location of the thickness (beyond a threshold value) of the chiral STF to identify the excitation of a Dyakonov–Tamm wave.

7.2 Introduction

The experimental observation of the Dyakonov–Tamm wave was demonstrated using a prism-coupled configuration in Ch. 5. As with other types of electromagnetic surface waves such as SPP waves [85], Tamm waves [90], and Dyakonov waves [94], Dyakonov–Tamm waves [47, 120] can be excited in several experimental configuration [75].

For practical applications, one of the most common methods of exciting electromagnetic surface waves is grating coupling [77]. In this method a periodically patterned material can be used to couple light across an interface, provided the wave vector of the incident light matches one of the Floquet harmonics of the given grating. These conditions are dictated by the angle at which the incident light falls on the grating, the wavelength of the incident light, and the characteristic period of the grating. In a scenario where the wavenumber of an ESW matches the wavenumber of a given Floquet harmonic, the coupling of light by the grating can excite the ESW at the periodically corrugated interface [75]. The type of ESW which will be excited is dictated by the properties of the two materials at the interface: if the interface is between a metal and a dielectric, an SPP wave will be launched; if the interface is between two dielectric materials, at least on of which is periodically nonhomogeneous normal to the interface, a Tamm wave will be launched; if the interface is between two dielectric materials, at least on of which is anisotropic, it is possible to launch a Dyakonov wave; and if the interface is between two dielectrics, one of which is both anisotropic and periodically nonhomogeneous, it is possible to launch a Dyakonov–Tamm wave.

The plan for this chapter is as follows: In Sec. 7.3 the process by which samples were fabricated is presented. The grating-coupled excitation of the Dyakonov–Tamm wave is described in Sec. 7.4. The results of the experiments are presented in Sec. 7.5, and conclusions are given in Sec. 7.6. Figure 7.1 shows a schematic of the structure fabricated for this research.

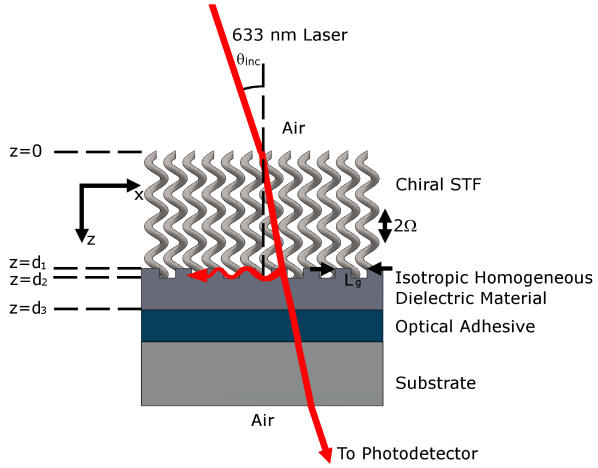

Figure 7.1: Schematic representation of the grating-coupled configuration used to excite a Dyakonov–Tamm wave at the interface of a homogeneous dielectric layer of magnesium-fluoride and a zinc-selenide chiral STF.

7.3 Fabrication of Samples

Gratings were produced through a two-stage replication process. Starting with a 1D grating with a $L_g = 350$-nm period, $d_2 - d_1 = 93$-nm depth, and 50% duty cycle that had been produced on a silicon wafer by electron-beam lithography, the first-stage replica was produced by thermally evaporating an $\sim$ 250-nm thick gold film on it. A glass slide was then attached to the gold-coated silicon grating with Norland Optical Adhesive 61 (NOA61) (Norland Products, Cranbury, NJ). When the silicon wafer was mechanically separated from the glass slide, the gold grating remained attached to the glass slide, thereby resulting in a gold replica of the original grating. To produce the second-stage grating replica, the gold grating on the glass substrate was coated with a 900-nm thick magnesium-fluoride thin film, attached to a second glass slide with NOA61, and then the glass slides with the gold and magnesium fluoride were mechanically separated to leave a magnesium-fluoride grating attached to one of the glass slides. Prior to the deposition of the gold or magnesium-fluoride film, the evaporation chamber had been pumped to a base pressure of ~ 6 μTorr; both films were deposited with normal vapor incidence ($\chi_v = 90$ deg) and without substrate rotation, at a deposition rate of ~ 0.8 nm s^{-1}. Photographs and SEM images of the sequence of replicated gratings are provided in Fig. 7.2.

The magnesium-fluoride/NOA61/glass assembly then served as the substrate upon which a zinc-selenide chiral STF was deposited. The substrate was initially positioned with a vapor-flux

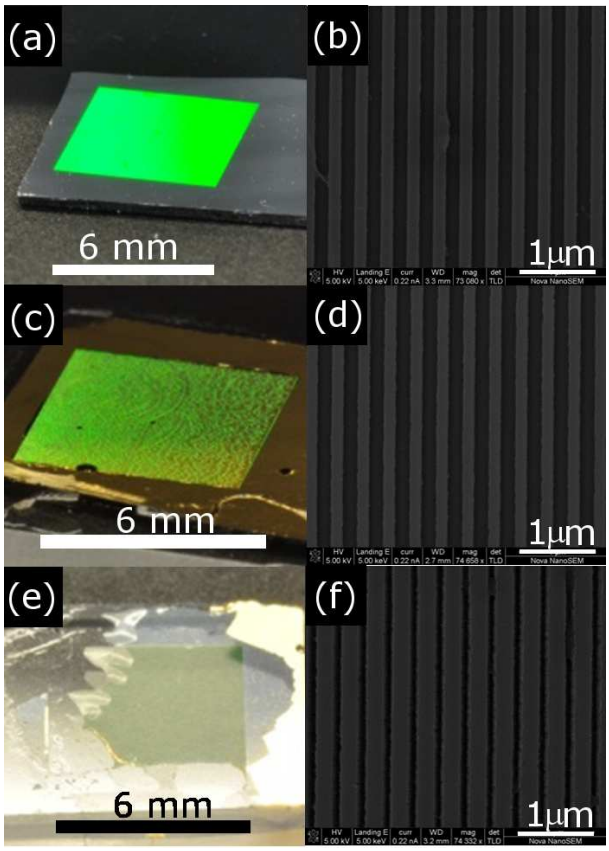

Figure 7.2: Photographs and corresponding SEM images of the sequence of replicated gratings. (a) Photograph of the original silicon grating; (b) SEM image of the original silicon grating; (c) photograph of the gold grating replicated from the original silicon grating; (d) SEM image of the gold grating; (e) photograph of the magnesium-fluoride grating replicated from the gold grating; and (f) SEM image of the magnesium-fluoride grating.

angle $\chi_v = 20$ deg and an initial growth direction specified by $\gamma = 45$ deg as measured from the optically significant axis of the grating. Once the assembly was positioned, the evaporation chamber was evacuated until a base pressure of ~ 2 μTorr was reached, and the film deposition was initiated. The zinc-selenide chiral STF was deposited at a constant deposition rate of 0.27 nm s^{-1} while the substrate stage was rotated about its surface normal; this rotation was carried out in 20 discreet steps per revolution with a 75-s pause between each step. In this way structurally right-handed zinc-selenide chiral STFs of $N_p = 5,\ 6,$ and 7 periods were produced with structural periods of $2\Omega = 400$ nm resulting in a chiral STF thickness $d_1 = 2\Omega\, \mathrm{N}_p \in \{2000,\ 2400,\ 2800\}$ nm. Figure 7.3(a) shows a cross sectional SEM image of the NOA61/magnesium-fluoride/zinc-selenide structure with an $\mathrm{N}_p = 7$ chiral STF, while Fig. 7.3(b) shows an image in which the magnesium-

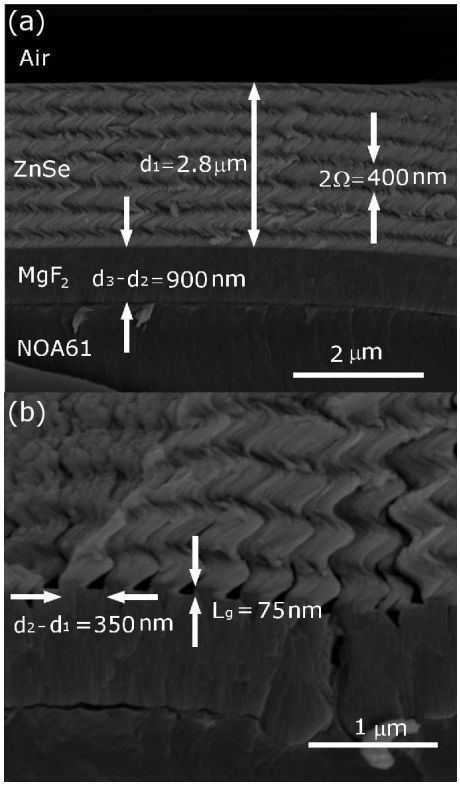

Figure 7.3: Cross sectional FESEM images of (a) the entire magnesium-fluoride/zinc-selenide structure and (b) a close up of the grating/chiral STF interface.

fluoride grating is visible at its interface with the zinc-selenide chiral STF. Note that the grating height $d_2 - d_1$ in Fig. 7.3(b) is ~ 75 nm rather than the 93 nm or the original silicon grating, but the grating period $L_g = 350$ nm with a 50% duty cycle is maintained through the two stages of replication.

7.4 Grating-Coupled Excitation

The grating-coupled configuration, shown schematically in Fig. 7.1, was implemented by mounting the sample in a modified Metricon Model 2010/M prism coupler (Metricon Corporation, Pennington, NJ). A 633-nm Melles-Griot He-Ne laser was oriented to produce p-polarized incident light. With p-polarized light incident on the chiral STF at an angle θ_{inc} as measured from the surface normal, the intensity $t(\theta_{inc})$ of the light transmitted through the sample was measured. The sample was then removed and the reference intensity $I_\circ(\theta_{inc})$ of the laser collected. Transmittance was then calculated as the ratio of the transmitted light to the incident

light $T(\theta_{inc}) = t(\theta_{inc})/I_{\circ}(\theta_{inc})$. This was repeated for $N_p \in \{5, 6, 7\}$.

7.5 Experimental Results

The calculated transmittance is shown in Fig. 7.4 with: $N_p = 5$ shown by the red dashed line, $N_p = 6$ by the blue dotted-and-dashed line, and $N_p = 7$ by the solid black line. It can be seen that the dip in transmittance is nearly independent of the thickness of the chiral STF suggesting that the decrease in transmittance is associated with a surface wave being launched at the interface of the magnesium-fluoride grating and the zinc-selenide chiral STF.

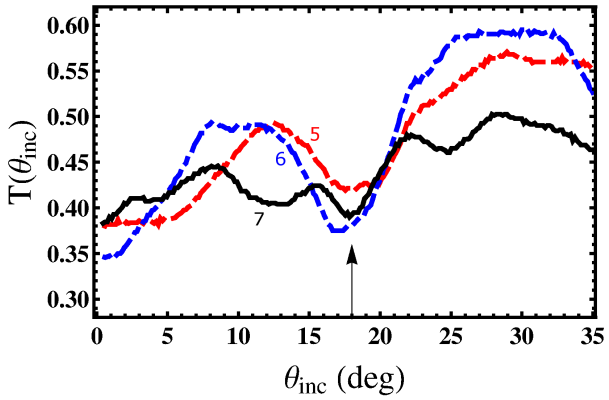

Figure 7.4: Measured values of $T(\theta_{inc})$ vs. θ_{inc} for $N_p = 5$ (red dashed curve), 6 (blue dotted-and-dashed) curve, and 7 (black curve). The vertical arrow indicates the excitation of a Dyakonov–Tamm wave at $\theta_{inc} \sim 18$ deg. Incident light was p-polarized.

Distinct dips in measured transmittance were found in each case at $\theta_{inc} \sim 18$ deg. This result can be compared with the results in Ch. 6 for the observation of the Dyakonon–Tamm wave in the prism-coupled configuration, as they both utilize the same magnesium-fluoride/zinc-selenide combination. As such the relative wave number $\kappa/\kappa_{\circ}$ can be calculated for each case to facilitate comparison. In the prism-coupling result in which dips in reflectance were found at 57.5 deg, the relative wavenumber can be calculated as $\kappa/\kappa_{\circ} = n_{prism} \sin\theta_{inc} = 1.50039$. In the grating-coupled configuration, nonspecular orders of the Floquet harmonics generated by the grating are necessary for the launch of a Dyakonov–Tamm wave. As such a Floquet harmonic should be found in proximity to any Dyakonov–Tamm wave. The relative wavenumber of the Floquet harmonics can be calculated as $\kappa/\kappa_{\circ} = \sin\theta_{inc} + m\lambda\ {L_g}^{-1}$ where m is taken from the set of integers. For the case of $m = -1$ and $\theta_{inc} = 18$ deg, $\kappa/\kappa_{\circ} = -1.49955$ with the negative

indicating that the evanescent wave will propagate in the negative-x direction.

7.6 Conclusion

The thickness independence of the dips in transmittance along with the agreement with prior observation of the Dyakonov–Tamm wave in the prism-coupled configuration indicates that the dips in transmittance correspond to the launch of a Dyakonov–Tamm wave at the magnesium-fluoride/ zinc-selenide interface. The grating-coupled excitation of Dyakonov–Tamm waves holds promise for the fabrication of more compact devices when compared to prism-coupled excitation. The use of a grating also allows the angle at which the Dyakonov–Tamm wave will be observed to be tailored to some extent. The greatest advantage that grating-coupled excitation of Dyakonov–Tamm waves holds over prism-coupled excitation is the potential to integrate several Dyakonov-Tamm-wave-based devices on a single substrate. Due to the relatively long propagation lengths of Dyakonon–Tamm waves when compared to SPP waves [120], Dyakonov–Tamm waves may be suitable for improved devises with similar applications.

The propagation of the Dyakonov–Tamm wave guided by a periodically corrugated interface was demonstrated in this chapter. This required the deposition of a conformal thin film with specific and complicated morphology on a non-planar substrate.

Chapter 8

Conclusions and Future Work

8.1 Conclusions

As was discussed in Chapter 1, my objectives for this dissertation were to:

(a) demonstrate that some of the limitations of thermal evaporation for depositing conformal thin films on non-planar substrates can be overcome;

(b) demonstrate that conformal thin films can be deposited on non-planar/non-traditional substrates without damaging the substrates; and

(c) evaluate the adequacy and the efficacy of conformal thin films of diverse morphologies in three distinct settings.

Three settings which demonstrated the efficacy of thermally evaporated conformal thin films were presented in this dissertation. Each setting demonstrated a morphology which was produced to allow for a specific application. A dense conformal thin film was deposited on a highly non-planar biological substrate to enable a method of mass producing replicas of a biotemplate. A conformal thin film with columnar morphology was deposited on a planar substrate with undulating features composed of a radically different material than the substrate to reproduce the topology of the substrate with high fidelity. A film with a well-engineered helical morphology was deposited on a periodically decorated substrate to enable the launch of an electromagnetic surface wave that had not been previously observed experimentally.

In the first setting, artificial visual decoys for an invasive species commonly known as the emerald ash borer (EAB) were fabricated through a bioreplication process which made use of thermally evaporated conformal thin films, electroforming, and several casting steps to produce a pair of dies that were used to pattern a polymer sheet upon which a Bragg reflector had been deposited to provide iridescent color which matched the targeted species. The decoys for the EAB exploited the mating behavior of this species to cue males to pounce on traps which can be used to monitor and control their spread in North America. Through preliminary studies it was found that (i) both the overall shape and micro-scale surface features must be present to attract male EAB, and (ii) decoys with color produced by paint will attract male EAB as well as decoys using a Bragg reflector for coloration.

In the second setting, I optimized a new technique which relies on the topology of a fingermark to make visible and identifiable. This technique utilizes a columnar thin film (CTF) deposited conformally over both the fingermark and underlying substrate. The CTF technique was optimized for several substrates and compared with traditional development techniques. CTF development was found to be superior to traditional techniques in several cases. Use of the CTF technique was investigated for several types of particularly difficult to develop fingermarks such as those which consist of both bloody and non-bloody areas, and fingermarks on fired cartridge casings. Additional experiments were conducted to compare the sensitivity of conventional techniques with the CTF technique. Finally, the CTF technique was compared to another thin-film fingermark development technique called vacuum-metal deposition. The thin-film morphologies resulting from the two techniques and the efficacy of developing fingermarks on several forensically relevant substrates were compared.

For the third setting, a new class of electromagnetic surface wave called a Dyakonov–Tamm wave was experimentally observed in two configurations. First, the prism-coupled configuration was utilized to excite a Dyakonov–Tamm wave guided by the interface of a dense (and isotropic) magnesium-fluoride thin film and a zinc-selenide chiral sculptured thin film. In this configuration, the excitation of a Dyakonov–Tamm wave was indicated by a reflection dip that occurred at the same angle of incidence, independent of the thickness of each partnering material, beyond some threshold, as well as the polarization state of the incident light. The Dyakonov–Tamm wave was then observed in the grating-coupled configuration. The same partnering materials were used with the exception that the planar interface was replaced with a periodically corrugated

interface. This required the deposition of the zinc-selenide chiral sculptured thin film on a non-planar substrate while maintaining the proper structure to allow for the propagation of the Dyakonov–Tamm wave.

These settings also highlighted the use of thermally evaporated conformal thin films to coat features of varying length scales. In conformally coating a beetle for bioreplication, the ability to capture the overall macroscopic shape of the beetle on the centimeter scale as well as reproducing the micrometer-scale surface features that pattern the entire beetle was essential. While not necessary in this setting, the modified-CEFR technique had previously been demonstrated as capable of capturing features which were $\sim$ 200-nm in diameter [48]. In developing fingermarks with CTFs, the ability to conformally coat micro-scale features which were found over substrates which were several centimeters in size was needed. The observation of the Dyakonov–Tamm waves required the coating of periodic features which were $\sim$ 175-nm in size.

The three settings were vastly different in the materials utilized both as substrates and thin films. In the first setting, a metal was deposited upon a relatively hard substrate of biological origin. In the second setting, several metals, semiconductors, insulators, and organic molecules were deposited upon both solid substrates of various materials and the oily emulsions of which sebaceous fingermarks are composed. In the third setting, more traditional substrates and evaporants were utilized.

The final way in which the settings differed was in the critical features of the thin films produced. In the first setting, it was critical that the structure of the beetle be closely reproduced. In the second setting the thin film was required to produce contrast between the substrate and the fingermark. In the third setting the nanoscale morphology of the thin-films had to be precisely maintained to produce the desired optical properties.

In Ch. 2 a process by which to mass produce artificial decoys for an invasive species of beetle was presented. This process achieved Objective (a) by showing that dense thin films of nickel can be conformally deposited on a highly non-planar/non-traditional substrate. Objective (b) was demonstrated by the high fidelity of the negative die used to produce the artificial decoys. Additionally, the same thin-film deposition process was used for the deposition of a conformal chalcogenide-glass thin film which could not be easily deposited by other methods. Finally, Objective (c) was demonstrated, as there had not yet been a method for mass producing highly non-planar bioreplicated surfaces. By achieving this, a tool with which entomologists and

foresters are working to control the spread of a destructive invasive species was brought about.

Chapter 3 presented the optimization a novel method of developing fingermarks for forensic identification; thereby demonstrating Objective (c). Objectives (a) and (b) were demonstrated by conformally coating a substrate upon which there were features of radically different chemical composition from the underlying substrate. It was also shown that by using a conformal thin film with columnar morphology, superior results could be obtained when compared to a dense conformal thin film. Through comparison with vacuum-metal deposition, it was shown that columnar morphology was maintained with many different evaporant materials.

The work presented in Chapters 4-7 represents the preliminary modeling of and ultimately the first experimental observation of the Dyakonov–Tamm wave. By exciting the Dyakonov–Tamm wave in the grating-coupled configuration, Objectives (b) and (c) were achieved as it required the deposition of a thin film with precisely designed and fabricated morphology on a periodically corrugated surface to allow for the support of Dyakonov–Tamm-wave propagation.

In concert, the work presented in this dissertation demonstrates that the limitations of thin-film deposition methods which utilize a directional vapor source can be overcome with appropriate substrate stage motion. Non-planar substrates with features extending over several length scales were conformally coated. Additionally, advantages associated with such film deposition techniques can be retained and extended leading to novel applications of existing thin film deposition techniques.

8.2 Suggestions for Future Work

8.2.1 Increase Scale of EAB Decoy Production

In Ch. 2 of this dissertation, artificial EAB decoys were produced from a single die that required each decoy to be hand pressed. The development of a larger die consisting of an array of many EAB would drastically increase the ability to produce decoys in significant enough numbers for proper entomological evaluation to be carried out. The development of dies which are compatible with existing manufacturing techniques (such as injection molding [121] and vacuum forming [122]) would allow bioreplicated EAB decoys to be manufactured truly on an industrial scale. This would allow for the use of such decoys in efforts to control and even eliminate the emerald ash borer from North America.

8.2.2 CTF Development of Fingermarks

The work presented in Ch. 3 represents the optimization of a fingermark development method that utilizes conformal thin films with columnar morphology deposited over fingermarks to make them visible for forensic identification. To date, this process has used the fingermarks of a single donor for the majority of the optimization and comparison with other techniques. Future work on this development technique should include evaluation of a large number of fingermarks from a wide variety of donors. This would more accurately access the value of the technique to forensic scientists.

8.2.3 Sensing Applications of Dyakonov–Tamm Waves

Having been experimentally demonstrated in Chapters 6 and 7, the use of Dyakonov–Tamm waves for sensing applications should now be targeted. As zinc-selenide chiral STFs are not easily infiltrated, the use of a different material system could ease the task of demonstrating a Dyakonov–Tamm-wave-based optical sensor. Such research would also be of value in verifying the results presented here.

Appendix A

An Objective Fingerprint Quality-Grading System

Forensic Science International 231 (2013) 204–207

Contents lists available at SciVerse ScienceDirect

Forensic Science International

journal homepage: www.elsevier.com/locate/forsciint

An objective fingerprint quality-grading system

Drew P. Pulsifer [a], Sarah A. Muhlberger [b], Stephanie F. Williams [b], Robert C. Shaler [c], Akhlesh Lakhtakia [a,*]

[a] Materials Research Institute and Department of Engineering Science and Mechanics, Pennsylvania State University, University Park, PA 16802, United States
[b] Forensic Science Program, Pennsylvania State University, University Park, PA 16802, United States
[c] Forensic Science Program and Department of Biochemistry and Molecular Biology, Pennsylvania State University, University Park, PA 16802, United States

ARTICLE INFO

Article history:
Received 11 November 2012
Received in revised form 22 April 2013
Accepted 7 May 2013
Available online 14 June 2013

Keywords:
Fingerprint grading scheme
Objective grading scheme
Clarity map

ABSTRACT

The grading of fingerprint quality by fingerprint examiners as currently practised is a subjective process. Therefore, an objective system was devised to remove the subjectivity. The devised grading system is quantitative and uses three separate, easily available, software packages to ultimately identify the portions of a fingerprint that correspond to low-, medium-, and high-quality definitive minutiae as defined on the Universal Latent Workstation of the US Federal Bureau of Investigation.

1. Introduction

The quality of a fingerprint is related to the degrees of distortion and degradation of the fingerprint [1]. Additionally, determination of the quality of a latent fingerprint is complicated by the subjectivity of currently used quality-grading systems.

The overwhelming majority of these systems—including those suggested by SWGFAST when determining suitability of a fingerprint for further analysis [2], Bond [3], and various other fingerprint researchers [4–9]—rely on the judgment of a fingerprint examiner to competently identify minutiae [10]. Depending on the quality of a fingerprint, different latent fingerprint examiners can differ on the number of minutiae identified [11–15]. Thus, the process of fingerprint identification runs the risk of varying from examiner to examiner during the progression from analysis and comparison to evaluation and finally to verification. Other grading systems are based on in-house derived algorithms to assess quality [16,17]. Some researchers assess quality based on an instrumentally derived contrast index [10,16,17].

In order to objectively grade the overall quality, clarity, and contrast of developed fingerprints, we have devised an objective, computer-based system. This grading system requires the successive use of three separate software packages to collectively transform a photograph of a fingerprint into a multicolor-coded clarity map, change the colors into a red–green–blue (RGB) spectrum, count the number of those pixels whose color corresponds to regions of definitive identifiable minutiae, and calculate the percentage of the fingerprint area which has definitive identifiable minutiae.

The quantitative quality-grading system is particularly useful when evaluating the efficacy of novel development methods, as well as for comparing two development methods using the split-fingerprint approach. The grading system is also useful for fingerprint examiners who grade latent fingerprints associated with casework. Instead of the examiner determining the number of points of comparison—which varies among examiners—this system could be used to define criteria for the percentage of a fingerprint that is of high quality before proceeding with the analysis. A similar approach underlies an alternative quality-grading system based on commercial software packages that has been devised recently [15].

2. Quantitative quality grading system: description and methodology

In order to use the quantitative quality-grading system, photographs must be taken both before and after a latent fingerprint is developed. The photographic plane of the camera must be parallel to the plane of the fingerprint, and a scale must be viewable in the resulting photograph. Thereby, variation between the length scales of the photographs can be reduced as much as possible in order to decrease errors in subsequent processing with the three computer programs.

* Corresponding author. Tel.: +1 814 863 4319.
E-mail address: akhlesh@psu.edu (A. Lakhtakia).

0379-0738/$ – see front matter © 2013 Elsevier Ireland Ltd. All rights reserved.
http://dx.doi.org/10.1016/j.forsciint.2013.05.003

The first software package employed is the Universal Latent Workstation (ULW) [18] developed by the US Federal Bureau of Investigation (FBI) to help fingerprint examiners to characterize fingerprints and then upload them to the Automated Fingerprint Identification System. The software package is supplied free by the FBI to appropriate individuals and agencies.

Once a photograph has been imported into the ULW as an image, the user is prompted to provide information about pixels per inch (ppi) of the image. The software accepts only images having a resolution of either 500 or 1000 ppi. The scale visible within the photograph's frame helps the software to identify the number of pixels in the photograph that fit within a distance of 1 inch. The software then converts the image to the proper resolution and into grayscale. Although we used version 5.9 of ULW with 1000 ppi resolution, the methodology of the quantitative grading system is applicable to other versions of ULW as well as for other resolutions.

Within ULW, there is a subset of features called the "Extended Feature Set" wherein an "Image Clarity" map can be applied to the image of the latent fingerprint. The clarity map [19] contains the colors black, red, yellow, and green that correspond to background, debatable ridge flow, debatable minutiae, and definitive minutiae, respectively. In this raw clarity map, the grayscale photograph of the fingerprint is still visible in the background. Next, the grayscale levels, brightness, and contrast are adjusted to leave only the four clarity-map colors visible. This is done by dragging the color adjustment bar at the top of the ULW program fully to the right. We refer to the clarity map altered in this way as darkened.

The darkened clarity map is to be exported as a .bmp file that is uploaded into an image-editing software package for transforming clarity-map colors assigned by the ULW into RGB (red, green, blue) color values. We used version 2.6.6 of the freeware called GIMP [20] as the second software package. RGB color values in GIMP are represented in digital 8-bit notation: black is represented by (0, 0, 0), blue by (0, 0, 255), yellow by (255, 255, 0), and white by (255, 255, 255). These values correspond to (0, 0, 0), (0, 0, 1), (1, 1, 0), and (1, 1, 1) when using arithmetic notation. The image is then saved for a pixel-counting algorithm to be used on it. In this color scheme, black corresponds to background, blue to debatable ridge flow, yellow to debatable minutiae, and white to definitive minutiae. We decided to rate the image quality based on the percentage of the image area that is white, i.e., identified as having definitive minutiae.

For this purpose, we wrote a program to run on Mathematica®, a commercially available software package [21]. In this program, the image is represented as an $N \times M$ matrix where N is the width of the image in pixels and M is the height of the image in pixels. Each element of this matrix contains the RGB value of the pixel in the image with the same coordinates. This representation is analogous to a vector field in which each coordinate in a 2-dimensional plane has a 3-dimensional vector associated with it. By our selection of the RGB values, we can simplify this vector field to a scalar field by averaging each of the RGB values. In this way, black (0, 0, 0) becomes 0, blue (0, 0, 1) becomes 1/3, yellow (1, 1, 0) becomes 2/3, and white (1, 1, 1) becomes 1. We now have an $N \times M$ matrix where each element is 1 of 4 possible numbers. Since we are only concerned with the occurrence of each value, we simplify the matrix into a list of its elements. Our task is thereby reduced to tallying the number of times that each value appears in the list and the calculating the percentage of the image each color represents after subtracting the black background pixels. We utilize the percentage of the image identified as containing definitive minutiae before and after development as a measure of the performance of the development technique as well as for comparing different fingerprint development techniques when using the split fingerprint method.

The program commands in version 7 of Mathematica® are outlined as follows:

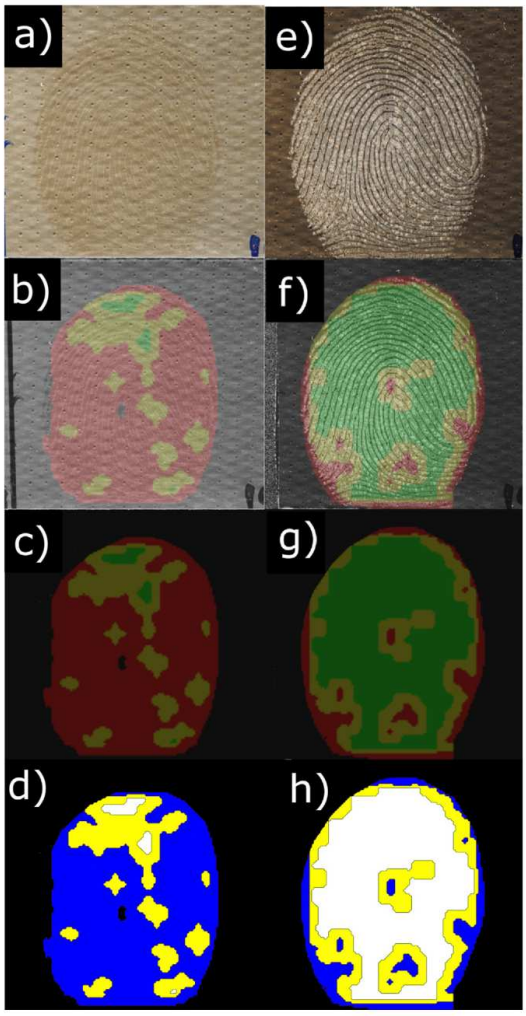

Fig. 1. (a) Latent fingerprint on Gorilla Tape® before development. (b) Same as (a) but with the raw clarity map from ULW. (c) Same as (b) but with the clarity map darkened prior to exporting. (d) Panel (c) after altering the colors in GIMP for input into Mathematica®. (e) Latent fingerprint on Gorilla Tape® after development with cyanoacrylate fuming. (f) Same as (e) but with the raw clarity map from ULW. (g) Same as (f) but with the clarity map darkened prior to exporting. (h) Panel (g) after altering the colors with GIMP for input into Mathematica®. Panels (d) and (h) correspond to 2.3% and 58% area of definitive minutiae, respectively; areas of definitive minutiae are indicated as white.

```
(1) a = Import["C:\\Insert Image from GIMP Pathname Here"];
(2) b = ColorQuantize[a,5];
(3) n = ImageDimensions[b];
(4) c = ImageData[b];
(5) e = Table[Mean[c[[A]][[B]],{A,1,n[[2]]},{B,1,n[[1]]}];
(6) f = Flatten[e];
(7) g = MatrixForm[Sort[Tally[f],#1[[1]]<#2[[1]]&]];
(8) p = Tally[f];
(9) lambda = Dimensions[p];
(10) m = lambda[[1]];
(11) sum = Total[Table[g[[1]][[k]][[2]],{k,1,m}]];
```

```
(12) Fraction[MatrixForm[Table[{3*g[[1]][[k]][[1]],N[100*g[[1]]
     [[k]][[2]]/((sum-g[[1]][[1]][[2]])"%",2]},{k,2,m}]]
```

The command (1) imports the desired image into Mathematica® subsequent to its processing with GIMP. Once the image has been imported, use of command (2) downgrades the photograph to a given number of colors. This number should be selected to be as low as possible without eliminating one of the colors assigned in GIMP. This must be done as when the image is exported from the ULW it may contain stray pixels that are not one of the four assigned colors. Ideally this value would be 4, but in practice it is selected between 5 and 7. The stray pixels account for a fraction of a percentage of the total image.

Next, command (3) is used in order to call up the dimensions of the image modified with command (2), so that pixel counters can be iterated in future commands. Command (4) generates a matrix with the same dimensions as the photograph modified by command (2) in which each matrix component is the RGB value of a pixel corresponding to that matrix element. Next, command (5) takes the average of the RGB values generated by command (4) thereby compressing the RGB value into a single number. The colors assigned in GIMP were selected so that this average value would come to 0 for black, 1/3 for blue, 2/3 for yellow and 1 for white. The simplified matrix from command (5) is then further reduced to a list by command (6). Command (7) then tallies the number of times that each value appears in this list, sorts the tally results in ascending order according to the value of the average RGB value from command (5), and reports the results in the form of a matrix with the average RGB value in the left column and the number of times of its occurrence in the right column. Command (8) utilizes the tally command again to give the total number of elements in the list generated by command (6). This is done again in order to use this information in future iterations. Command (9) gives the dimension of the matrix that has the color and its number count, for use in future iterations. Command (10) is then used to give the number of columns that appear after the execution of command (8), so that its result can be used by commands (11) and (12) as the upper limit of an iterator. Command (11) then gives the total number of all the pixels counted by summing the results of command (7). Finally, command (12) reports the percentage of the image that is composed of each color of interest. Colors are identified by their average RGB values multiplied by 3 to give each one as a whole number: 1 for blue, 2 for yellow, and 3 for white. The percentage reported is calculated from the blue, yellow and white areas of the image; black pixels are excluded. This allows us to consider only that portion of the photograph which displays ridge detail, when comparing the photographs of a fingerprint before and after development.

3. Results and discussion

The quantitative quality-grading system was used to determine the quality of development of a latent fingerprint on Gorilla Tape® with cyanoacrylate fuming. The image of the latent fingerprint before development is shown in Fig. 1a followed by the raw clarity map generated by the ULW in Fig. 1b, the darkened clarity map exported from the ULW in Fig. 1c, and the GIMP-processed image in Fig. 1d. The percentage of definitive minutiae in Fig. 1d was calculated by the Mathematica® algorithm as 2.3%. The same fingerprint was then subjected to cyanoacrylate fuming, with the

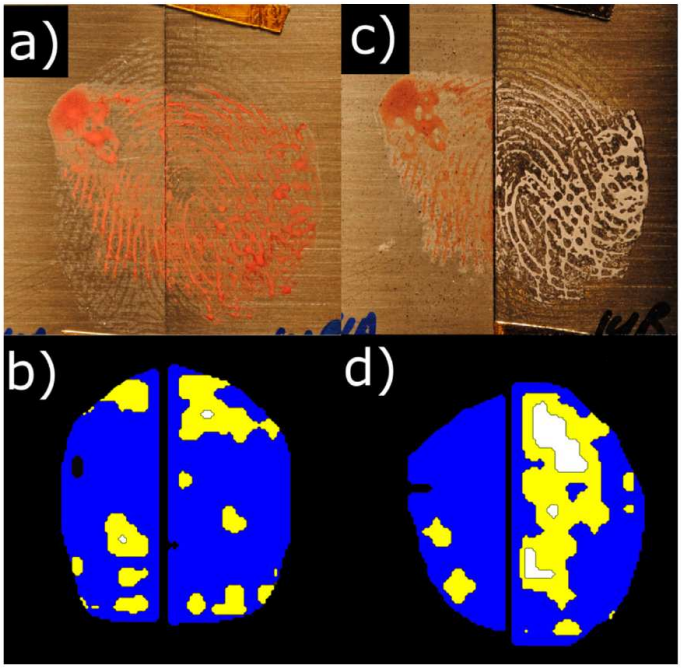

Fig. 2. (a) Partial bloody split fingerprint on stainless steel prior to development. (b) GIMP-processed images corresponding to the left and right portions of (a); the left portion was rated at 0.2% area of definitive minutiae by the Mathematica® algorithm while the right portion was rated at 0.3%. (c) Fingerprint from panel (a) after the left side was developed with cyanoacrylate fuming while the right side was developed with a nickel columnar thin film. (d) GIMP-processed images corresponding to the left and right portions of (c). The left portion was rated at 0% area of definitive minutiae by the Mathematica® algorithm while the right portion was rated at 8.7%, where the areas containing definitive minutiae are indicated in white.

photograph of the developed fingerprint shown in Fig. 1e. The ULW clarity map is shown in Fig. 1f, and the darkened clarity map to be exported is shown in Fig. 1g. The percentage of definitive minutiae in Fig. 1h is 58%, indicating substantial improvement afforded to this specific sample by cyanoacrylate fuming.

A qualitative grading scheme has been used by the UK Home Office for about 35 years [22]. In this subjective grading scheme that relies solely on visual inspection, the grade of 0 indicates no evidence of the fingerprint, 1 indicates evidence of contact but without ridge detail, 2 indicates that about one-third of the ridge detail is present but the fingerprint should not be used to identify a person from that fingerprint, 3 indicates as much as two-thirds of the ridge detail which can be used for identification, and 4 indicates full ridge details. With this qualitative scheme, the latent fingerprint in Fig. 1a was given a grade of 3, whereas the cyanoacrylate-fumed fingerprint in Fig. 1e was given a grade of 4. The subjective grading system of Ref. [22] is much too coarse in comparison to the objective grading system presented here that rated the latent fingerprint at 2.3% and the cyanoacrylate-fumed fingerprint at 58%. This illustrates that the objective grading system clearly differentiates fingerprint quality better, having a 55.7% differential between Figs. 1a and 1e versus the subjective evaluation where there was only a 1-point differential determined visually.

The quantitative quality-grading system was also used to compare development techniques and determine the superior technique using the split-fingerprint method. Fig. 2 presents a latent fingerprint split over two pieces of stainless steel. Before being developed, the left and right portions of the fingerprint were graded at 0.2% and 0.3% area of definitive minutiae, respectively. Fig. 2a shows a photograph of an undeveloped partially bloody split fingerprint on stainless steel, while Fig. 2b shows an image after processing by the three computer programs. The left portion of the fingerprint shown in Fig. 2a was then developed by cyanoacrylate fuming, and the right portion developed by the physical vapor deposition of a 100-nm thick columnar thin film of nickel [23]. The results of these developments are shown in Fig. 2c, and the corresponding final GIMP-processed images are shown in Fig. 2d. The left portion of Fig. 2d has 0% area of definitive minutiae while the right portion has 8.7% area of definitive minutiae after development with the columnar thin film.

The qualitative grading scheme of Ref. [22] leads to a grade of 3 for both the left and the right portions of Fig. 2a. The grade reduces to 2 after cyanoacrylate fuming (Fig. 2c, left) but remains at 3 after development with the columnar thin film (Fig. 2c, right). Clearly then, this subjective grading scheme is useful for initial comparison but does not take into account small details; certainly two fingerprints can have the same qualitative grade but different amounts or types of details. In contrast, the objective grading system presented here makes finer distinctions.

Let us mention here that Langenburg has independently developed a clarity map using the ULW (beta version 5.6.0) and then processed it using Adobe Photoshop (version 8.0CS) instead of GIMP, expressing the result as a percent of high-quality pixels in the image [15]. The fundamentals of this approach are similar to ours.

4. Concluding remarks

In order to objectively gauge the quality of a latent fingerprint, a quality-grading system is necessary. In that regard, an objective system was developed utilizing three easily available software packages that together remove the fingerprint examiner's subjectivity from the process of grading the quality of a latent fingerprint. This system is implemented easily because it is extremely simple and fast so that fingerprint examiners can go through the steps of the analysis quickly. Examples presented using the system demonstrated the successful quantification of definitive minutiae present. The system was also demonstrated to determine when one development technique is superior to another, using the split-fingerprint method typically employed to compare two methods.

This system is, as previously mentioned, a quantitative quality-grading system that should be useful for researchers in developing novel methods for fingerprint development and for fingerprint examiners when analyzing casework for comparing developed latent fingerprints with exemplar inked fingerprints or those taken digitally. The system provides a more robust and objective approach to the classification of quality (clarity) than currently used systems.

Acknowledgements

We thank an anonymous reviewer whose comments helped us improve the manuscript. This work was supported by Award No. 2010-DN-BX-K232, awarded by the National Institute of Justice, Office of Justice Programs, U.S. Department of Justice. The opinions, findings, and conclusions or recommendations expressed in this publication are those of the authors and do not necessarily reflect those of the Department of Justice.

References

[1] B. Budowle, J. Buscaglia, R.S. Perlman, Review of the scientific basis for friction ridge comparisons as a means of identification: committee findings and recommendations, Forensic Sci. Commun. 8 (1) (2006) http://www.fbi.gov/about-us/lab/forensic-science-communications/fsc/jan2006/research/2006_01_research02.htm (accessed 18.04.2013).
[2] http://www.swgfast.org/documents/conclusions/110315-Conclusions-DRAFT_1.1-Archived.pdf (accessed 01.05.2012).
[3] J.W. Bond, Visualisation of latent fingerprint corrosion of metallic surfaces, J. Forensic Sci. 53 (2008) 812–822.
[4] C.A. Pounds, R. Grigg, T. Mongkolaussavaratana, The use of 1,8-diazafluoren-9-one (DFO) for the fluorescent detection of latent fingerprints on paper. A preliminary evaluation, J. Forensic Sci. 35 (1990) 169–175.
[5] M. Stoilovic, Improved method for DFO development of latent fingerprints, Forensic Sci. Int. 60 (1993) 141–153.
[6] E. Halahmi, O. Levi, L. Kronik, R.L. Boxman, Development of latent fingerprints using a corona discharge, J. Forensic Sci. 42 (1997) 833–841.
[7] Y. Migron, D. Mandler, Development of latent fingerprints on unfired cartridges by palladium deposition: a surface study, J. Forensic Sci. 42 (1997) 986–992.
[8] C. Bersellini, L. Garofano, M. Gianetto, F. Lusardi, G. Mori, Development of latent fingerprints on metallic surfaces using electropolymerisation processes, J. Forensic Sci. 46 (2001) 871–877.
[9] C. Wallace-Kunkel, C. Lennard, M. Stoilovic, C. Roux, Optimisation and evaluation of 1,2-indanedione for use as a fingermark reagent and its application to real samples, Forensic Sci. Int. 168 (2007) 14–26.
[10] J.D. Humphreys, G. Porter, M. Bell, The quantification of fingerprint quality using a relative contrast index, Forensic Sci. Int. 178 (2008) 46–53.
[11] G. Langenburg, Pilot study: a statistical analysis of the ACE-V methodology – analysis stage, J. Forensic Ident. 54 (2004) 64–79.
[12] R.A. Hicklin, J. Buscaglia, M.A. Roberts, S.B. Meagher, W. Fellner, M.J. Burge, M. Monaco, D. Vera, L.R. Pantzer, C.C. Yeung, T.N. Unnikumaran, Latent fingerprint quality: a survey of examiners, J. Forensic Ident. 61 (2011) 385–418.
[13] I.W. Evett, R.L. Williams, A review of the sixteen points fingerprint standard in England and Wales, J. Forensic Ident. 46 (1996) 49–73.
[14] I.E. Dror, C. Champod, G. Langenburg, D. Charlton, H. Hunt, R. Rosenthal, Cognitive issues in fingerprint analysis: inter- and intra-expert consistency and the effect of a 'target' comparison, Forensic Sci. Int. 208 (2011) 10–17.
[15] G. Langenburg, A critical analysis and study of the ACE-V process, University of Lausanne, 2012 (PhD thesis).
[16] E. Tabassi, C.L. Wilson, A novel approach to fingerprint image quality, in: Proc. 2005 IEEE Conference on Image Processing (ICIP2005), September 11–14, (2005), pp. II-37–40.
[17] H. Fronthaler, K. Kollreider, J. Bigun, Automatic image quality assessment with application in biometrics, in: Proc. 2006 IEEE Computer Vision and Pattern Recognition Workshop (CVPRW'06), June 17–22, (2006), pp. 30–37.
[18] https://www.fbibiospecs.org/Latent/LatentPrintServices.aspx (accessed 30.10. 2012).
[19] R.A. Hicklin, J. Buscaglia, M.A. Roberts, Assessing the clarity of friction ridge impressions, Forensic Sci. Int. 226 (2013) 106–117.
[20] http://www.gimp.org (accessed 14.05.2012).
[21] http://www.wolfram.com (accessed 14.05.2012).
[22] V.G. Sears, S.M. Bleay, H.L. Bandey, V.J. Bowman, A methodology for finger mark research, Sci. Justice 2 (2012) 145–160.
[23] A. Lakhtakia, R.C. Shaler, R.J. Martín-Palma, M.A. Motyka, D.P. Pulsifer, Solid-state acquisition of fingermark topology using dense columnar thin films, J. Forensic Sci. 56 (2011) 612–616.

Appendix B

Non-technical Abstract

A conformal thin film is one which is of uniform thickness, composition, and morphology at all locations when deposited on an undulating or uneven substrate. Conformal thin films have a wide variety of uses in the microelectronics, optics, and coatings industries. The ever-increasing performance of conformal coatings has enabled tremendous technological advancement in the last half century. In this time, new film-deposition techniques which are intrinsically conformal have been developed and refined nearly to perfection. While these techniques have remarkable performance in traditional applications which utilize planar substrates such as silicon wafers, they are not suitable for some applications such as the conformal coating of non-traditional substrates such as biological material, or for applications where complicated film morphologies are required.

The process of thermally evaporating a material under vacuum conditions is one of the oldest thin film deposition techniques which is able to safely deposit a wide variety films on sensitive substrates as well as produce some remarkable and functional film morphologies. A drawback of thermally evaporated thin films is that they are not intrinsically conformal. To overcome this nonconformality while maintaining the advantages of thermal evaporation, a procedure for varying the substrates orientation with respect to the incident vapor flux during deposition was developed. This process was shown to greatly improve the conformality of thermally evaporated thin films. This development allows for several novel applications of thermally evaporated conformal thin films on non-planar/non-traditional substrates.

Three applications of improved thermally evaporated conformal thin films are discussed in this dissertation. For the first application, a process for fabricating artificial decoys to help

monitor and slow the spread of an destructive invasive species is developed. This process utilizes thermally evaporated conformal thin films with dense morphology deposited directly on the upper surface of the pest as a key step in producing a robust die. This die is then used to stamp colorful polymer sheets to produce a multiple decoys which have been shown to successfully attract the target species.

A second application of improved thermally evaporated conformal thin films is the development of fingermarks. An invisible fingermark is left on any object which is touched with the friction ridges found on the human hand. These fingermarks have long been used to identify the perpetrators of crimes due to the fact that they can be used to uniquely identify individuals. There are a wide variety of existing techniques for making these fingermarks visible, but there are certain substrates on which fingermarks are difficult to develop by existing methods. By depositing a thermally evaporated conformal thin film with columnar morphology over a substrate patterned with a fingermark, fingermarks on several difficult substrates have been successfully developed. This new technique has also been compared to traditional development techniques on less difficult substrates and found to perform better in several instances.

The final application described in this dissertation is the experimental observation of a new electromagnetic surface wave. An electromagnetic surface wave (ESW) occurs at the interface of two different materials given that the partnering materials have certain properties. There are several classes of ESWs which are characterized by the properties of the pairing of materials. The best known ESW is a surface-plasmon-polariton wave which can propagate along the interface of a metal and a non-metal. A class of ESWs called Dyakonov-Tamm waves were theoretically predicted to exist in 2007. This research represents the first experimental observation of a Dyakonov-Tamm wave. A Dyakonov-Tamm wave propagates along the interface of two non-metals with specific properties. Thermal evaporation was needed to create the helicoidal morphology of one of the partnering materials that gave it the optical properties needed to support the propagation of the Dyakonov–Tamm wave when partnered with a film with dense morphology.

Bibliography

[1] Smith, D. L., *Thin Film Deposition*, McGraw-Hill, New York, NY (1995).

[2] Vossen, J. L. and Kern, W., *Thin Film Processes II*, Academic Press, San Diego, CA (1991).

[3] Hecht, E., *Optics 4th ed.*, Pearson, New York, NY (2002).

[4] Macleod, H. A., *Thin-Film Optical Filters 3rd ed.*, Institute of Physics, Philadelphia, PA (2001).

[5] Tien, P. K., "Light waves in thin films and integrated optics," *Applied Optics* **10**, 2395–2413 (1971).

[6] Kittel, C., *Introduction to Solid State Physics 8th ed.*, Wiley, New York, NY (2005).

[7] Nicolet, M. A., "Diffusion barriers in thin films," *Thin Solid Films* **52**, 415–443 (1978).

[8] Nix, W. D., "Mechanical properties of thin films," *Metallurgical Transactions A* **20**, 2217–2245 (1989).

[9] Kumar, N., Yanguas-Gil, A., Daly, S. R., Girolami, G. S., and Abelson, J. R., "Growth inhibition to enhance conformal coverage in thin film chemical vapor deposition," *Journal of the American Chemical Society* **130**, 17660–17661 (2008).

[10] Granneman, E. H. A., "Thin films in the integrated circuit industry: requirements and deposition methods," *Thin Solid Films* **228**, 1–11 (1993).

[11] *International Technology Roadmap for Semiconductors: Executive Summary*, www.ITRS.net (2011).

[12] Saha, D. and Mukherjee, A., "Pervasive computing: A paradigm for the 21st century," *Computer* **36**, 25–31 (2003).

[13] Ganti, R. K., Srinivasan, S., and Gacic, A., "Multisensor fusion in smartphones for lifestyle monitoring," *Proceedings of the International Conference on Body Sensor Networks* , 36–43 (2010).

[14] Pulsifer, D. P. and Lakhtakia, A., "Background and survey of bioreplication techniques," *Bioinspiration and Biomimetics* **6**, 031001 (2011).

[15] Yamada, N., Ijiro, J., Okamota, E., Hayashi, K., and Masuda, H., "Characterization of antireflection moth-eye film on crystalline silicon photovoltaic module," *Optics Express* **19**, 185–125 (2011).

[16] Xiao, R. and Ming, N., "Surface roughening and surface diffusion in kinetic thin-film deposition," *Physical Review E* **49**, 4720–4723 (1994).

[17] Higashi, G. S. and Fleming, C. G., "Sequential surface chemical reaction limited growth of high quality Al_2O_3 dielectrics," *Applied Physics Letters* **55**, 1963–1965 (1989).

[18] Hampden-Smith, M. J. and Kodas, T. T., "Chemical vapor deposition of metals: Part 1. an overview of cvd processes," *Chemical Vapor Deposition* **1**, 8–23 (1995).

[19] Chae, Y. K., Egashira, Y., Shimogaki, Y., Sugawara, K., and Komiyama, H., "Chemical vapor deposition reactor design using small-scale diagnostic experiments combined with computational fluid dynamics simulations," *Journal of the Electrochemical Society* **146**, 1780–1788 (1999).

[20] Robertson, R., Hills, D., and Gallagher, A., "Silane pyrolysis," *Chemical Physics Letters* **103**, 397–404 (1984).

[21] Buss, R. J., Ho, P., Breiland, W. G., and Coltrin, M. E., "Reactive sticking coefficients for silane and disilane on polycrystalline silicon," *Journal of Applied Physics* **63**, 2808–2819 (1988).

[22] Cook, G., Timms, P. L., and Göltner-Spickermann, C., "Exact replication of biological structures by chemical vapor deposition of silica," *Angewandte Chemie International Edition* **42**, 557–559 (2003).

[23] Ritala, M. and Niinistö, J., "Atomic layer deposition," in *Chemical Vapour Deposition: Precursors, Processes, and Applications*, Jones, A. C. and Hitchmann, M. L., eds., Royal Society of Chemistry, Cambridge, United Kingdom (2009).

[24] Puurunen, R. L., "Surface chemistry of atomic layer deposition: A case study for trimetylyaluminum/water process," *Journal of Applied Physics* **97**, 121301 (2005).

[25] Huang, J., Wang, X., and Wang, Z. L., "Controlled replication of butterfly wings for achieving tunable photonic properties," *Nano Letters* **6**, 2325–2331 (2006).

[26] Musgrave, C. and Gordon, R. G., "Precursors for atomic layer deposition of high-k dielectrics," *FutureFab International* **18**, 126–128 (2005).

[27] Winters, H. F. and Kay, E., "Gas incorporation into sputtered films," *Journal of Applied Physics* **38**, 3928–3934 (1967).

[28] Chrisey, D. B. and Hubler, G. K., *Pulsed Laser Deposition of Thin Films*, Wiley, New York, NY (1994).

[29] Dirks, A. G. and Leamy, H. J., "Columnar microstructure in vapor-deposited thin films," *Thin Solid Films* **47**, 219–233 (1977).

[30] Lowndes, D. H., Geohegan, D. B., Puretzky, A. A., Norton, D. P., and Rouleau, C. M., "Synthesis of novel thin-film materials by pulsed laser deposition," *Science* **273**, 898–903 (1996).

[31] Lakhtakia, A. and Messier, R., *Sculptured Thin Films: Nanoengineered Morphology and Optics*, SPIE Press, Bellingham, WA, USA (2005).

[32] Graper, E., *Thin Film Evaporation Source Reference*. R. D. Mathis Co. (April, 2004).

[33] Pulsifer, D. P., Lakhtakia, A., and Martín-Palma, R. J., "Improved conformal coatings by oblique-angle deposition for bioreplication," *Applied Physics Letters* **95**, 193701 (2009).

[34] Martín-Palma, R. J., Pantano, C. G., and Lakhtakia, A., "Biomimetization of butterfly wings by the conformal-evaporated-film-by-rotation technique for photonics," *Applied Physics Letters* **93**, 083901 (2008).

[35] Martín-Palma, R. J., Pantano, C. G., and Lakhtakia, A., "Replication of fly eyes by the conformal-evaporated-film-by-rotation technique," *Nanotechnology* **19**, 355704 (2008).

[36] Martín-Palma, R. J., Pantano, C. G., and Lakhtakia, A., "Towards the use of the conformal-evaporated-film-by-rotation technique in fabricating microelectronic circuits and microsystems," *Microelectronics Reliability* **29**, 460–462 (2009).

[37] Haack, R. A., Jendek, E., Liu, H., Marchant, K. R., Petrice, T. R., Poland, T. M., and Ye, H., "The emerald ash borer: a new exotic pest in North America," *Newsletter of the Michigan Entomological Society* **47**, 1–5 (2002).

[38] Poland, T. M. and McCullough, D. G., "Emerald ash borer: Invasion of the urban forest and the threat to North America's ash resource," *Journal of Forestry* **104**, 119–124 (2006).

[39] Kim, M., Nagarajan, R., Snook, J. H., Samuelson, L. A., and Kumar, J., "Nanostructured assembly of homopolymers for a flexible Bragg grating," *Advanced Materials* **17**, 631–633 (2005).

[40] Lelito, J. P., Fraser, I., Mastro, V. C., Tumlinson, J. H., Böröczky, K., and Baker, T. C., "Visually mediated 'paratrooper copulations' in the mating behavior of *Agrilus planipennis* (Coleoptera: Buprestidae) a highly destructive invasive pest of North American ash trees," *Journal of Insect Behavior* **20**, 537–552 (2007).

[41] Lelito, J. P., Fraser, I., Mastro, V. C., Tumlinson, J. H., and Baker, T. C., "Novel visual-cue-based sticky traps for monitoring of emerald ash borers, *Agrilus planipennis* (coleoptera: Buprestidae)," *Journal of Applied Entomology* **132**, 668–674 (2008).

[42] Olsen, Sr., R. D., "Fingerprint identification," in *Scott's Fingerprint Mechanics*, Scott, W. R., ed., Charles C. Thomas, Springfield, IL (1978).

[43] Ramotowski, R. S., "Composition of latent fingerprint residue," in *Advances in Fingerprint Technology*, Lee, H. C. and Gaensslen, R. E., eds., CRC Press, Boca Raton, FL (2001).

[44] Ramotowski, R. S., "Methods of latent fingerprint development," in *Advances in Fingerprint Technology*, Lee, H. C. and Gaensslen, R. E., eds., CRC Press, Boca Raton, FL (2001).

[45] Lennard, C., "The detection and enhancement of latent fingerprints," *Proceedings of the 13th INTERPOL Forensics Science Symposium Oct 16-19; Lyon, France* (2001).

[46] Lakhtakia, A., Shaler, R. C., Martín-Palma, R. J., Motyka, M. A., and Pulsifer, D. P., "Solid-state acquisition of fingermark topology using dense columnar thin films," *Journal of Forensic Sciences* **56**, 612–616 (2011).

[47] Lakhtakia, A. and Polo, Jr., J. A., "Dyakonov–Tamm wave at the planar interface of a chiral sculptured thin film and an isotropic dielectric material," *Journal of the European Optical Society–Rapid Publications* **2**, 07021 (2007).

[48] Pulsifer, D. P., Lakhtakia, A., Martín-Palma, R. J., and Pantano, C. G., "Mass fabrication technique for polymeric replicas of arrays of insect corneas," *Bioinspiration and Biomimetics* **5**, 036001 (2010).

[49] Crook, D. J., Francese, J. A., Zylstra, K. E., Sawyer, A. J., Bartels, D. W., Lance, D. R., and Moss, V. C., "Laboratory and field response of the emerald ash borer (Coleoptera: Buprestidae), to selected regions of the electromagnetic spectrum," *Journal of Economic Entomology* **102**, 2160–2169 (2009).

[50] Pulsifer, D. P., Lakhtakia, A., Kumar, J., Baker, T. C., and Martín-Palma, R. J., "Toward pest control via mass production of realistic decoys of insects," *Proceedings of SPIE* **8339**, 83390H (2012).

[51] Dushkina, N. and Lakhtakia, A., "Structural colors, cosmetics, and fabrics," *Proceedings of SPIE* **7401**, 740106 (2009).

[52] Extrand, C. W., "Spin coating of very thin polymer films," *Polymer Engineering and Science* **34**, 390–394 (1994).

[53] Bailey, J. and Sharp, J. S., "Thin film polymer photonics: Spin cast distributed Bragg reflectors and chirped polymer structures," *European Physical Journal E* **33**, 341–349 (2010).

[54] Shaler, R. C., Lakhtakia, A., Rogers, J. W., Pulsifer, D. P., and Martín-Palma, R. J., "Columnar-thin-film acquisition of fingerprint topology," *Journal of Nanophotonics* **5**, 051509 (2011).

[55] McGeough, J., Leu, M., Rajurkar, K., Silva, A. D., and Liu, Q., "Electroforming process and application to micro/macro manufacturing," *CIRP Annals–Manufacturing Technology* **50**, 499–515 (2001).

[56] Lenau, T. and Barfoed, M., "Colours and metallic sheen in beetle shells—a biomimetic search for material structuring principles causing light interference," *Advanced Engineering Materials* **10**, 299–314 (2008).

[57] Domingue, M. J., Csóka, G., Tóth, M., Vétek, G., Pénzes, B., Mastro, V., and Baker, T. C., "Field observations of visual attraction of three european oak buprestid beetles toward conspecific and heterospecific models," *Entomologia Experimentalis et Applicata* **140**, 112–121 (2011).

[58] Crane, N. J., Batrick, E. G., Perlman, R. S., and Huffman, S., "Infrared spectroscopic imaging for noninvasive detection of latent fingerprints," *Journal of Forensic Sciences* **52**, 48–53 (2007).

[59] Worley, C. G., Wiltshire, S. S., Miller, T. C., Harilla, G. J., and Majidi, V., "Detection of visible and latent fingerprints using micro-x-ray fluorescence elemental imaging," *Journal of Forensic Sciences* **51**, 57–63 (2006).

[60] Batey, G. W., Copeland, J., Donnelly, D. L., Hill, C. L., Laturnus, P. L., McDiamid, C. H., MIller, K. J., Misner, A. H., Tario, A., and Yamashita, A. B., "Metal deposition for latent fingerprint development," *Journal of Forensic Identification* **48**, 165–175 (1998).

[61] Watkin, J. E., Wilkinson, D. A., Misner, A. H., and Yamashita, A. B., "Cyanoacrylate fuming of latent fingerprints: Vacuum versus heat/humidity," *Journal of Forensic Identification* **44**, 546–556 (1994).

[62] Bond, J. W., "Visualization of latent fingerprints corrosion on metallic surfaces," *Journal of Forensic Sciences* **53**, 812–822 (2008).

[63] Williams, G., McMurray, H. N., and Worsley, D. A., "Latent fingerprint detection using a scanning kelvin microprobe," *Journal of Forensic Sciences* **46**, 546–556 (1994).

[64] Pounds, C. A., Grigg, R., and Mongolaussavartana, T., "The use of 1,8-diazafluoren-9-one (DFO) for the fluorescent detection of latent fingerprints on paper. A preliminary evaluation," *Journal of Forensic Sciences* **35**, 169–175 (1990).

[65] Stoilovic, M., "Improved method for DFO development of latent fingermarks," *Journal of Forensic Sciences* **60**, 141–153 (1993).

[66] Halahmi, E., Levi, O., Kronic, L., and Boxman, R. L., "Development of latent fingerprints using a corona discharge," *Journal of Forensic Sciences* **42**, 833–841 (1997).

[67] Migron, Y. and Mandler, D., "Development of latent fingerprints on unfired cartridges by palladium deposition: A surface study," *Journal of Forensic Sciences* **42**, 986–992 (1997).

[68] Bersellini, C., Garofano, L., Gianetto, M., Lusardi, F., and Mori, G., "Development of latent fingerprints on metallic surfaces using electropolymerisation processes," *Journal of Forensic Sciences* **46**, 871–877 (2001).

[69] Wallace-Kunkel, C., Lennard, C., Stoilovic, M., and Roux, C., "Optimization and evaluation of 1,2-indanedione for use as a fingermark reagent and its application to real samples," *Forensic Science International* **168**, 14–26 (2007).

[70] http://www.cleanroom.byu.edu/TFE materials.phtml (accessed April 7th 2012)

[71] Meyers, A. and Weck, M., "Design and synthesis of Alq_3-functionalized polymers," *Macromolecules* **36**, 1766–1768 (2003).

[72] Champod, C., Lennard, C., Margot, P., and Stoilovic, M., *Fingerprints and Other Ridge Skin Impressions*, CRC Press, New York, NY (2004).

[73] Yamashita, B., French, M., Bleay, S., Cantu, A., Inlow, V., Ramotowski, R., Sears, V., and Wakefield, M., "Latent print development," in *The Fingerprint Sourcebook*, McRoberts, A., ed., National Institute of Justice, Washington, DC (2011).

[74] Migron, Y., Hocherman, G., Springer, S., Almog, J., and Mandler, D., "Visualization of sebaceous fingerprints on fired cartridge cases: A laboratory study," *Journal of Forensic Sciences* **43**, 543–548 (1998).

[75] Polo, Jr., J. A., Mackay, T. G., and Lakhtakia, A., *Electromagnetic Surface Waves: A Modern Perspective*, Elsevier, Waltham, MA (2013).

[76] Polo, Jr., J. A. and Lakhtakia, A., "Surface electromagnetic waves: A review," *Laser & Photonics Review* **5**, 234–246 (2011).

[77] Homola, J. A. ed., *Surface Plasmon Resonance Based Sensors*, Springer, New York, NY (2006).

[78] Swiontek, S. E., Pulsifer, D. P., and Lakhtakia, A., "Optical sensing of analytes in aqueous solutions with a multiple surface-plasmon-polariton-wave platform," *Scientific Reports* **3**, 1409 (2013).

[79] Shinn, M. and Robertson, W. M., "Surface plasmon-like sensor based on surface electromagnetic waves in a photonic band-gap material," *Sensors and Actuators B: Chemical* **105**, 360–364 (2005).

[80] Konopsky, V. N. and Alieva, E. V., "Photonic crystal surface waves for optical biosensors," *Analytical Chemistry* **79**, 4729–4735 (2007).

[81] Yeatman, E. and Ash, E. A., "Surface plasmon microscopy," *Electronics Letters* **23**, 1091–1092 (1987).

[82] Atwater, H. A. and Polman, A., "Plasmonics for improved photovoltaic devices," *Nature Materials* **9**, 205–213 (2010).

[83] Sekhon, J. S. and Verma, S. S., "Plasmonics: The future wave of communication," *Current Science* **101**, 484–488 (2011).

[84] Ritchie, R. H., "Plasma losses by fast electrons in thin films," *Physical Review* **106**, 874–881 (1957).

[85] Turbadar, T., "Complete absorption of light by thin metal films," *Proceedings of the Physical Society* **73**, 40–44 (1959).

[86] Kretshmann, E. and Raether, H., "Radiative decay of nonradiative surface plasmons excited by light," *Zeitschrift für Naturforschung A* **23**, 2135–2136 (1968).

[87] Otto, A., "Excitation of nonradiative surface plasma waves in silver by the method of frustrated total reflection," *Zeitschrift für Physik* **216**, 398–410 (1968).

[88] Yeh, P., Yariv, A., and Hong, C. S., "Electromagnetic propagation in periodic stratified media. I. General theory," *Journal of the Optical Society of America* **67**, 423–438 (1977).

[89] Tamm, I., "Über eun mögliche Art der Elektronenbindung an Kristalloberflächen," *Zeitschrift für Physik A* **76**, 849–850 (1932).

[90] Yeh, P., Yariv, A., and Cho, A. Y., "Optical surface waves in periodic layered media," *Applied Physics Letters* **32**, 104–105 (1978).

[91] Konopsky, V. N., Karakouz, T., Alieva, E. V., Vicario, C., Sekatskii, S. K., and Dietler, G., "Photonic crystal biosensor based on optical surface waves," *Sensors* **13**, 2566–2578 (2013).

[92] D'yakonov, M. I., "New type of electromagnetic wave propagating at an interface," *Soviet Physics–JETP* **67**, 714–716 (1988).

[93] Takayama, O., Crasovan, L. C., Johansen, S. K., Mihalache, D., Artigas, D., and Torner, L., "Dyakonov surface waves: A review," *Electromagnetics* **28**, 126–174 (2008).

[94] Takayama, O., Crasovan, L., Artigas, D., and Torner, L., "Observation of Dyakonov surface waves," *Physcial Review Letters* **102**, 043903 (2009).

[95] Kavokin, A. V., Shelykh, I. A., and Malpuech, G., "Lossless interface bodes at the boundary between two periodic dielectric structures," *Physical Review B* **72**, 233102 (2005).

[96] Maab, H., Faryad, M., and Lakhtakia, A., "Surface electromagnetic waves supported by the interface of two semi-infinite rugate filters with sinusoidal refractive-index profiles," *Journal of the Optical Society of America B* **28**, 1204–1212 (2011).

[97] Robertson, W. M. and May, M. S., "Surface electromagnetic wave excitation on one-dimensional photonic band-gap arrays," *Applied Physics Letters* **74**, 1800–1802 (1999).

[98] Kretschmann, E. and Raether, H., "Radiative decay of non-radiative surface plasmons excited by light," *Zeitschrift für Naturforschung* **23**, 2135–2136 (1968).

[99] Rosenblatt, D., Sharon, A., and Friesem, A. A., "Resonant grating waveguide structures," *IEEE Journal of Quantum Electronics* **33**, 2038–2059 (1997).

[100] Gates, B. D., Xu, Q., Steward, M., Ryan, D., Wilson, C. G., and Whitesides, G. M., "New approaches to nanofabrication: Molding, printing and other techniques," *Chemical Review* **105**, 1171–1196 (2005).

[101] Faryad, M. and Lakhtakia, A., "Grating-coupled excitation of multiple surface plasmon-polariton waves," *Physical Review A* **84**, 033852 (2011).

[102] Moharam, M. G., Grann, E. B., and Pommet, D. A., "Formulation for stable and efficient implementation of the rigorous coupled-wave analysis of binary gratings," *Optics Letters* **36**, 1584–1586 (2011).

[103] Chateau, N. and Hugonin, J. P., "Algorithm for the rigorous coupled-wave analysis of grating diffraction," *Journal of the Optical Society of America A* **11**, 1321–1331 (1994).

[104] Wang, F., Horn, M. W., and Lakhtakia, A., "Rigorous electromagnetic modeling of near-field phase-shifting contact lithography," *Microelectronic Engineering* **71**, 34–53 (2004).

[105] Marcuse, D., *Theory of Dielectric Optical Waveguides*, Academic Press, San Diego, CA (1991).

[106] Yakubovich, V. A. and Starzhinskii, V. M., *Linear Differential Equations with Periodic Coefficients*, Wiley, New York, NY (1975).

[107] Agarwal, K., Polo, Jr., J. A., and Lakhtakia, A., "Theory of Dyakonov–Tamm waves at the planar interface of a sculptured nematic thin film and an isotropic dielectric material," *Journal of Optics A: Pure and Applied Optics* **11**, 074003 (2009).

[108] Rashed, R., "A pioneer in anaclastics, Ibn Sahl on burning mirrors and lenses," *Isis* **81**, 464–491 (1990).

[109] Motyka, M. A. and Lakhtakia, A., "Multiple trains of same-color surface plasmon-polaritons guided by the planar interface of a metal and a sculptured nematic thin film. Part II: Arbitrary incidence," *Journal of Nanophotonics* **3**, 033502 (2009).

[110] Faryad, M. and Lakhtakia, A., "Prism-coupled excitation of Dyakonov–Tamm waves," *Optical Communications* **294**, 192–197 (2012).

[111] Juluria, Y., *Computer Methods for Engineering*, Taylor & Francis, Philadelphia, PA (1996).

[112] Hodgkinson, I. J., Wu, Q. H., and Hazel, J., "Empirical equations for the principal refractive indices and column angle of obliquely-deposited films of tantalum oxide, titanium oxide and zirconium oxide," *Applied Optics* **37**, 2653–2659 (1998).

[113] Kapany, N. S. and Burke, J. J., *Optical Waveguides*, Academic Press, New York, NY (1972).

[114] Gao, J., Lakhtakia, A., and Lei, M., "Synoptic view of Dyakonov–Tamm waves localized to the planar interface of two chiral sculptured thin films," *Journal of Nanophotonics* **5**, 051502 (2011).

[115] Polo, Jr., J. A. and Lakhtakia, A., "Dyakonov–Tamm waves guided by the planar interface of an isotropic dielectric material and an electro-optic ambichiral Reusch pile," *Journal of the Optical Society of America B* **28**, 567–576 (2011).

[116] Pulsifer, D. P., Faryad, M., and Lakhtakia, A., "Parametric investigation or prism-coupled excitation of Dyakonov–Tamm waves," *Journal of the Optical Society of America B* **30**, 2081–2089 (2009).

[117] Johnson, P. B. and Christy, R. W., "Optical constants of the noble metals," *Physical Review B* **6**, 4370–4379 (1972).

[118] Lakhtakia, A., Jen, Y.-J., and Lin, C.-F., "Multiple trains of same-color surface plasmon-polaritons guided by the planar interface of a metal and a sculptured nematic thin film. Part III: Experimental evidence," *Journal of Nanophotonics* **3**, 033506 (2009).

[119] Faryad, M. and Lakhtakia, A., "Prism-coupled excitation of Dyakonov-Tamm waves," *Optical Communications* **294**, 192–197 (2013).

[120] Pulsifer, D. P., Faryad, M., and Lakhtakia, A., "Observation of the Dyakonov–Tamm wave," *Physical Review Letters* , accepted for publication.

[121] Rosato, D. V., Rosato, D. V., and Rosato, M. G., *Injection Molding Handbook 3rd ed.*, Kluwer Academic Publishers, Norwell, MA (2000).

[122] Kleespies III, H. S. and Crawford, R. H., "Vacuum forming of compound curved surfaces with a variable geometry mold," *Journal of Manufacturing Systems* **17**, 325–337 (1998).

Vita

Drew Patrick Pulsifer

Drew Patrick Pulsifer was born on September 11, 1985 in Pennsylvania, USA. He received his Bachelor of Science in Physics from Millersville University of Pennsylvania in 2008, receiving the John Van Horn Award for Applied Physics.

Drew joined the Department of Engineering Science and Mechanics at the Pennsylvania State University as a Masters of Science student in the fall of 2008 under the advisement of Akhlesh Lakhtakia, the Charles Godfrey Binder Professor of Engineering Science and Mechanics. After receiving his M.S. degree in 2010, Drew continued under the advisement of Dr. Lakhtakia toward his Ph.D. degree. During the course of his graduate studies, Drew coauthored more than 20 journal articles and presented 4 papers at national conferences. Additionally, Drew received the following awards:

(i) Grand Prize at the ESM Today Paper and Poster Competition (2010),

(ii) A Society of Photo-Optical Instrumentation Engineers (SPIE) Student Travel Grant (2010),

(iii) The Haythornthwaite Fund for Innovation Prize (2011),

(iv) An SPIE Scholarship (2011), and

(v) The Penn State Alumni Association Dissertation Award (2013).